UiT
THE ARCTIC
UNIVERSITY
OF NORWAY

Faculty of Science and Technology
Department of Physics and Technology

# A Sensitivity Study of L-Band Synthetic Aperture Radar Measurements to the Internal Variations and Evolving Nature of Oil Slicks

—

**Vebjørn Karisari**

*EOM-3901 Master's thesis in Energy, Climate and Environment, 30 SP*

*June 2018*

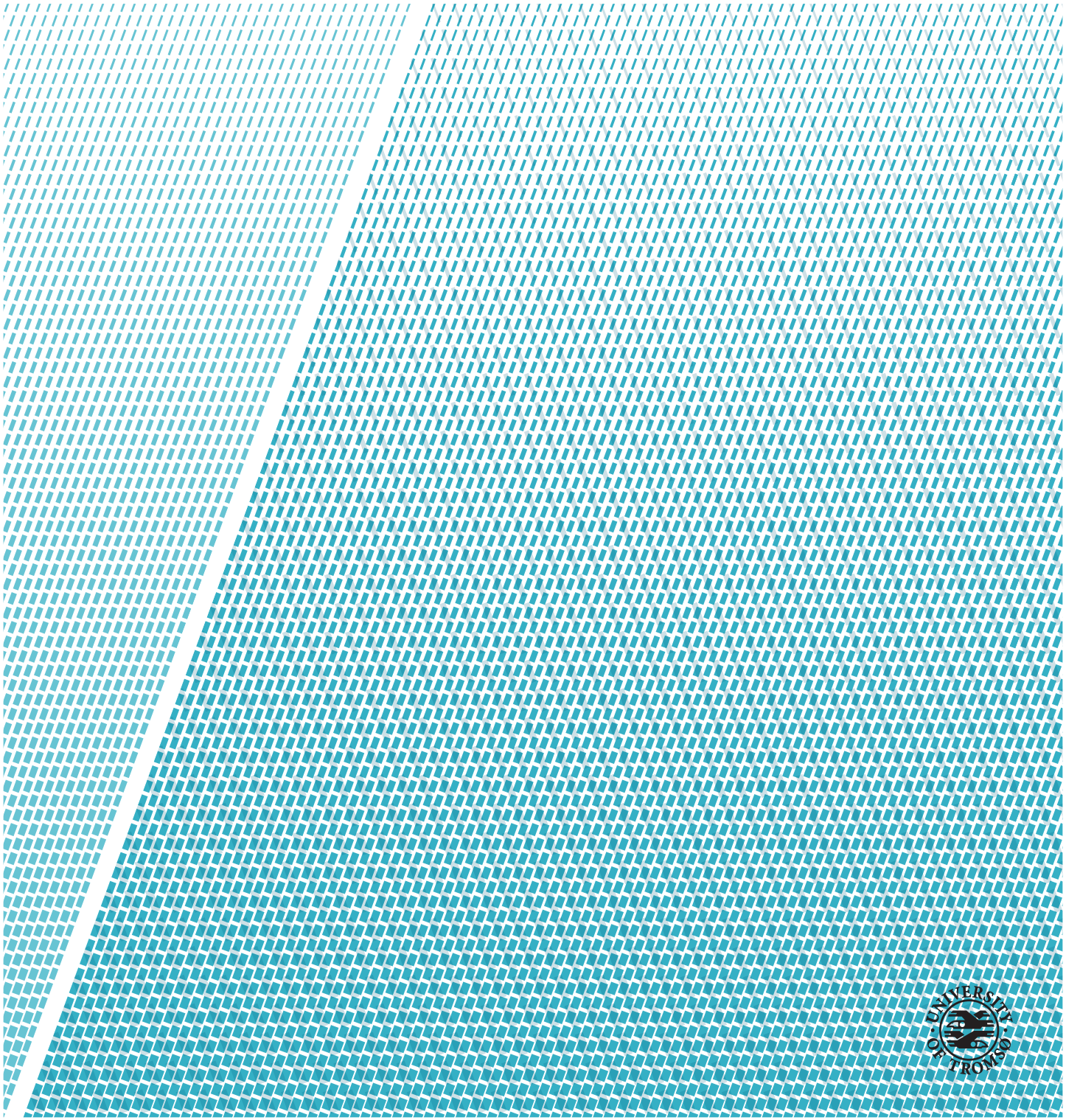

# Abstract

This thesis focuses on the use of multi-polarization synthetic aperture radar (SAR) for characterization of marine oil spills. In particular, the potential of detecting internal zones within oil slicks in SAR scenes are investigated by a direct within-slick segmentation scheme, along with a sensitivity study of SAR measurements to the evolving nature of oil slicks. A simple, k-means clustering algorithm, along with a Gaussian Mixture Model are separately applied, giving rise to a comparative study of the internal class structures obtained by both strategies. As no optical imagery is available for verification, the within-slick segmentations are evaluated with respect to the behavior of a set of selected polarimetric features, the prevailing wind conditions and weathering processes. In addition, a fake zone detection scheme is established to help determine if the class structures obtained potentially reflect actual internal variations within the slicks. Further, the evolving nature of oil slicks is studied based on the temporal development of a set of selected geometric region descriptors.

Two data sets are available for the investigation presented in this thesis, both captured by a full-polarization L-band airborne SAR system with high spatial- and temporal resolution. The results obtained with respect to the zone detection scheme developed supports the hypothesis of the existence of detectable zones within oil spills in SAR scenes. Additionally, the method established for studying the evolving nature of oil slicks is found convenient for accessing the general behavior of the slicks, and simplifies interpretation. It was observed that there seemingly exist a correlation between increasing oil fraction for mineral oil emulsions and increasing slick extent. Further, both the circularity ratio and slick complexity provided a good separation between mineral oil emulsions and plant oil, as the plant oil rapidly tended towards a circular shape whereas the emulsions became elongated.

# Acknowledgements

First and foremost, I would like to thank my co-superviser, Martine M. Espeseth, for her endless commitment and support throughout this period. Thanks for always being available for discussion, for giving me ideas and inspiration, and for proof-reading a million drafts. I really appreciate it. I would also like to thank my head supervisor, Camilla Brekke, for her engagement and contribution during this thesis. Your expertise have been of great value, and helped me move in the right direction.

Further, I would also like to thank NOFO and the Norwegian Meteorological Institute for collecting meteorological and oceanographic data of the scientific experiments investigated in this thesis.

To my family, parents, sister and girlfriend, thanks for your support and love throughout this period of time. I know you most likely do not understand my field of study, but you still show interest and support me no matter what.

Finally, I would like to thank my fellow students, EKM class '13 for making my time at the university awesome. I will miss our daily sessions of table tennis, your bad jokes, our discussions, and our collaboration. Good luck to all of you in this upcoming chapter of your life.

# Contents

# List of Figures

# List of Tables

# List of Abbreviations

**AIC** Akaike Information Criterion

**ALOS** Advanced Land Observation Satellite

**BIC** Bayesian Information Criterion

**DP** Dual-Polarization

**FP** Full-Polarization

**GHAS** Generalized Hard Algorithmic Scheme

**GMM** Gaussian Mixture Model

**H** Horizontal

**MLC** Multi-Look Complex

**NESZ** Noise-Equivalent Sigma Zero

**NOFO** Norwegian Clean Seas Association for Operating Companies

**NORSE2015** Norwegian Radar Oil Spill Experiment 2015

**OOW** Oil-On-Water campaign

**RAR** Real Aperture Radar

**RISAT** Radar Imaging Satellite

**SAR** Synthetic Aperture Radar

**SLC** Single-Look Complex

**SNR** Signal-to-Noise Ratio

**SP** Single-Polarization

**UAVSAR** Uninhabited Aerial Vehicle Synthetic Aperture Radar

**V** Vertical

# Nomenclature

| | |
|---|---|
| $A$ | Area |
| $B$ | Bandwidth |
| $C$ | Slick complexity |
| $\boldsymbol{C}$ | Covariance matrix (from the Sinclair matrix) |
| $c$ | Speed of light |
| $D_A$ | Antenna length |
| $D_r$ | Antenna width |
| $DR$ | Damping ratio |
| $d$ | Distance measure |
| $E^i$ | Incident electric field |
| $E^s$ | Scattered electric field |
| $e$ | Euler's number |
| $I(x, y)$ | Binary image function |
| $J$ | Cost function |
| $JM$ | Jeffries and Matusita separability criterion |
| $K$ | Number of clusters / components |
| $KS$ | Kolmogorov-Smirnov test |
| $k$ | Wavenumber |
| $L$ | Synthetic aperture length |
| $\hat{L}$ | Maximized likelihood function |
| $l$ | Dimension of feature vector |
| $m_{pq}$ | Raw moment of order $(p + q)$ |
| $\hat{m}_{pq}$ | Geometric moment of order $(p + q)$ |
| $N$ | Number of observations/samples |
| $N_L$ | Number of looks |
| $n_i$ | Index of refraction |
| $P$ | Perimeter |
| $P_j$ | Prior probability of class $j$ |
| $PD$ | Copolarization difference |
| $PR$ | Copolarization power ratio |
| $p(\boldsymbol{x})$ | Probability density function of $\mathbf{x}$ |
| $p(\boldsymbol{x}\|j)$ | Likelihood of class $j$ with respect to $\boldsymbol{x}$ |
| $R$ | Sensor-target distance |
| $R_c$ | Circularity ratio |

| | |
|---|---|
| $\boldsymbol{S}$ | Sinclair matrix |
| $S_{ij}$ | Complex scattering coefficient |
| $s_h$ | Standard deviation of the surface height |
| $s_L$ | Target vector in lexicographic basis |
| $u_{i,j}$ | Hard membership coefficients |
| $X_{a_{\text{RAR}}}$ | Azimuth resolution for RAR |
| $X_{a_{\text{SAR}}}$ | Azimuth resolution for SAR |
| $X_r$ | Ground range resolution |
| $\beta$ | Beam width |
| $\tau$ | Pulse length |
| $\epsilon$ | Permittivity/dielectric constant |
| $\boldsymbol{\zeta}$ | Estimated unknown parameter |
| $\hat{\boldsymbol{\zeta}}_{ML}$ | Estimated maximum likelihood |
| $\boldsymbol{Z}$ | Current estimate of unknown parameter |
| $\eta_{pq}$ | Normalized central moment of order $(p+q)$ |
| $\theta$ | Incidence angle |
| $\theta_l$ | Look angle |
| $\theta_r$ | Opening angle in range |
| $\theta_{rf}$ | Refraction angle |
| $\lambda$ | Wavelength |
| $\rho$ | Person's correlation criterion |
| $\mu_{pq}$ | Central moment of order $(p+q)$ |
| $\boldsymbol{\mu}$ | Mean vector |
| $\nu$ | Number of parameters estimated by model |
| $\boldsymbol{\Sigma}$ | Covariance matrix |
| $\phi_i$ | Hu's i'th invariant moment |
| $\boldsymbol{\psi}$ | Cluster representative |
| $\boldsymbol{\omega}$ | Class members |

# 1 Introduction

This thesis focus on the application of L-band synthetic aperture radar (SAR) for analyzing the internal variations and the evolving nature of already detected marine oil spills. This introductory chapter presents the motivation behind the study presented in this thesis, previous work done on the field, the main objectives, the contributions and findings made, and the thesis outline.

## 1.1 Motivation

As the world has been tied closer together through globalization, emission of environmentally damaging substances has experienced an extensive increase. Especially transportation, in the form of shipping account for a considerable amount of the greenhouse gasses emitted into the atmosphere. In addition, accidental and illegal discharges of oil from ships and tankers occur on a regular basis all over the world, posing an immense threat to the marine environment. As this activity often occurs at remote areas, the problem is difficult to approach. However, remote sensing systems has provided an alternative. Especially SAR has the potential of aiding a stricter regulation, by its unique capability of monitoring large-scale areas during both day and night. Further, by establishing precise oil spill detection schemes, along with robust analyzing tools for extraction of detailed oil slick information, oil spill recovery operations have the potential of becoming much more efficient. So far, research in general has focused on optimizing the oil spill detection schemes as false alarm rates are

still high. This thesis attempts to go one step further, proceeding towards the detailed analysis of already detected oil spills, in search of valuable information that might streamline current oil spill recovery operations.

Improvements in technology and tools engineered for recovery operations occur continuously, but does not help much if the procedure itself is not optimal. A common issue arises already during the earliest stages of an oil spill recovery operation, where the lack of information about the oil formation and zoning makes the decision about where to initialize the clean-up hard. Intuitively, if the clean-up is initialized in the denser regions of oil, there is a significantly higher chance of recovering more oil. Therefore, information about the internal variations within oil spills can be used to direct oil spill responders to the more critical areas of oil, thereby providing a more efficient clean-up. This thesis offers an attempt in investigating the existence of potential *radar zones* within marine oil spills for such purposes. Further, a fundamental understanding of the temporal development of oil spills is important to maintain and customize effective clean-ups. Hence, this thesis also focuses on the evolving nature oil slicks.

## 1.2 Previous Work

To the authors knowledge, research focusing on detecting potential zones within oil slicks in SAR scenes is scarce. Jones et al. in [42] investigated the potential of using the damping ratio (DR) for detecting zones for three different mineral oil emulsions and a plant oil. It was found that all the emulsions initially exhibited zoning, which persisted longest for the highest oil content emulsion, while zoning was not apparent in the plant oil slick. It was concluded that since the oil slicks studied were relatively thin, the observed zoning was most likely a result of alteration of the surface wave spectrum with different slick thicknesses and not a change in the dielectric properties [42]. It is important to note that this zone detection scheme was based upon visually inspecting the behavior of the DR, whereas a more automatic method is developed to reduce the human factor in this thesis.

In [41], Jones et al. also conducted a study focusing on modeling the oil slick transport for the same data set. The main objective in this investigation was to simulate the transport of oil at the ocean surface with respect to the prevailing meteorological and oceanic conditions, and compare it to the SAR observations acquired. In addition, some SAR observations were made directly related to the appearance of the slicks. In summary, the slick extent of the oil emulsions was found to increase more compared to the biogenetic slick simulant studied. Further, the biogenetic slick was also found to rapidly tend towards a more

compact and circular shape which stabilized in a form of equilibrium shape and size in contradiction to the oil emulsions. Again, these observations was directly deducted by visually inspecting the slicks. The same data set will therefore be subject to investigation in this thesis, as the approach for analyzing the evolving nature of the slicks is slightly different. In this thesis, the evolving nature of the oil slicks is quantified based on studying the temporal development of a set of numerical region descriptors. The features selected in this thesis include the area, perimeter, circularity ratio, slick complexity, and Hu's 1st planar moment invariant. In particular, these geometric features have been tested in the context of classification. Skrunes in [68] shed light on the opportunity of using the area, perimeter and circularity ratio as measures for discrimination between marine targets, whereas Brekke in [6] included the area, perimeter and slick complexity for classification of detected dark spots in SAR scenes. This thesis does not include the regional descriptors for direct classification purposes, but attempts to find trends in SAR time series with respect to the evolving nature of oil slicks.

## 1.3 Objectives

This thesis provides a sensitivity study of L-band SAR measurements to the internal variations and the evolving nature of oil slicks. The superior objectives are to investigate the existence of potential zoning within oil slicks in SAR scenes by performing a direct within-slick segmentation, along with studying the evolving nature of oil slicks. Two unsupervised segmentation approaches are suggested in the search of the existence of potential radar zones, namely a k-means clustering algorithm and a Gaussian Mixture Model (GMM). The k-means clustering algorithm will be preset to search for a fixed number of classes based on the framework established by optical imagery introduced later on, whereas a model selection criterion will be used for the GMM to find the best fit. Since no optical imagery are available for verification of the actual appearance of the oil slicks under observation, the class structures provided by the segmentation strategies will be evaluated with respect to environmental conditions, weathering processes, and polarimetry. The evolving nature of oil slicks will be studied by analyzing a set of selected oil slick features, i.e., geometric region descriptors based on the appearance of the slick. These features will be computed across several scenes with high temporal resolution, allowing a qualitative analysis of how the slicks behave as a function of time.

## 1.4 Contributions

The main contributions from the work presented in this thesis include:

- A simple and extendable method for detecting potential radar zones within oil spills in SAR scenes.
- A strategy of analyzing the evolving nature of oil slicks based upon numerical geometric region descriptors.
- A study demonstrating the sensitivity of multi-polarization SAR features to looser/tighter segmentation of oil slicks.

## 1.5 Thesis Outline

This thesis is organized in 7 chapters including the introduction.

**Chapter 2** reviews the basic principles of remote sensing by SAR, including e.g., the radar imaging geometry, speckle, polarimetry, and scattering mechanisms.

**Chapter 3** introduces SAR for oil spill monitoring, including e.g., the most important properties of oil, external sources acting on oil in ocean, and the oil spill detection scheme by SAR.

**Chapter 4** presents the data sets available for the investigation conducted in this thesis.

**Chapter 5** outlines the methodology developed for the investigation presented in this thesis, including e.g., the multi-polarization SAR features studied, the within-slick segmentation strategies applied, and the selected oil slick features inspected as a function of time.

**Chapter 6** presents and discusses the results obtained when carrying out the investigation presented in this thesis, including e.g., the within-slick segmentations, and the temporal development of the oil slick features selected.

**Chapter 7** summarizes the work presented, lists observations, and attempts to draw conclusions from the investigation conducted in this thesis. Additionally, uncertainties with respect to the investigation are discussed, and some ideas regarding future work on this topic are suggested.

# 2

# Remote Sensing by SAR

Remote sensing has become a crucial tool for monitoring and performing measurements of vast areas, and specific targets that are unpractical or impossible to cover by manual fieldwork. The term is used to describe the science of extracting information about some target of interest, without ever being in direct contact. The type of remote sensing data acquired is related to the information being sought, as well as the size and dynamics of the target being studied.

There exist several remote sensing systems with different technological architectures for various applications. SAR account for a vast amount of the deployed remote sensing systems that operate today. It is an *active radar* system providing high-quality resolution imagery along with all-day monitoring capabilities during almost any weather conditions. In contradiction to *passive* systems depending on external sources, a radar system generates the signal itself, and is therefore not sensitive to variations in solar illumination. The generated electromagnetic radiation is transmitted and the complex backscattered signal is recorded coherently, forming the basis of 2D-images representing the targets in focus. The high spatial resolution is a result of advanced signal processing techniques producing a synthesized antenna array, hence the name *synthetic aperture*. The upcoming chapter presents the underlying theory of remote sensing by SAR systems, including e.g., a brief introduction to the basic principles of SAR, SAR imaging geometry and acquisition principles, polarimetry, and the scattering mechanisms that occur when radar pulses interact with targets to gain necessary prerequisites before proceeding to successive chapters.

## 2.1 Basic Principles of SAR

SAR systems are often characterized by their operational wavelength and polarimetric architecture. This is mainly because different wavelengths interact in different manners with opposing targets, and that the amount of polarimetric information retrieved limits the system. An important property describing the interaction between the transmitted electromagnetic pulse and the target in focus is the *penetration depth*. Intuitively, the penetration depth is a distance measure describing how far an electromagnetic wave can propagate into a media. More specifically, it is defined as the distance an electromagnetic wave can penetrate before the magnitude is reduced by $\frac{1}{e}$ [8]. In general, the penetration depth of an electromagnetic wave increases as a function of increasing wavelength. On the contrary, as the wavelength decreases, smaller elements within the target interacts with the signal causing a decreasing penetration depth.

SAR systems operate with wavelengths covering the microwave region of the electromagnetic spectrum, spanning from around 1 mm to about 1 m. Microwaves have the favorable property of being able to penetrate through most of the composition of the atmosphere, hence avoids being altered when propagating. This spectral region is again split into different bands. The most common operational bands are C (4-8 cm)-, X (2.5-4 cm)- and L (15-30 cm)-band [58]. The investigation presented in this thesis will be based upon data collected using L-band.

### 2.1.1 Radar Imaging Geometry

The main objective of SAR systems is to form 2D-images of the ground by transmitting coherent electromagnetic pulses, and recording the complex reflectivity, i.e., backscattered signal. Figure 2.1 illustrates the configuration of such a radar system. The flight direction of the sensor platform is defined as the *azimuth* direction. As the platform moves in azimuth, the antenna illuminates the ground in the *range* direction. The total area illuminated on the ground is referred to as the *antenna footprint* determined by the *beam width* in azimuth, and *swath width* in range. The *incidence angle* $\theta$ varies with respect to range, stretching from *near range* (closest to the antenna) to *far range* (furthest away from the antenna). A target is first observed when it enters the near edge of the antenna beam, and remains within the beam until the radar has moved a distance equal to the beam width. For targets located in the middle of the beam, this distance corresponds to the *synthetic aperture length* $L$ [21].

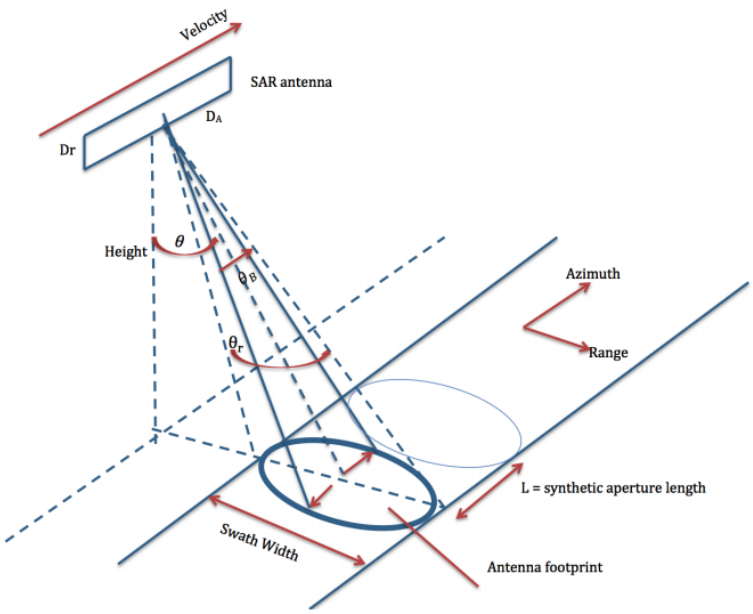


**Figure 2.1:** Illustration of SAR imaging geometry from figure 2.3 in [23]. $D_r, D_A, \theta_l, \theta_r$, and $\beta$ is the antenna width, antenna length, look angle, opening angle in range, and beam width, respectively.

The backscattered signal is segmented as the sensor platform moves, forming a two-dimensional matrix in range and azimuth. Since the time of arrival is proportional to the distance, objects at different distances from the sensor are distinguished by the arrival time. This forms the dimension in range. The second dimension is proportional to the along track distance in azimuth, taking the Doppler history into account. Each pixel within the image will then represent the scattering targets contained in the corresponding resolution cell on the ground.

### 2.1.2 Resolution

The quality of the output image is determined by the spatial resolution provided by the system. The spatial resolution is defined as the minimum distance targets within the antenna beam can be near each other while still being separable in the output image. Further, the spatial resolution is decomposed into resolution in the azimuth and range direction, describing the quality in both dimensions. For Real Aperture Radar (RAR) systems, the ground range resolution is given as [21]

$$X_r = \frac{c}{2B\sin(\theta_l)}, \tag{2.1}$$

where c is the speed of light, $\theta_l$ is the look angle, and $B$ is the bandwidth of the transmitted pulse related to the pulse length by $\tau = \frac{1}{B}$. Thus, a broader bandwidth or a short pulse produce a higher resolution. However, due to noise effects it is desired to work with high-energy pulses [23]. In order to solve this conflict of interest, the *chirp* principle is introduced. The chirp principle is a pulse compression technique that produces a short pulse spanning over a broad bandwidth, i.e., creates a high-energy pulse [21].

The resolution in the azimuth direction is given as [21]

$$X_{a_{\text{RAR}}} = \frac{R\lambda}{D_A}, \tag{2.2}$$

where $R$ is the sensor-target distance, $\lambda$ is the operational wavelength, and $D_A$ is the antenna length. The real-aperture imaging technique provides an azimuth resolution that is linearly proportional to the distance between the sensor and the target. This is the main disadvantage with such an imaging system. A spaceborne RAR system would demand an impractical antenna size to output an image with tolerable resolution. It is this adverse property that SAR confronts.

The main idea behind SAR is to synthesize an array of antennas with respect to the Doppler history. It utilizes the fact that an array of antennas is equivalent to a single antenna moving along the array line as long as the received signals are coherently recorded [21]. The Doppler effect changes during the time period in which targets are within the antenna footprint, making it possible to separate them. At first the Doppler effect is large while decreasing as the sensor moves towards the target, reaching its minimum when the target is located in the middle of the beam, and then start increasing again [15]. Considering the hardware, SAR systems are equal to RAR systems. The main difference between the two systems lies within the software, more specifically in the signal processing method used for resolution optimization in azimuth. The resolution in the azimuth direction for a SAR system is given as [21]

$$X_{a_{\text{SAR}}} = \frac{D_a}{2}. \tag{2.3}$$

Hence, the azimuth resolution for a SAR system is only determined by the dimension of the antenna, while the sensor-target distance $R$ becomes negligible.

### 2.1.3 Speckle

Although SAR systems has some very favorable properties compared to other existing remote sensing systems, it is certainly not perfect. The main disadvantage of SAR is the inherent property of *speckle* noise. Speckle is a multiplicative noise, appearing as a highly unordered and chaotic noise pattern contaminating the output images [5]. For most types of natural terrain, each scattering target within a pixel is slightly displaced relative to each other. If the displacement is random in nature, the targets will cause constructive and destructive interference, giving rise to the granular noise pattern known as speckle. Speckle is not considered as noise as in the classical sense, but is, as mentioned, an inhered property of the backscattered signal itself, and can therefore be statistically modeled as a random walk in the complex plane [69].

Speckle is a highly unwanted property as the resulting degradation pose difficulties on automatic feature extraction, and other image processing operations. Hence, a number of filtering techniques have been developed for despeckling. The arguably most common technique is multi-looking, either in the spatial- or frequency domain [8]. Since speckle in fact are pixels abruptly deviating from the surrounding pixels, an averaging box-car filter can be used in the spatial domain. The idea behind such a filter is to slide an averaging window over the entire image, whereas pixel values are assigned by taking the mean of a set of neighboring samples. This reduces the variance, thus result in less pronounce speckle. In the frequency domain, the equivalent operation is done by dividing the image into sub-looks in the azimuth direction, and then average over these. The standard deviation of the speckle is then reduced by a factor of $\sqrt{N_L}$, where $N_L$ is the number of looks extracted from the full aperture image [54]. These methods are very effective in reducing speckle, but comes at the cost of reduced spatial resolution. Another disadvantage is the induction of mixed pixels, especially at boundaries and edges which becomes less defined.

A common measure indicating the quality of the image with respect to the noise present, is the *signal-to-noise ratio* (SNR). The SNR is desired to be as large as possible, i.e., the data should preferably consist of a lot of signal compared to noise. The SNR varies as a function of incidence angle, being maximized in the middle of the antenna swath, and lowest at the edges. This is a direct consequence of the antenna pattern, as the strongest response is at this exact location. Another relevant parameter considering noise, is the *noise-equivalent sigma zero* (NESZ). It is a measure indicating if a polarimetric channel holds reliable information with respect to the amount of noise present.

## 2.2 Polarimetry

The fact that electromagnetic waves oscillates transverse relative to the direction of propagation introduces the aspect of *polarimetry*. Polarimetry is an important domain to consider when operating with remote sensing systems as it might potentially reveal information about physical properties of the target under observation [69]. The polarization of electromagnetic waves is contained within the elements of the vector amplitude of the electric field [21]. Polarized waves can be defined as where the electric field oscillates in one direction or in a specific pattern. The upcoming section gives a brief review of the diversity of polarimetric architectures, before proceeding to elaborate about full-polarization (FP) SAR systems as will be studied in this thesis.

### 2.2.1 Polarization Diversity

Utilizing the polarimetric information encoded within the electromagnetic radiation have become a crucial part of both active and passive remote sensing systems. The fundamental quantity measured by a polarimetric SAR system is the complex scattering coefficient $S_{ij}$ from the target, where $i$ and $j$ define the polarization on transmit and receive [76]. In the linear basis, an electromagnetic wave can have *horizontal* (H) or *vertical* (V) polarization. H is usually defined as the state at which the electric vector component oscillates perpendicular to the plane of incidence, while V is where the electric field is orthogonal to the propagation direction and the horizontal polarization [21]. Other forms of polarization states include e.g., circular and elliptical polarization. Circular polarization occurs when two linear horizontal and vertical polarized waves are transmitted simultaneously, with 90° out of phase for the vertical polarized wave. Intuitively, elliptical polarization occurs when these waves are not orthogonally transmitted.

Different polarization architecture acquires different polarimetric information based on the channels on transmit and receive. Most commonly, polarimetric SAR systems have operated with linear polarization basis including the HH, HV, HH and VV channels. Single-polarization (SP) SAR systems transmit and receive on the same polarization channel. Dual-polarization (DP) SAR systems also transmit one polarization, but receive on two channels. The combination of channels received depends on the polarization of the transmitted wave. Further, FP SAR systems both transmit and receive on horizontal and vertical, while retrieving all four polarization combinations, i.e., HH and VV, and HV and VH, often referred to as the co- and cross polarization channels, respectively [69]. There also exist SAR systems utilizing the property of circular/elliptical polarization. Such systems are most commonly referred to as hybrid polarization or compact polarization SAR systems, and can be further explored in [23].

### 2.2.2 Full-Polarization SAR

In recent years, SAR systems have developed from operating with a single channel to cover all possible polarization combinations. Such FP SAR systems provide the unique capability of measuring the complete scattering matrix, often referred to as the Sinclair matrix, allowing a more precise identification and extraction of the scattering properties within a given resolution cell [22]. The Sinclair matrix contains complex scattering coefficients for each pixel, characterizing the scattering mechanisms occurring at that specific point on the ground. The matrix relates the electric field incident onto the target to the electric field scattered from the target [78]

$$\begin{bmatrix} E_p^s \\ E_q^s \end{bmatrix} = \frac{e^{-jkR}}{R} \begin{bmatrix} S_{pp} & S_{qp} \\ S_{pq} & S_{qq} \end{bmatrix} \begin{bmatrix} E_p^i \\ E_q^i \end{bmatrix}, \tag{2.4}$$

where $E^i$ denotes the incident electric field and $E^s$ is the scattered electric field, $k$ is the wavenumber defined as $k = \frac{2\pi}{\lambda}$, and subscript $q$ and $p$ denotes the orthogonal linear polarization states. The total backscattered signal for an FP system can then, in the linear horizontal-vertical basis, be expressed mathematically as the Sinclair matrix [46]

$$\boldsymbol{S} = \begin{bmatrix} S_{HH} & S_{HV} \\ S_{VH} & S_{VV} \end{bmatrix}. \tag{2.5}$$

The four terms can be reduced to three if *reciprocity* is assumed, meaning that the interaction between the target and the electromagnetic wave is equal for the cross-polarization channels, namely that $S_{HV} = S_{VH}$ [46][60]. This is usually done when dealing with monostatic[1] systems where the internal state of the target is unaltered by the polarization of the probing wave [69].

From this Sinclair matrix, various polarimetric target descriptors have been developed for interpreting and relating the polarimetric information collected to target properties. The *Lexicographic scattering vector* is a common polarimetric target descriptor, and provides the basis for the much desired *covariance matrix*. The Lexicographic target vector is given as [46]

$$s_L = [S_{HH} \;\; \sqrt{2}S_{HV} \;\; S_{VV}]^T, \tag{2.6}$$

1. A monostatic system transmits and receive the signal with the same antenna.

where T denotes the transpose operation. The covariance matrix is defined as the multi-looked Hermitian outer product of this scattering target vector, given by the following equation [46]

$$\boldsymbol{C} = \langle s_L, s_L^{*T} \rangle = \frac{1}{K} \sum_{i=1}^{L} s_L s_L^{*T}, \tag{2.7}$$

where $\langle \cdot \rangle$ indicates spatial averaging (multi-looking), and $*$ denotes the complex conjugate. Thus, the *multi-looked complex* (MLC) covariance matrix is given as [46]

$$\boldsymbol{C} = \begin{bmatrix} \langle |S_{HH}|^2 \rangle & \sqrt{2}\langle S_{HH} S_{HV}^* \rangle & \langle S_{HH} S_{VV}^* \rangle \\ \sqrt{2}\langle S_{HV} S_{HH}^* \rangle & 2\langle |S_{HV}|^2 \rangle & \sqrt{2}\langle S_{HV} S_{VV}^* \rangle \\ \langle S_{VV} S_{HH}^* \rangle & \sqrt{2}\langle S_{VV} S_{HV}^* \rangle & \langle |S_{VV}|^2 \rangle \end{bmatrix}. \tag{2.8}$$

The covariance matrix is arguably the most common reference point regarding the interpretation of FP SAR data, as a wide diversity of multi-polarization SAR features can be extracted by decomposing this matrix. Another common reference point is the *coherency matrix*, operating in the Pauli space originating from the Pauli target vector. The reader is referred to [46] and [58] for further reading regarding this topic.

As mentioned, FP SAR systems extract more polarimetric information compared to SP and DP systems, but comes at the cost of typically smaller spatial coverage or reduced spatial resolution, along with requiring more power [22]. The smaller swath is a result of fulfilling the Nyquist criteria, since the pulse repetition frequency is higher for FP SAR systems. The type of polarization architecture and which channels that are active vary and depends upon the field of application. Previous studies have suggested that the HH-channel is more suited for sea ice surveillance [17], compared to the VV-channel which is more suited for ocean surface sensing [2][28][34]. Therefore, since this thesis works with oil spills in marine environments, the VV-channel will be preferred.

## 2.3 Scattering Mechanisms

If electromagnetic radiation is subject to an interface separating two media with different dielectric or magnetic properties, the electromagnetic radiation will be altered. This interaction leads to scattering mechanisms. The type of scattering mechanism occurring is strongly related to the property of the incident wave, and the physical characteristics of the target under observation. In general, we separate between three different types of scattering mechanisms, i.e., surface-, double bounce-, and volume scattering. These scattering mechanisms will be the subject of discussion in remaining part of this chapter.

### 2.3.1 Surface Scattering

Surface scattering is the scattering mechanism referred to when the incoming electromagnetic radiation only disperse once at the surface boundary between two media, hence it is often called single bounce scattering. It occurs at surfaces that are considered reasonably flat relative to the wavelength of the incoming radiation [23]. The backscattered response from surface scattering is closely related to the *roughness* of the surface, which again is related to its geometry, i.e., physical shape. The wavelength of the incoming electromagnetic radiation determines the scale at which the roughness of the target is detected. By nature, waves interact more significantly with objects having a geometry of the same order of magnitude as the wavelength. This causes short wavelengths to be more sensitive to small variations at the surface compared to longer wavelengths.

In the case of very smooth surfaces relative to the incident wavelength, the reflection occurs in the specular direction, and is described by Snell's law [21]

$$n_1 \sin\theta = n_2 \sin\theta_{rf}. \tag{2.9}$$

Here, $n_i$ denotes the index of refraction related to the dielectric constant by Maxwell's relation $n_i = \sqrt{\epsilon}_i$, and $\theta_{rf}$ is the refraction angle [13][23]. Hence, for perfectly smooth surfaces no backscatter will be detected as the radiation is reflected away from the sensor [69]. Intuitively, in order for a remote sensing system to be able to collect any information, the surface needs to be rough to some extent. Whether or not a surface is considered rough is commonly determined by the Rayleigh Criteria, given as

$$s_h \geq \frac{\lambda}{8}\cos\theta, \tag{2.10}$$

where $s_h$ is the standard deviation of the surface height. The surface is considered rough if the equality holds [23]. For rough surfaces, the scattering

consists of one *coherent* reflection component in the specular direction and one *diffuse* (incoherent) component occurring randomly in all directions. As the roughness of the surface increases, the coherent scattering component becomes negligible and the scattering tends towards a Lambertian pattern, i.e., completely diffuse and independent of the incidence angle of the incoming radiation [23][69].

### 2.3.2 Double Bouncing Scattering

Double bounce scattering refers to the scattering mechanism that occurs when electromagnetic radiation undergoes two bounces when interacting with an interface. This scattering mechanism occurs in general from dihedral corner reflectors like e.g., buildings. For ideal corner reflectors, the complete backscattered response lies completely within the copolarization channels, i.e., no contribution exist in the cross-polarization channels [13][23]. In general, man-made structures produces double bounce scattering. This makes vessels traveling at seas distinguishable from its surrounding, and easy to detect by SAR imagery and other remote sensing systems.

### 2.3.3 Volume Scattering

Volume scattering is the result of interaction between electromagnetic radiation and media with local variations in the dielectric properties [13]. Recall the ability of electromagnetic radiation to penetrate into media (discussed in Section (2.1)). Volume scattering occurs when the electromagnetic radiation penetrates into the interface, creating backscattering contributions from different layers within the media. L-band, which is the operational wavelength on the sensor providing the data for this thesis, lies in the far microwave region, and therefore have a relatively large penetration depth compared to e.g., C- and X-band. Thus, when studying oil in marine environments, there is a risk that a portion of the backscattered response originate from the underlying sea water.

# 3

# SAR for Oil Spill Monitoring

Spaceborne remote sensing SAR systems have paved the way for global coverage monitoring, with high spatial resolution on a repeated basis. This has provided the opportunity of regulating large-scale areas, along with the possibility of extracting endless information, giving rise to climate models, weather forecasting, meteorological- and oceanographic research, and pollution monitoring. These branches have become increasingly dependent on the services provided by SAR systems. Especially for oil spill monitoring, SAR has proven to be a very favorable sensor due to its characteristics. This chapter introduces the topic of marine oil spills, including an overview of the most important oil properties, the mechanisms that determine the fate and behavior of oil slicks in the marine environment, and the application of SAR for oil spill monitoring.

## 3.1 Oil Spills in the Marine Environment

The release of oil into the marine environment occurs frequently all over the world, with the evident majority originating from natural seeps from geological strata below the sea floor and anthropogenic sources related to oil production, transportation and consumption. Hence, the occurrence of oil spills correlate well with the major production cites and transport routes, along with geologically active areas. Annually, it has been estimated that about 1.2 million tons of oil are exposed to the marine environment [67]. Releases in connection with reported ship accidents only account for a small part of this, whereas a

larger portion emerges from both legal and illegal deliberated discharges from ships during routine operations [69]. The environmental impacts associated with oil spills is complex and depends on several factors like e.g., the volume and type of oil spilled, the ambient weather conditions, and the presence and sensitivity of ecological life. In general, various types of oil interacts differently with the marine environment, thereby causing different slicks to behave and develop independently over time. This temporal evolvement is often strongly correlated to the properties of the oils, along with various weathering processes and environmental conditions. This upcoming section introduces and discusses these factors.

### 3.1.1 Properties of Oil

Oil describes a wide selection of both natural and synthetic compounds, used especially as lubricants and fuel. There exist a wide selection of oil types with different composition, causing their properties to vary significantly from type to type. The most important properties to recognize when dealing with oil spills in marine environments are *viscosity*, *density*, and *solubility*, along with the *dielectric constant* [14][69].

**Viscosity** can be defined as a substance resistance to flow, where low viscosity indicates an easier flow compared to a high viscosity substance [14]. In terms of oils, the viscosity depends on the relative fraction of light and heavy components, whereas the viscosity increases as a function of increasing heavy components. Consequently, oil spills with low viscosity are more likely to spread out and form a thin layer over a larger area on the ocean surface compared to high viscosity oil. In general, the viscosity of oil increases approximately exponentially as a function of decreasing temperature [24].

**Density** is defined as a substances mass per unit volume. Oils are defined as light or heavy, depending on their density. The property is important because it indicates whether a specific oil will float or sink when exposed to water. The average sea water has a density slightly larger then most oils, hence oils will in general float on the ocean surface [14][24].

**Solubility** is a measure indicating the amount of oil that will dissolve in the water column on a molecular basis [14]. In general, the solubility of oil in water is low, but the soluble parts can potentially be toxic to the aquatic life [14]

**Dielectric constant** (relative permittivity) is defined as the ratio between a substances permittivity and the permittivity of vacuum [69]. The

dielectric constant of oil is much lower than that of sea water [56]. Therefore, if the oil is mixed sufficiently into the water column, the effective dielectric constant at the ocean surface is expected to decrease. In terms of remote sensing, the backscattered signal tends to increase as a function of increasing dielectric constant [80]. Hence, oil spills are expected to produce a lower backscatter than clean ocean.

### 3.1.2 Weathering Processes

Oil spills are subject to a number of weathering processes immediate after release. Weathering denotes a variety of physical, chemical, and biological processes that transforms the oil spill as a function of time. Consequently, weathering processes are crucial in determining the fate and behavior of oil spills. As a part of the objective in this thesis is to study the temporal evolvement of oil spills, it is essential to understand the concepts behind the most important weathering processes. Intuitively, the impact of the different weathering processes depends on environmental conditions, but the oil properties are in fact more decisive [69].

The most important weathering processes acting on oil spills include *evaporation*, *emulsification*, *dispersion*, *dissolution*, *spreading*, *oxidation*, and *biodegradation*. In general, these processes can be sorted into two chronological categories based on when they have their dominant effect, i.e., the *early stage* and the *later stage* of an oil spill [40]. Figure 3.1 illustrates these processes and how they influence oil in marine environments.

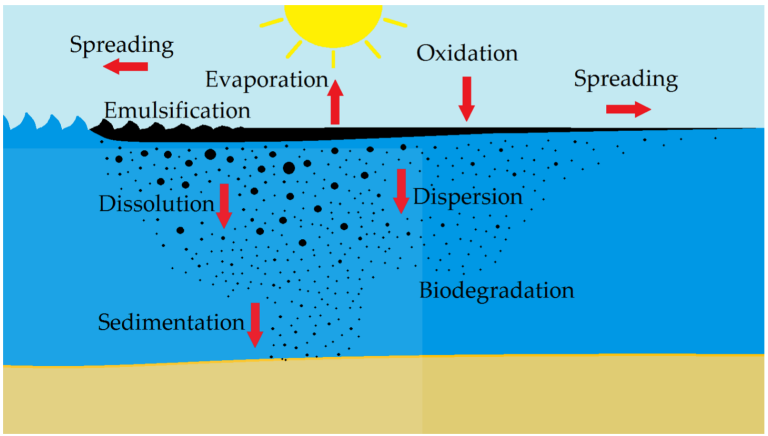


**Figure 3.1:** Overview of the most important weathering processes acting on oil at sea. Illustration from figure 2.1 in [69], adapted from [1].

The dominant weathering processes in the early stage of an oil spill are spreading, evaporation, dispersion, emulsification and dissolution, whereas oxidation, sedimentation and biodegradation are long term processes [40]. It is these long term processes that ultimately determines the fate of an oil spill. The weathering processes are listed and elaborated below.

**Spreading** is an important weathering process in the initial phase after release, and refers to the oils ability to spread out on the ocean surface. The spread is closely correlated to the viscosity of the oil and the environmental conditions such as wind and ocean current. Typically. the spread of oil is not uniform, indicating that the formation of various zones will occur [47][69]. In fact, it has been found that more than 90 % of the oil can potentially be located in less than 10 % of the slick area [37].

**Evaporation** involves the loss of preferentially light compounds of the oil into the atmosphere. This especially influence the mass balance between heavy and light compounds, causing the density and viscosity to increase [47]. Light crude oils can potentially lose up to 75 % of the initial volumes within a few days, while medium crudes might lose as much as 40 %. On the contrary, heavy or residual oils only looses 10 % of its initial volume [14]. The loss of volume due to evaporation is hard to model as most oils consist of a mixture of hundreds of compounds.

**Emulsification** involves the mixing of water into the oil spill. Typically, this will thicken and increase the volume, which again contributes to the persistence of oil spills [63]. Emulsification might also increase the oil viscosity up to three orders magnitude [14].

**Dispersion** occurs when oil spills are subject to turbulent ocean states, causing parts of the oil to break up and mixed vertically, down into the water column. This weathering process becomes dominant for low viscosity oil spills, where as much as 90 % or more of the slick might potentially be dispersed. The dispersibility decreases in line with increasing viscosity.

**Dissolution** involves the chemical stabilization of oil components in the ocean. Although it only accounts for a small portion of the oil loss, it is considered an important weathering process as the soluble components of oil can be toxic to aquatic species [14].

**Oxidation** causes the organic compounds of oil to form new compounds, along with rearranging the distribution of residual compounds. These oxidized products are more soluble in water compared to the compounds they originate from [14].

**Biodegradation** of hydrocarbons has been considered one of the principal removal mechanisms in the aquatic environment. The biodegradation rate is correlated to the environmental conditions, including oxygen concentration, nutrients, temperature, salinity and pressure, as well as oil properties [14].

**Sedimentation** is the sorption of oil to suspended sediments that eventually settle out of the water column and accumulate on the seafloor [14].

Later on, in the investigation presented in this thesis, the within-slick segmentations will be evaluated with respect to the weathering processes outlined above, along with an attempt in correlating these to the evolving nature of the oil slicks studied.

### 3.1.3 Environmental Impacts

Environmental and oceanic processes also influences the temporal development of oil slicks. Especially the transport and movement are controlled by drift from varying components of winds and currents, the turbulent movement of oil in the upper ocean, along with weathering [59]. In general, the horizontal movement of oil slicks is controlled by the ambient current, wave-induced Stoke drift, and wind drag at the ocean surface [41].

Typically, oil slicks on the ocean surface are transported along with the ocean current with a drift speed of a few percent (~3.5%) of the wind speed for low to moderate wind speeds (3-7 m/s), and a drift angle of ~15° right/left of the wind direction when at the north/south hemisphere [14][41]. For higher winds, an increasing occurrence of wave breaking and vertical mixing slows the drift to about 0.5% of the wind speed, and a slightly larger deflection angle [20].

The particles within oil slicks are affected by surface Stoke drift, which involves the cyclic motion of particles moving up and down into the water-column, depending on their location within the water column, with respect to the ocean state. Also, as oil slicks in general remain on the ocean surface, they are subject to forcing by wind. This introduces the exposure to Langmuir Circulation. Langmuir Circulation, often expressed as windrows, are a common oceanic phenomenon generated by the ambient wind conditions in combination with Stoke drift [14]. This phenomenon induce the accumulation of divergence and convergence bands on the ocean surface, creating windrows parallel to the wind direction. With respect to oil slicks, windrows can potentially have many effects. It can enhance the movement of the slick, affect the oil thickness by creating convergence and divergence zones on the surface, and enhance

the vertical dispersion of oil droplets [14]. Typically, windrows are observed along the upwind end of oil slicks, where the layer of oil is relatively thin, while oil in general accumulates in the downwind direction, where viscous effects dominate the dynamics [48]. Thus, oil slicks are often experience to have a relatively well-defined leading edge in the downwind direction, along with a streaky trailing edge or feathered appearance in the upwind edge of the slick [2][66].

## 3.2 Oil Spill Detection Scheme by SAR

A variety of remote sensing systems have been used for detecting and classifying marine oil spills. Traditionally, SAR systems have been used for monitoring and detection, while optical systems have been used for classification and verification. Optical systems have the advantage of capturing data equivalent to the human eye, making it easy to detect oil spills and observing potential zones. The downside of using optical systems is the strict limitation to variation in solar illumination and vulnerability to environmental conditions. Therefore, it is desired to explore if SAR systems are able to reveal the same information as optical systems for detecting potential zones in oil spills. The upcoming section presents the principles behind using SAR for oil spill monitoring, and outlines the framework regarding oil spill zoning established by optical systems, here also being sought for SAR systems.

### 3.2.1 Scattering at the Ocean Surface

Oceans and open water are in general considered rough surfaces, hence exhibit surface scattering (see Section (2.3.1)) of incoming electromagnetic radiation. The scattering occurring at clean ocean surfaces for typical SAR incidence angles[1] can be described through Bragg theory [38][81].

The presence of waves mainly characterizes the dynamics at the ocean surface. These waves span over a wide spectrum, with wavelengths of several hundred meters to capillary waves of a few millimeters. For typical SAR incidence angles, when small-scale waves dominate at the ocean surface, the backscattered response is characterized by Bragg scattering. Bragg scattering occurs when the wavelength of the incidence electromagnetic radiation is in resonance with the wavelength of the ocean facet [23][46]. In addition to Bragg scattering, large-scale gravity waves on the ocean surface cause an in-plane tilt and out-of-plane tilt of the facet, which adds a response in the cross polarized channels,

1. Incidence angles in the range of ~18°-50° [69]

and alters the response in the copolarized channels [22]. The *tilted Bragg model* accounts for this, and is therefore commonly used to model the backscattered response when observing marine environments.

The radar backscatter from the ocean also varies as a function of incidence angle, yielding an increasing signal for decreasing incidence angles. When approaching large incidence angles, the backscatter may also be limited by the system noise floor [69]. The incidence angle dependency is related to the operational wavelength and polarization, in addition to the current environmental conditions at the ocean surface. Figure 3.2b illustrates a scene from Data Set 2 (which will be introduced later on in Chapter 4, along with the sensor used) showing the averaged backscattered response as a function of incidence angle. As the figure shows, the backscatter decreases as a function of increasing incidence angle. The slight increase when approaching far range is a result of approaching the system noise floor. In general, the most useful incidence angles spans from 20° to 45° [34].

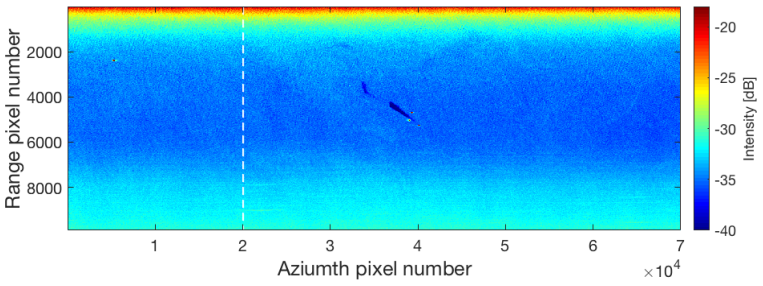


**(a)**

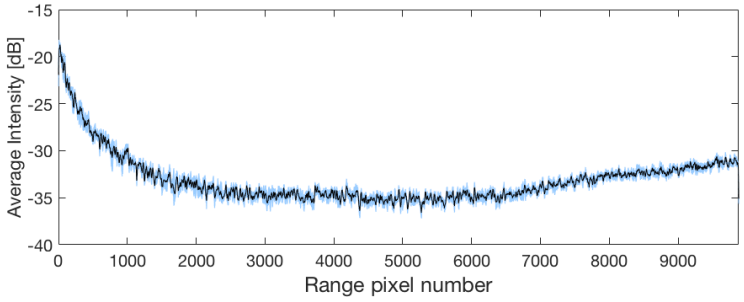


**(b)**

**Figure 3.2:** Radar backscatter as a function of incidence angle for ocean surface sensing. a) VV intensity image of marine oil spill, and b) average intensity in dB as a function of incidence angle. The light blue lines represent the profile for 100 azimuth pixels around the dashed white line in a), whereas the black line represent the average of those profiles.

### 3.2.2 Detectability of Oil Spills in SAR Images

The backscattered response from oil spills collected by SAR systems is complex and dependent on several factors. This includes oil spill properties, e.g., dielectric properties, viscosity, extent, and composition, environmental conditions, e.g., wind, sea state, and temperature, and sensor properties, e.g., frequency, resolution, coverage, and SNR. In general, two factors mainly provides the contrast that allows for detectability of oil spills in SAR images, namely the damping effect and reduction in the dielectric property (see Section (3.1.1)). Typically, oil will spread out, forming a thin layer covering the ocean surface. This will dampen the small-scale surface roughness, thereby smoothing the ocean surface. This smoothing results in reduced backscatter compared to the surrounding clean ocean [22], thus provides a contrast. In addition, the dielectric property is found to change significantly when water is polluted by oil. If the oil spill is relatively thick and/or the concentration of oil droplets within the water column is relatively high, a reduction in the dielectric property occurs resulting in less radar backscatter [56][72]. Oil spills will therefore appear as dark regions in SAR images.

In general, literature regarding remote sensing of oil spills in the marine environment primarily focuses on oil spill detection schemes (see e.g., [7][33][51][52][76]). Several automatic and semi-automatic oil spill detection schemes have been established, with varying successes. False alarms are a common issue, as so-called *look-alikes* often occur at the ocean surface. Look-alikes is the term used to describe phenomena occurring at the ocean surface that produces a backscattering response similar to oil spills. This includes natural films, low wind, heavy rain, grease ice, etc. [36]. Until now, the research has proceeded towards optimizing these automatic oil spill detection schemes. In fact, literature investigating potential radar zones detection and evolving nature of oil slicks is scarce. However, in this thesis, it is desired to move one step further, and investigate if potential zones can be detected within oil spills by using SAR instead of optical system, and if SAR measurements can be used to quantify the fate and behavior of oil spills.

### 3.2.3 Challanges and Limitations

Several challenges arise when using SAR systems for monitoring oil spills in marine environments. The arguably most encountered problem with using SAR for monitoring oil spills in marine environments is the challenge of distinguishing oil spills from look-alikes. Look-alikes are, as mentioned, other natural phenomena with similar SAR signatures as oil spills. Hence, appearing as dark patches on the sea surface. A number of classification schemes have been developed for separating actual oil spills from look-alikes based upon the shape, texture, edges, and contrast, along with the presence of natural slicks in the vicinity, and SAR derived wind speed [7]. Also, a technique involving log-cumuluants have been developed for separating biogenic slick from mineral oil with success for low resolution (50 meters) SAR images [70]. This field of study is still ongoing, as no perfect method have been found. In this thesis, the risk of encountering look-alikes is minimal as the oil slicks under observation are intentionally discharged, and thereby verified.

The environmental conditions also introduce limitations when using SAR for oil spill monitoring. Especially wind constrains the opportunity of performing reliable measurements, as it effectively influences the dynamics at the ocean surface. Thus, the backscattered level and the visibility of oil spills and look-alikes are also influenced [76]. The operational wavelength of a SAR system determines the range of wind speeds that the instrument "tolerates". As the wind increases, the contrast between oil spills and the surrounding water decreases. In high wind, only thick regions of oil are visible [7]. Look-alikes are often encountered in local low wind areas, where the lack of roughness on the ocean surface produce a low backscattered response. Intuitively, higher wind speeds causes a rougher ocean surface, thereby decreasing the possibility of detecting look-alikes [3]. There is no universal upper limit agreed upon regarding wind conditions for SAR imagery, but e.g., the Kongsberg Satellites Services based in Tromsø operates with 15 m/s as an upper limit for their oil spill detection report [3].

### 3.2.4 Bonn Agreement Oil Appearance Code

The *Bonn Agreement Oil Appearance Code* is an international standard developed to classify regions within oil spills in marine environments. Typically, five distinct classes have been used to map oil spills based upon thickness and volume. Table 3.1 outlines the different classes.

| **Classes** | **Layer Thickness Interval ($\mu m$)** | **Volume (liters of oil per $km^2$)** |
|---|---|---|
| Shine | 0.04 to 0.30 | 40 to 300 |
| Rainbow | 0.30 to 5.0 | 300 to 5000 |
| Metallic | 5.0 to 50 | 5000 to 50 000 |
| Discontinuous True Color | 50 to 200 | 50 000 to 200 000 |
| True Color | 200< | 50 to 300 |

**Table 3.1:** Overview of the class labels for internal zoning within oil slicks established in the Bonn Agreement Oil Appearance Code [49].

The names of the five categories are related to the visual appearance of oil with the properties listed. Shine and rainbow often correspond the to thin, outermost layers in oil spills, while the true color often appears in relatively dense regions. Figure 3.3 shows two optical acquisitions of oil spills where zones are labeled with respect to the Bonn Agreement Oil Appearance Code. Recall that a part of the objective of this thesis is to inspect the possibility of detecting similar radar zones in oil spills. Therefore, later on, a portion of the within-slick segmentation scheme will be based on these five distinct categories. Note that the number of zones detectable by using radar imagery might not necessarily have to be the same as with optical systems.

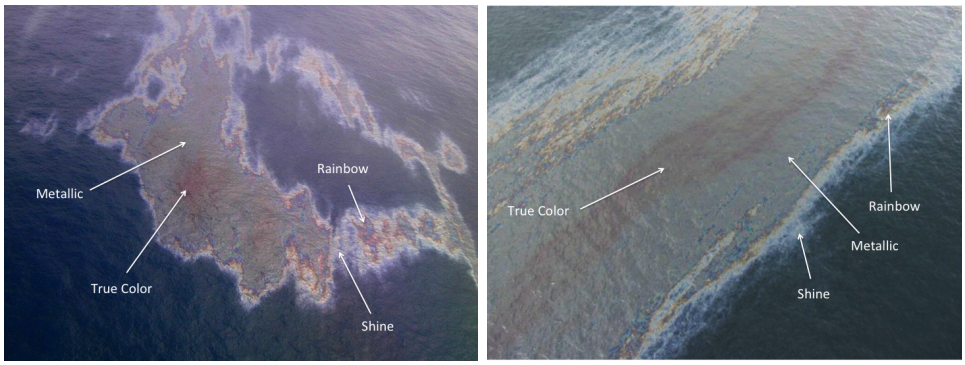


**Figure 3.3:** Optical acquisitions of marine oil spills with internal zoning labeled according to the Bonn Agreement Oil Appearance Code. Photographies are curtesy of NOFO (Bonn Agreement Aerial Surveillance data obtained during NOFO Oil-On-Water exercise).

# 4

# Dataset

In general, data for oil spill remote sensing scientific purposes is scarce. Since oil spills in fact pose an environmental threat, it is difficult to obtain permission for deliberate and controlled experiments. An exception is the annual Oil-On-Water (OOW) exercise conducted by the Norwegian Clean Seas Association for Operating Companies (NOFO). During these campaigns, several oil spills are deliberately discharged with the solid purpose of training the preparedness for oil spill recovery. Although the fundamental motivation behind these campaigns is to test procedures and technology for oil spill recovery, it simultaneously provides an unique opportunity for collecting data for remote sensing research purposes. The work presented in this thesis is based on data collected during the OOW exercise conducted in 2015. The upcoming sections introduces the campaign itself before proceeding to the dedicated scientific experiments that were embedded into the 2015 OOW campaign. The data used throughout this thesis were obtained during these scientific experiments.

## 4.1 The Oil-On-Water Campaign

NOFO is an organization for operators on the Norwegian continental shelf specialized in reducing the environmental damage by efficient and robust oil spill response. Its mandate is to "*ensure that oil recovery preparedness is always dimensioned in keeping with the needs and contingency plans of the operating companies*" [26]. To achieve such an optimal preparedness, they conduct several exercises involving oil spill recovery under realistic conditions every year. The OOW campaign is one of the few large-scale exercises involving several vessels, aircrafts and representatives from the oil industry, research and development companies, pollution authorities, the coast guard, the coastal administration and research institutes [69]. To pose minimum damage and disturbance to the surrounding environment, the operation takes place at the abandoned Frigg field located in the North Sea (59° 59' N, 2° 27' E) (see figure 4.1) during the part of the year when the presence of birds and marine life is minimal.

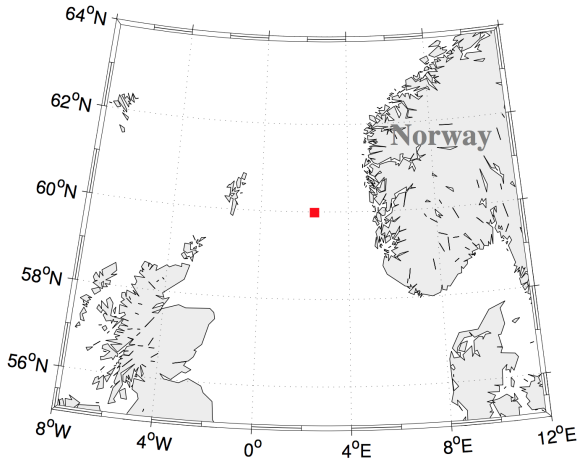


**Figure 4.1:** The annual OOW exercise is located at the abandoned Frigg field, marked with a red square (figure from figure 6.1 in [69]).

The OOW exercise in 2015 was conducted over a four-day period from 8-11 of June. In total, NOFO had permission of releasing 130 tons of oil during the campaign [44]. Multiple spills with different oil emulsion[1] and volume were released spread over all days. Despite relatively high wind conditions, all planned spills were conducted. In total, two data sets acquired on separate dates during OOW 2015 by the same sensor are available for this thesis. The following sections present the sensor technology, introduces the experimental setups, and the data collection.

1. Dispersion of one liquid in another immiscible liquid. In this case, an oil/water mixture.

## 4.2 Sensor

During the OOW 2015, several remote sensing systems were deployed to collect measurements of the experiments conducted, including the well-known Radarsat-2, RISAT-1, TerraSAR-X, ALOS-2, as well as the National Aeronautics and Space Administration's (NASA's) FP L-band airborne Uninhabited Aerial Vehicle Synthetic Aperture Radar (UAVSAR). The data provided for this thesis was acquired by the latter sensor while mounted on a GulfStream-III aircraft. Figure 4.2 shows the sensor platform setup.


**(a)** GulfStream-III aircraft. **(b)** UAVSAR mounted on the aircraft.

**Figure 4.2:** Photographies of the UAVSAR mounted on the GulfStream-III aircraft taken by Camilla Brekke.

The UAVSAR system is unique as it provides high spatial resolution imagery with a significantly low noise floor compared to other existing remote sensing SAR systems. An exception might be the German Aerospace Center's multi-frequency (X-, C-, S-,L-, and P-band) FP F-SAR with even better spatial resolution, and more or less equivalent NESZ (for L-band) [64]. The fact that the UAVSAR sensor is airborne allows for frequent, repetitive acquisitions, thereby providing high temporal resolution if needed. Important properties of the UAVSAR sensor are listed in table 4.1. The UAVSAR is, as mentioned, an FP system resulting in the Sinclair matrix (see Section 2.2.2) being collected. The reader is referred to [27] and [45] for further reading regarding the sensor technology of the UAVSAR.

| Mode | Polarization | Wavelength [cm] | Incidence angle | NESZ [dB] | Resolution (range × azimuth) | Swath width | Look direction |
|---|---|---|---|---|---|---|---|
| PolSAR | HH, HV, VH, VV | L-band (23.8 cm) | 19.5° to 67.5° | ~ -48 to -33 | 2.5 m × 1 m | 20 km | Left |

**Table 4.1:** Overview of important properties of the UAVSAR sensor [27].

## 4.3 Data Set 1 (NORSE2015)

The first data set provided for this thesis was collected during the Norwegian Radar oil Spill Experiment 2015 (NORSE2015), conducted on June 10. NORSE2015 was a joint experiment between the UiT The Arctic University of Norway (UiT) and the Jet Propulsion Laboratory (JPL)/NASA performed in collaboration with NOFO. The motivation behind the experiment was to systematically collect multisensor- and multifrequency (X-, C-, and L-band) SAR data of surface oil slicks with different known properties. A comparative study between the sensors is presented in [74], which found the UAVSAR to provide the best visual slick-sea contrast and slick detectability, along with superior SNR. Before proceeding, note that the UAVSAR scenes illustrated throughout this thesis have been geocoded with the reference system WGS84 and epsg:4326.

### 4.3.1 Experimental Setup

The experiment was designed to collect data for studying the polarization-dependent electromagnetic signals and their relationship to varying oil-water mixtures and dielectric properties, as well as the slicks evolving nature as a function of time [22]. In total, four substances were released close in time with a spatial separation of about 0.5 nautical miles. Three of these substances was oil emulsions produced by NOFO with equal composition (Troll crude oil, Oseberg crude oil, and One-Mul emulsifier) with varying volumetric fraction of oil, namely 40% (E40), 60 % (E60), and 80% (E80). The fourth substance was plant oil (P) simulating a natural biogenetic slick. Table 4.2 presents important properties of the discharges.

| Release | Time (UTC) | Substance | Volume |
|---|---|---|---|
| P | 04:48 | Plant oil: Radiagreen ebo | 0.2 $m^3$ |
| E40 | 04:59 | Emulsion (40 % oil)<br>300 L water + 100 L Troll + 100 L Oseberg + 0.2 L One-Mul | 0.5 $m^3$ |
| E60 | 05:15 | Emulsion (60 % oil)<br>200 L water + 150 L Troll + 150 L Oseberg + 0.2 L One-Mul | 0.5 $m^3$ |
| E80 | 05:30 | Emulsion (80 % oil)<br>100 L water + 200 L Troll + 200 L Oseberg + 0.2 L One-Mul | 0.5 $m^3$ |

**Table 4.2:** Properties of the four substances released during NORSE2015 [74].

The first substance released was the plant oil, followed by the oil emulsions with increasing volumetric oil fraction. Following release, all four slicks were left untouched on the ocean surface. The experiment was designed in a way that provided consistency regarding the incidence angle by aligning the discharges approximately parallel to the flight (azimuth) direction of the various

spaceborne sensor platforms, and acquisitions were made when the slicks were located in the middle of their swaths to maximize the SNR. The flight path of the aircraft carrying the UAVSAR was then preprogrammed to collect measurements accordingly. In total, 22 scenes were acquired in a parallel ascending-descending (heading 7°/187°) manner during two flights as the aircraft needed refueling midway. The first flight collected 16 scenes and lasted from 05:32-08:53 UTC, while the second flight captured 6 scenes lasting from 11:45-13:18 UTC [74]. An exception is the last scene from the first flight, which was capture with a heading of 142°. Figure 4.3 shows the incidence angle span for each slick for the entire UAVSAR time series.

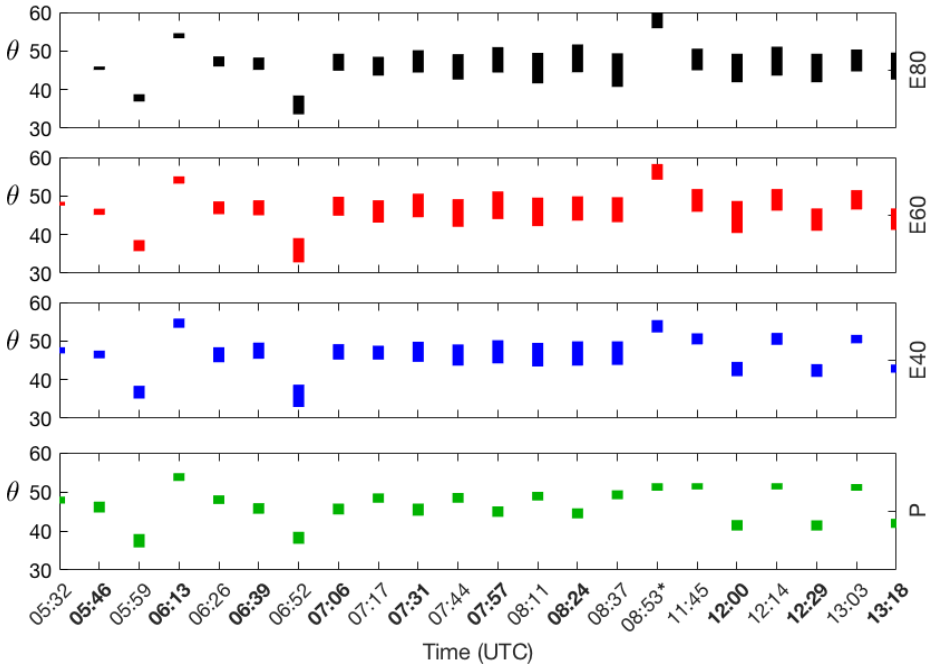


**Figure 4.3:** Overview of the incidence angle range for each slick along the UAVSAR time series. Figure adapted from figure 2 in [22].

Figure 4.4 shows the geocoded intensity images of the 22 scenes collected during NORSE2015 with the time of acquisition labeled below its respective scene. Labels with normal fonts correspond to scenes acquired while ascending, whereas bold fonts indicate scenes acquired while descending. The cross-flight acquisition captured at 08:53 UTC clearly stands out, and is indicated with a * symbol. As the figure shows, the E80 was not released in time of the first acquisition (05:32 UTC). Therefore, the slick labels are indicated in the second scene where all the discharges was completed.


**Figure 4.4:** Geocoded intensity images of the VV channel of the 22 scenes in acquired during NORSE2015. The time of acquisition is labeled below the images, where normal fonts correspond to scenes captured while ascending, bold fonts correspond to scenes captured while descending, and * denotes the cross-flight acquisition. The E80 is the northernmost slick, followed by the E60, E40, and P, respectively. The bright white objects in the scenes are nearby vessels. UAVSAR data are courtesy of NASA/JPL-Caltech.

In addition, *in situ* data, including meteorological and oceanographic information was collected from different platforms during the experiment. Multiple measurements were acquired on board of the release vessel, while additional information was captured by weather balloons, drifters and buoys released from the same vessel. The drifters and buoys were deployed simultaneously with the oils, while the weather balloons were released at different times throughout the day [74]. The weather conditions were harsh during the experiment. While discharging the oils, the vessel measured wind speeds of 9-11 m/s from a west-southwest direction, a wave height of 2.5 m, and a temperature of 9 °C. Such wind conditions are in the upper part of the range where oil spill detection is considered possible [25][75].

| **Time** (UTC) | **Sensor Platform** | **Wind Speed** [m/s] (direction) | $\mathbf{H}_S$ [m] | **Temperature air** (sea surface) |
|---|---|---|---|---|
| 04:30 | Ship | 12 | 2.5 | 10 °C |
| 04:50 | Ship | 11 | 2.5 | 19 °C |
| 05:34 | Ship | 9 (248°) | | |
| 06:18 | Ship | 12 (260°) | | |
| 06:52 | Balloon | | | 10.2°C |
| 05:00-23:50 | Drifters | | | (9.9-10.2 °C) |

**Table 4.3:** Measurements of the meteorological and oceanographic conditions during NORSE2015 [74].

The primary focus for this data set is to investigate the evolving nature of the oil slicks due to the number of acquisitions available along with the high temporal resolution. The potential of detecting radar zones have already been investigated in [42] for this data set, which found that the slicks showed tendencies of exhibiting some zoning in the early stages of the releases, but few or no zoning as time went by. Note that no direct within-slick segmentation was performed in that investigation. Hence, an attempt in detecting radar zones within these oil slicks is still carried.

## 4.4 Data Set 2

The second data set available for this thesis was acquired during the last day of the OOW 2015 campaign, i.e., on June 11. Whereas NORSE2015 was rigorously designed and planned over an extensive time period, the data collected during this experiment became a bonus flight.

### 4.4.1 Experimental Setup

The exercise included the release of two mineral oil emulsions, both of the type Oseberg Blend. The main motivation behind this experiment was to test the performance of an oil spill recovery system. Thus, it was not in any way facilitated the collection of remote sensing data, which is noticeable by the lack of preferred *in situ* measurements and number of acquisitions.

The first spill was released at 08:06 UTC and was a test release of 6 $m^3$. The release of the second main spill ended at 08:53 UTC south of the test release with a volume of 16 $m^3$. Several acquisitions were made with the UAVSAR, but only three acquisitions contained the actual discharges. Each of these three acquisitions were made with different imaging geometry. The first acquisition was made at 08:46 UTC with a heading of 187°. The second acquisition was made at 09:03 UTC with a heading of 277°, while the last scene was captured at 09:18 UTC while heading 142°. The geocoded product of the intensity images of the three acquisitions are shown in figure 4.5, where 4.5a, 4.5b, and 4.5c shows the first, second and third acquisition, respectively. The images are oriented with north pointing upward, such that the left, uppermost slick correspond to the test release while the right, lowermost slick is the main slick. In addition, the scenes are scaled equally to preserve their sizes relative to each other. Note that the test release is somewhat split in all scenes. Throughout this thesis only the larger (left) part of the test release will be studied.

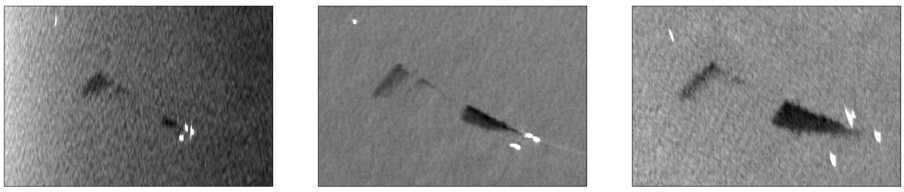

**(a)** **(b)** **(c)**

**Figure 4.5:** Geocoded intensity images of the VV channel of the a) 08:46 UTC, b) 09:03 UTC, and c) 09:18 UTC acquisition included in Data Set 2. The test release correspond to the leftmost slick, while the main slick is the rightmost slick. The bright white objects correspond to nearby vessels. The images are oriented with north pointing upward, and scaled equally to preserve their size relative to each other. UAVSAR data are courtesy of NASA/JPL-Caltech.

During the experiment, some *in situ* data was also collected. The wind speed was measured to be 7-9 m/s between 07:00-11:00 UTC, causing a relatively rough surface. In addition, the wind direction at 09:40 UTC was measured to be 237°. Figure 4.6 shows the range of incidence angles which the oil slicks span over for each acquisition. Note that the imaging geometry during the second flight causes the slicks to span over a relatively narrow range of incidence angles, compared to the other acquisitions.

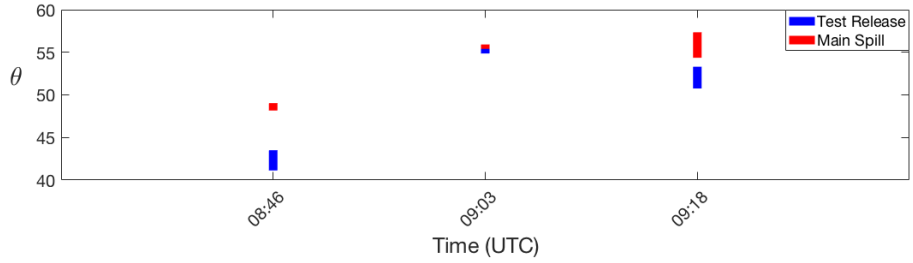


**Figure 4.6:** Overview of the incidence angle range for each slick in the scenes included in Data Set 2. The test release is indicated with blue, while the main slick is represented by red.

## 4.5 Speckle Filtering

The intensity images of each channel obtained by an FP SAR system, assuming reciprocity, can be represented as the diagonal of the covariance matrix (see equation (2.8)), and can be referred to as $\boldsymbol{C}_{11}$, $\boldsymbol{C}_{22}$, and $\boldsymbol{C}_{33}$ depending on the channel of interest. These elements are computed from the *single-look complex* (SLC) SAR data, and must therefore be filtered in order to reduce speckle.

Speckle filtering is the most fundamental step within image processing of SLC SAR data. Recall that a common way of reducing speckle is by multi-looking (see Section 4.5), often referred to as smoothing in the spatial domain or incoherent averaging in the frequency domain. For simplicity, a mean filter with the proper dimension will be used throughout this thesis. The size of the filter mask is crucial as it balances the trade-off between noise reduction and preservation of spatial resolution. Recall from table 4.1 that the UAVSAR instrument provides a slant range resolution 2.5 times greater than the azimuth resolution (2.5 m $\times$ 1.0 m). Hence, in order to obtain a square resolution cell, the filter mask should have the same aspect ratio. Previous studies have applied a $15 \times 60$ filter mask size with success, corresponding to a ratio of 1:4 between pixels in range and azimuth. As one of the main objectives of this thesis is to investigate the potential of detecting zoning within the oil slicks, a high spatial resolution is wanted, meaning that a small filter mask with the same aspect ratio should be used. The VV-channel is in general less affected by noise compared to the other polarization channels due its significant level above the noise floor [2][34][69], making it even more favorable for the application in this thesis.

# 5

# Methodology

In this chapter, central aspects of the method used to investigate the objectives outlined in Section (1.3) will be presented. The data sets available for this thesis are unique as they include acquisitions of controlled discharges of oil with different, known properties and *in situ* measurements. The airborne UAVSAR instrument used for the data collection provides scenes that have both high spatial- and temporal resolution with a significantly low noise floor. This permits a detailed analysis of the internal variations within the slicks, and their temporal development over time. The upcoming sections introduce relevant multi-polarization SAR features, the strategies used for the within-slick segmentation in search of the existence of potential radar zones, and the geometric oil slick descriptors used to quantify the behavior of the oil slicks as a function of time.

## 5.1 Multi-Polarization SAR Features

Radar polarimetry has become an important domain within SAR remote sensing for extracting information about the observed media. Consequently, by rigorous research over time, many *multi-polarization* SAR features (polarimetric features) have been defined and used to reveal valuable information for different applications. Polarimetric features are basically parameters defined by individual or combinations of polarimetric channels. Thus, the diversity of polarimetric features is only constrained by imagination. Different polarimetric features can be computed by e.g., decomposing the covariance- and coherency matrix. Since this thesis considers oil in a marine environment, the selection of polarimetric features is based on previous studies that have found certain features valuable for this application [22].

### 5.1.1 The Damping Ratio

Oil dampens the capillary waves on the ocean surface, causing regions infested by oil to return less radar backscatter. This dampening effect introduces the damping ratio (DR). The DR is a common polarimetric feature that has been extensively studied and tested for the application of monitoring oil in marine environments (see e.g., [22][42][69][83]). It is defined as the ratio between the backscattered response from clean, homogenous ocean and oil-infested ocean, thereby quantifying the contrast. Mathematically it can be expressed as [57]

$$DR_{ij} = 10\log_{10}\left(\frac{\langle|S_{ij}^{(ocean)}|^2\rangle}{\langle|S_{ij}^{(oil)}|^2\rangle}\right), \qquad ij \in \{HH, HV, VH, VV\} \tag{5.1}$$

where $S_{ij}^{(oil)}$ is the complex scattering coefficient from oil-infested ocean, $S_{ij}^{(ocean)}$ is the corresponding complex scattering coefficient from clean, homogenous ocean, and subscript $i$ and $j$ denotes the polarization on transmit and receive, respectively.

The DR is an attractive polarimetric feature as it only requires single polarization SAR data as input. However, the literature is divided regarding the importance of the polarimetric architecture chosen when using the DR. Some studies have suggested that the DR is independent of polarization architecture [31][83], while others have found that the VV-channel provides an enhanced contrast between oil-infested ocean and clean ocean [52][62]. Jones et al. in [42] found only minor differences between the DRs sensitivity to the detection of zoning within oil spills in SAR scenes as measured using the VV, HH, and

HV modes. The obvious disadvantage with the DR is that it requires the user to construct an area that simulates the backscattered response from a homogenous, clean ocean area corresponding to the oil spill area. This introduces uncertainties, as well as room for errors. Ideally, this region should completely represent the radar backscatter with respect to the current wind and sea state, along with spanning over the same incidence angles as the oil spill. In practice, such a region is impossible to construct, but an accepted approximation is to crop a homogenous, clean ocean region shifted in the azimuth direction, spanning over the same incidence angles relative to the oil spill.

The DR has been found to increase with increasing oil viscosity and thickness, and decrease as a function of increasing windspeed [12][29]. This implies that it might potentially exist a correlation between the existence of zones within oil spills and the behavior of this polarimetric feature. In addition, the contrast has been reported to increase with incidence angle, but have been found independent of the radar look-direction relative to wind for wind speeds between 6-10 m/s [83]. However, Skrunes et al. in [73] found that the DR was sensitive to the look-direction with respect to upwind/downwind, which in fact also is demonstrated in this thesis. For mineral oil slicks, the DR has been observed to increase with increasing wave number [32], causing the DR to provide a larger response for shorter wavelengths [42].

In the pilot project of this thesis, the behavior of the copolarization difference (PD) defined as [72]

$$PD = \left\langle |S_{VV}|^2 \right\rangle - \left\langle |S_{HH}|^2 \right\rangle . \tag{5.2}$$

was also studied. The results obtained showed a somewhat similar trend in the class structures obtained when using the DR and PD as input for the within-slick segmentation. With that in mind, before proceeding to investigate both the DR and PD, a correlation test between the two polarimetric features is carried out based on Pearsons correlation coefficient. The correlation test can be found in Appendix A, and provided a significant correlation ($\rho \geq 0.85$) for the majority of the slicks in Data Set 2. Based on this observation, the PD will not be included further in this thesis.

### 5.1.2 Copolarization Power Ratio

In addition to the dampening effect, the dielectric properties of the ocean surface might also potentially be altered when exposed to oil. Recall from Section (3.2.2) that if the oil spill is relatively thick and/or if the concentration of oil droplets within the water column is relatively high, a reduction in the dielectric constant occurs resulting in less backscatter. With that in mind, internal variations of the dielectric constant within oil slicks might potentially correspond to variations in oil slick thickness.

In the tilted Bragg regime, the contribution from the ocean wave spectrum is independent of the polarization. This causes ratios of polarimetric channels to be a function of only surface slope, incidence angle and the dielectric constant [57]. Consequently, such ratios are independent of the dampening effect of capillary waves induced by oil. Additionally, since the long wavelength ocean waves that govern the surface slope are largely unaffected by the presence of oil or other surface contaminates [57], local variations with respect to ratios of polarimetric channels are likely to correspond to local variations in the dielectric constant. Hence, in order to investigate the internal variations within oil slicks with respect to the dielectric properties, the copolarization power ratio (PR) is introduced, and defined as [57]

$$PR = \frac{\langle |S_{HH}|^2 \rangle}{\langle |S_{VV}|^2 \rangle}, \tag{5.3}$$

Minchew et al. in [57] investigated the theoretical PR for different concentrations of oil when using the tilted Bragg model, and found that a higher concentration resulted in a higher PR. This implies that there might be reasonable to believe that there exist a correlation between variations in PR and potential oil slick zones. In addition, a relation between increasing SNR and increasing PR was also established. The PR was also found to differ significantly as a function of incidence angle, yielding a higher PR for lower incidence angles.

## 5.2 Segmentation Strategies

In the pursuit of identifying potential zones within oil spills in SAR scenes, some choices must be made. Perhaps the most limiting choice of all is the strategy that actually carries out the final segmentation within the oil slicks. Since the existence of zones within oil slicks in SAR scenes is currently at a hypothetical stage, i.e., not yet established, the number of zones and their respective labels are unknown. Therefore, methods based on unsupervised machine learning is essential. In this thesis, two unsupervised segmentation strategies will be presented, giving rise to a comparative analysis. The first method involves a simple k-means clustering algorithm where the number of predefined classes is based on the framework established in the Bonn Agreement Oil Appearance Code (recall Section (3.2.4)), thereby constraining the number of zones to five. However, in the second approach, the model itself will identify the number of classes. This will be done by using a GMM in combination with a model selection criterion. The upcoming section introduces the concept behind both strategies, and discusses their strengths and weaknesses.

### 5.2.1 K-means Clustering

K-means is an unsupervised clustering technique that partitions observations into a predefined number of clusters based on spatial position in an $l$-dimensional feature space. It is an attractive clustering technique due to its conceptual and computational simplicity. The k-means clustering algorithm is in fact a special case of the Generalized Hard Algorithmic Scheme (GHAS) [79]. The main idea behind GHAS is to initialize a set of cluster representatives, corresponding to the predefined number of clusters, and assign data points to clusters based on distance measures. From the set of clusters formed, new cluster representatives are computed and the data points are once again reassigned. This procedure is iteratively repeated until the cluster representatives become stable, hence the optimal clusters have been reached.

The cost function used for this two-step optimization problem is defined as [79]

$$J(\boldsymbol{\psi}, U) = \sum_{i=1}^{N} \sum_{j=1}^{K} u_{ij} d(\boldsymbol{x_i}, \boldsymbol{\psi}_j), \tag{5.4}$$

where $u_{ij}$ are hard membership coefficients, $N$ is the number of observations in the data set, $K$ is the number of predefined clusters, and $d(\boldsymbol{x}_i, \boldsymbol{\psi}_j)$ is some optional distance measure defined between data point $\boldsymbol{x}_i, \ldots, \boldsymbol{x}_N$ and cluster representatives $\boldsymbol{\psi}_j, \ldots, \boldsymbol{\psi}_K$, in an $l$-dimensional feature space. Recall that data points are assigned to the "most similar" cluster, such that $u_{ij} = 1$ if $\boldsymbol{x}_i$ belongs to $\boldsymbol{\psi}_j$, and 0 else. After the data points have been assign to the closest cluster, each

cluster representative is updated, and data points are once again reassigned. The new cluster representatives are computed by minimizing the cost function, i.e., by solving the derivative of equation (5.4) in the following manner.

$$\begin{aligned} \frac{\partial J(\boldsymbol{\psi}, U)}{\partial \boldsymbol{\psi}_j} &= 0 \\ \frac{\partial}{\partial \boldsymbol{\psi}_j} \sum_{i=1}^{N} \sum_{j=1}^{K} u_{ij} d(\boldsymbol{x}_i, \boldsymbol{\psi}_j) &= 0 \\ \sum_{i=1}^{N} \sum_{j=1}^{K} u_{ij} \frac{\partial}{\partial \boldsymbol{\psi}_j} d(\boldsymbol{x}_i, \boldsymbol{\psi}_j) &= 0. \end{aligned} \tag{5.5}$$

The distance measure used for the k-means clustering scheme is the Euclidean distance defined as [79]

$$d(\boldsymbol{x}_i, \boldsymbol{\psi}_j) = ||\boldsymbol{x}_i - \boldsymbol{\psi}_j||^2, \tag{5.6}$$

where a data point is classified to a specific cluster if the Euclidean distance is smallest for this particular cluster [79]. By inserting equation (5.6) into equation (5.5), and solving with respect to fixed cluster representatives, i.e., individually for each $j \in [1, K]$, the expression becomes

$$\begin{aligned} -\sum_{i=1}^{N} u_{ij}[2(\boldsymbol{x}_i - \boldsymbol{\psi}_j)] &= 0 \\ \boldsymbol{\psi}_j \sum_{i=1}^{N} u_{ij} &= \sum_{i=1}^{N} u_{ij} \boldsymbol{x}_i \\ \boldsymbol{\psi}_j &= \frac{\sum_{i=1}^{N} u_{ij} \boldsymbol{x}_i}{\sum_{i=1}^{N} u_{ij}}, \end{aligned} \tag{5.7}$$

which basically states that the updated cluster representative is equal to the sum of all data points within the cluster divided by the number of data points within the cluster, i.e., the mean (centroid). For $K$ predefined clusters, the algorithm computes $K$ means, hence the name. Keep in mind that this procedure is iteratively repeated until the cluster representatives converges, i.e., becomes stable.

Figure 5.1 shows the step-by-step procedure for the k-means clustering algorithm. In the illustration, circular data points correspond to cluster representatives, while squares are data points. First and foremost, if $K$ number of clusters are predefined, the k-means algorithm initialize $K$ centroids representing each cluster. Further, data points are assigned to the class with the closest centroid. After the data points have been assigned, the centroids are updated with respect to the current data points within each cluster. The data points are again reassigned to the class with the closest centroid. This procedure is repeated until the optimal clusters have been reached.

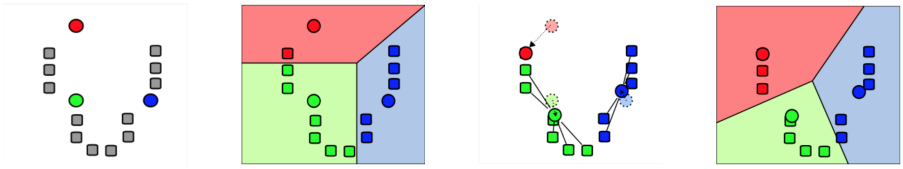

**(a)** Step 1. **(b)** Step 2. **(c)** Step 3. **(d)** Step 4.

**Figure 5.1:** Illustration of the concept behind the k-means clustering method. a) $k = 3$ clusters are predefined, and $k = 3$ initial, arbitrary cluster representatives are generated, b) clusters are formed based upon the position between data points and the cluster representatives, c) new cluster representatives are computed as the centroid/mean by minimizing the cost function, and d) the optimal clusters have been reached by iteratively repeating step 2 & 3 until the cost function is minimized and stable. Figure from [82].

The k-means clustering algorithm has been extensively used for different applications and found quite robust in many cases [11][53]. Skrunes et al. in [71] provided a systematic investigation of eight polarimetric features for the specific purpose of discriminating between mineral oil slicks and monomolecular biogenetic films, and found that k-means performed at least as good as a standard Wishart clustering of the covariance matrix. It is important to note that the clustering technique does not take the underlying statistics of the data into account. Therefore, if the data is assumed to consist of a mixture of distributed classes, k-means might not be the correct approach. The obvious weakness of the method is that the number of cluster must be predefined by the user, and that a poor estimate might prevent the algorithm to unravel the underlying clustering structure [79]. Also, the k-means clustering algorithm search for spherical clusters that are equal in size, which is not necessarily true in most cases. However, this segmentation strategy is still tested in this thesis to see if any reasonable results can be obtained with such a simple method.

### 5.2.2 Gaussian Mixture Model

The GMM is another unsupervised clustering technique that partitions the data into clusters (components) based on fitting a set of sub-distributions into the data. The model is a special case within the field of mixture models, where the set of density components fitted are assumed to be Gaussian distributed. Unlike the k-means algorithm, the GMM is a probabilistic model. However, the GMM is an attractive option for unsupervised clustering as it is relatively fast, simple to understand, computationally tractable, and built-in to many analysis softwares [19][55].

The basic definition of a mixture model can be expressed as [79]

$$p(\boldsymbol{x}) = \sum_{j=1}^{K} p(\boldsymbol{x}|j)P_j, \tag{5.8}$$

where $p(\boldsymbol{x}|j)$ is the *likelihood function* of class $j$ with respect to data point $\boldsymbol{x} \in \{\boldsymbol{x}_1, \boldsymbol{x}_2, ..., \boldsymbol{x}_N\}$, and $P_j$ is the *a priori probability* of class $j$. Further,

$$\sum_{j=1}^{K} P_j = 1, \qquad \textit{and} \qquad \int_{\boldsymbol{x}} p(\boldsymbol{x}|j)d\boldsymbol{x} = 1, \tag{5.9}$$

meaning that the sum of the probabilities for each class must be equal to 1, and that the total class-conditional probability of the data points in $\boldsymbol{x}$ belonging to class $j$ must sum to 1. Hence, by looking at equation (5.8), a mixture model attempts to create a linear combination of $K$ density functions to express the overall density function $p(\boldsymbol{x})$ of the data set.

The unknown parameters of the density functions being fit to $p(\boldsymbol{x})$ can be estimated by the expectation-maximization algorithm with respect to the maximum likelihood method. By assuming statistical independence between the observations within the data, the likelihood function can be expressed as in [79]

$$p(X;\boldsymbol{\zeta}) \equiv p(\boldsymbol{x}_1, \boldsymbol{x}_2, ..., \boldsymbol{x}_N; \zeta) = \prod_{k=1}^{N} p(\boldsymbol{x}_k;\boldsymbol{\zeta}), \tag{5.10}$$

where $\boldsymbol{\zeta}$ represent the unknown parameters estimated from the random samples $X \in \{\boldsymbol{x}_1, \boldsymbol{x}_2, ..., \boldsymbol{x}_N\}$ drawn from $p(\boldsymbol{x};\boldsymbol{\zeta})$. The maximum likelihood method estimates the unknown parameters $\boldsymbol{\zeta}$ with respect to maximizing the likelihood function, that is [79]

$$\hat{\boldsymbol{\zeta}}_{ML} = arg \max_{\boldsymbol{\zeta}} \prod_{k=1}^{N} p(\boldsymbol{x}_k;\boldsymbol{\zeta}). \tag{5.11}$$

The likelihood function is maximized when the gradient with respect to the unknown parameters $\boldsymbol{\zeta}$ is zero. For mathematical convenience, the log-likelihood function is defined due to the monotonicity of the logarithmic function [79]

$$L(\boldsymbol{\zeta}) = \ln \prod_{k=1}^{N} p(\boldsymbol{x}_k; \boldsymbol{\zeta}). \tag{5.12}$$

The estimated unknown parameters $\boldsymbol{\zeta}$ can now be computed by solving the following equation [79]

$$\begin{aligned} \frac{\partial L(\boldsymbol{\zeta})}{\partial \boldsymbol{\zeta}} &= 0 \\ \frac{\partial \ln \prod_{k=1}^{N} p(\boldsymbol{x}_k; \boldsymbol{\zeta})}{\partial \boldsymbol{\zeta}} &= 0. \end{aligned} \tag{5.13}$$

Lets consider the GMM. The log-likelihood function of a finite mixture model, defined as in equation (5.8), can be expressed as

$$L(\boldsymbol{\zeta}) = \sum_{k=1}^{N} \sum_{j=1}^{K} \ln(p(\boldsymbol{x}_k|j; \boldsymbol{\zeta}) P_j), \tag{5.14}$$

where

$$p(\boldsymbol{x}_k|j; \boldsymbol{\zeta}) = \frac{1}{(2\pi)^{l/2}} |\boldsymbol{\Sigma}_j|^{-1/2} \exp\left( -\frac{1}{2} (\boldsymbol{x}_k - \boldsymbol{\mu}_j)^T \boldsymbol{\Sigma}_j^{-1} (\boldsymbol{x}_k - \boldsymbol{\mu}_j) \right) \tag{5.15}$$

for multivariate Gaussian distributions. Here, $\boldsymbol{\mu}_j$ and $\boldsymbol{\Sigma}_j$ represent the unknown mean vector and covariance matrix of class $j$, respectively. The unknown parameters, $\boldsymbol{\mu}_j$, $\boldsymbol{\Sigma}_j$ and $P_j$, can now be iteratively estimated by the two-step expectation-maximization algorithm. The first step involves estimating the expectation of the log-likelihood function in equation (5.14), whereas the second part maximizes the estimated log-likelihood function with respect to each unknown parameter. The desired output of the expectation-maximization algorithm is then $K$ estimated Gaussian density functions with means, variances, and prior probabilities fitted with respect to the data set. The full mathematical derivation of the expectation-maximization algorithm is not within the scope of this thesis, and the reader is referred to [55] and [79] for detailed information concerning this topic. Further, data points are assigned on a probabilistic basis to the Gaussian component (class) that it has the highest posterior probability of belonging to.

Doulgeris in [19] presented a simple and extendable segmentation method for polarimetric SAR images based on a GMM, which produced good, smooth, fast and robust results for image segmentation and interpretation. Further, Espeseth et al. in [22] applied the same method to extract the oil slick masks for their

respective study with success. The advantage of using the GMM compared to the k-means is that it can account for elliptical clusters, i.e., that clusters can have different covariance structures, along with different cluster sizes. Similar to the k-means clustering algorithm, the GMM also requires the number of clusters to be predefined. Luckily, several methods have been developed in order to help determine the number of classes that fits best to the distribution of the data. The Bayesian Information Criterion (BIC) and the Akaike Information Criterion (AIC) have both been extensively used within model selection [30][65][77]. The criteria are quite similar, as they are both based on the optimized negative log-likelihood, but, in general, the BIC penalizes the number of estimated parameters (i.e., the model complexity) harder then the AIC. Consequently, the BIC is biased in favor of simpler models, i.e., models with less components, and might therefore potentially underfit. On the contrary, the AIC criteria might suggest an overfitted model [10][43].

If there in fact exist zones within oil slicks in SAR scenes, the number of detectable zones is expected to be relatively low. Therefore, to prevent the GMM to provide an overestimated model, the BIC score will be the determining factor in this thesis. The BIC score for a fitted mixture model can be defined as [55]

$$BIC = \ln(N)\nu - 2\ln(\hat{L}), \tag{5.16}$$

where $\hat{L}$ is the maximized value of the likelihood function of the model, and $\nu$ is the number of free parameters estimated by the model, i.e., the mean, variance, and prior probability of each Gaussian component. Another restriction is introduced to avoid small classes relative to the size of the data set to be included in the final segmentation. Due to speckle and transitions between regions, the GMM is likely to detect regions of mixed pixels as separate classes in SAR scenes. These "zones" are not of interest, and causes the GMM to obtain models with redundant classes. To avoid this, a merging procedure with resepct to a separability criterion is introduced. This criterion will be used to quantify the separability between the classes provided by the model. The smaller class are then merged with the larger regions that they are most similar to. Hence, only the large prominent classes is outputted. The upcoming section introduces the separability criterion used in this merging procedure.

### 5.2.3 The Jeffries and Matusita Separability Criterion

The Jeffries and Matusita (JM) separability criterion is a common between-class separability measure within pattern recognition and feature selection. The basic concept behind separability measures is to evaluate the proximity between the distribution of different classes. The JM separability measure is valid under the assumption of samples drawn from Gaussian distributions, and

is therefore very well suited for the sake of measuring the separability between the components obtained by the GMM.

If $\boldsymbol{\omega}_i$ and $\boldsymbol{\omega}_j$ are members of a set of classes $i, j = 1, 2, .., K$ where $i \neq j$, then the JM separability criterion is given as [16]

$$JM = 2(1 - e^{-d_{ij}}), \tag{5.17}$$

where $d_{ij}$ is an arbitrary distance measure. In this thesis, the Bhattacharyya distance measure will be used, defined as [4]

$$d_{ij} = \frac{1}{4}(\boldsymbol{\mu}_j - \boldsymbol{\mu}_i)^T(\boldsymbol{\Sigma}_i + \boldsymbol{\Sigma}_j)^{-1}(\boldsymbol{\mu}_j - \boldsymbol{\mu}_i) + \frac{1}{2}log\left(\frac{|\boldsymbol{\Sigma}_i + \boldsymbol{\Sigma}_j|}{2\sqrt{|\boldsymbol{\Sigma}_i\boldsymbol{\Sigma}_j|}}\right). \tag{5.18}$$

This separability measure outputs a value in the range between 0 and 2, where 0 indicates low separability (high similarity) and 2 indicates high separability (low similarity). Figure 5.2 illustrates an example of how the JM will be used in this thesis. Figure 5.2a shows an image containing three regions, i.e., two large regions and one boundary region in between. In this case, it is of interest to merge the boundary region (2) with either of the two larger regions (1 and 3). Figure 5.2b shows the distributions of each region, with the JM between region 1 and 2, and between 2 and 3 indicated. The JM value between region 1 and 2 is higher then for region 2 and 3, i.e., region 2 and 3 are more similar and should therefore be merged. Figure 5.2c shows the resulting structure after merging region 2 and 3.

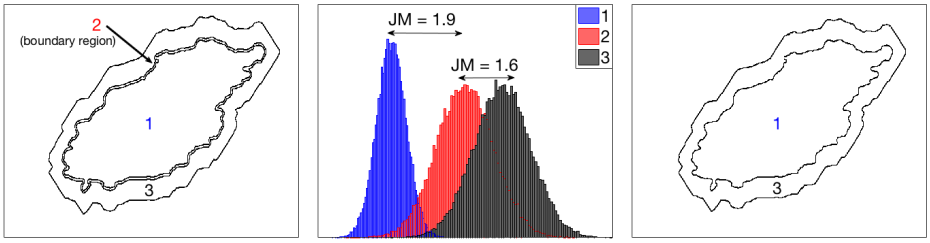


**(a)** **(b)** **(c)**

**Figure 5.2:** Example of using the JM separability criterion to merge boundary regions with their most similar neighboring region. a) image with object containing three regions, i.e., two large regions and one boundary region, b) distribution of the regions with the JM separability indicated, and c) resulting structure after merging.

Carvalho et al. in [9] studied the possibility of segmenting speckled SAR images by using a statistical region growing procedure. This resulted in an overestimated number of small homogenous regions, such that a hierarchical merging procedure in combination with the Kolmogorov-Smirnov (KS) test

was introduced to reduce the number of segments. Li and Chen in [50] used k-means clustering to obtain a large number of clusters in SAR images, followed by a merging procedure based on a similarity measure, a validity measure, and a KS test, and found the method to produced clusters that compared favorable to the actual features in the scenes. The motivation behind the suggested merging procedure in this thesis is similar.

The flowchart below summarizes the most important steps for both segmentation strategies applied in this thesis. The oil slick masks are segmented with the DR as input for both the k-means and GMM. The k-means segmentation is fairly simple, where the output segments are sorted with respect to their average DR, resulting in the class with the highest average DR to have the largest index value. As for the GMM, the BIC score determines which model that should be used, followed by the merging procedure and sorting before the final segmentation is ready. Further, a comparative study between the segmentations obtained from both strategies is conducted.

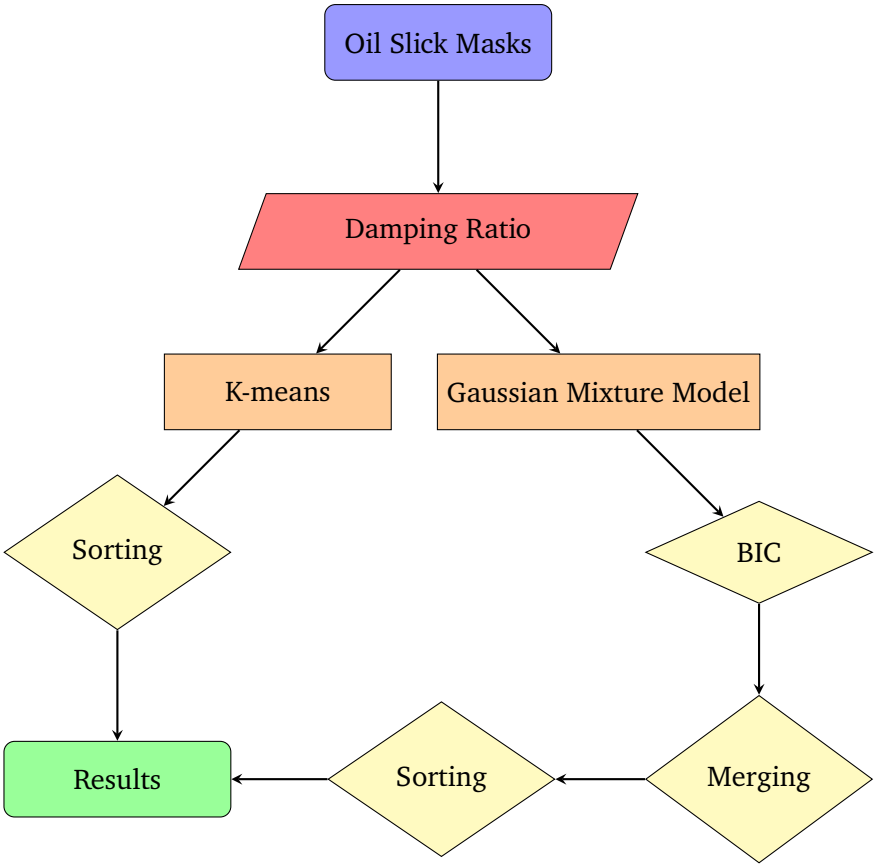


**Figure 5.3:** Flowchart illustrating the most important steps for the within-slick segmentation strategies applied in this thesis.

## 5.3 Oil Slick Features

Immediately after the oil is released into the ocean and continuing throughout its lifetime, it is exposed to forcing from a number of external processes like e.g., weathering, wind and ocean currents, that influence both the physical and radiometric appearance of the slick. As the diversity of oils is rather large, and the fact that their properties varies significantly, it is expected that different oil slicks behave and develop individually. Consequently, it might potentially be possible to recognize certain oil slicks if there exist knowledge about their expected behavior. This is what the second part of this thesis focuses on. It is wanted to examine if there exist certain numerical descriptors, i.e., oil slick features, that are sensitive and/or explain the evolving nature of the oil slicks under observation. These features will be computed with respect to the segmented masks of the oil slicks, and will be studied over a series of acquisitions in search of general trends. The upcoming section presents and discusses each of the features selected.

### 5.3.1 Geometric Features

The features presented in this section are derived directly from the geometry of the oil slick masks, and will be used to study the temporal development of the physical shapes of the oil slicks under observation. Such *geometric features* are often separated in two categories, namely *contour-based* and *region-based* geometric shape description, whereas the first studies the periphery of regions, while the latter includes the total region in the analysis. The geometric features studied in this thesis include the *area*, *perimeter*, *circularity ratio*, and *slick complexity*.

In image processing, the area is a region-based feature defined as the number of pixels contained within a certain region of interest. This feature is simply derived as

$$A = \sum_x \sum_y I(x, y), \tag{5.19}$$

where I(x,y) is a binary image function, and x and y are connected column and row pixels, respectively. For the purpose of analyzing oils in the marine environment, this geometric feature is particularly useful to quantify slick extent and its temporal development. This development is further controlled by weathering processes such as spreading and emulsification, along with the ambient environmental conditions. Therefore, by studying how this geometric feature behaves as a function of time, it might be possible to say something about e.g., the oil viscosity or the oils ability to emulsify (see Section (3.1.2)).

The perimeter is a contour-based descriptor as it describes the extent of the region boundary. It can be defined as [79]

$$P = \sum_{i=1}^{N-1} ||x_{i+1} - x_i|| + ||x_N - x_1||, \tag{5.20}$$

where $x_i$ for $i = 1, 2, ..., N$ are samples on the region boundary. It is difficult to extract any valuable information when studying oil slicks from this feature alone, but in combination with e.g., the area it might be useful. Oil slicks with a small area and small perimeter often have compact, non-complex shapes, whereas a corresponding small area with a large perimeter might indicate a very complex shape. Further, these two geometric features can be combined to define the circularity ratio and the slick complexity, derived as [6][35]

$$R_c = \frac{4\pi A}{P^2}, \tag{5.21}$$

and

$$C = \frac{P^2}{A}, \tag{5.22}$$

respectively.

The circularity ratio, $R_c$, provides an indication of how circular a region is, where a value of 1 correspond to a perfectly circular region and a value of $\sim \pi/4$ correspond to a square. Further, very low values are associated with involuted regions and highly elongated shapes [68]. Jones et al. in [42] found, when studying the same data set as in Data Set 1, that the plant oil rapidly tended towards a more compact and circular shape compared to the emulsions. This behavior is quite interesting, and expected to be detected when studying the temporal development of the circularity ratio for this data set. Intuitively, the slick complexity, $C$, quantifies the complexity of image regions, and is expected to be relatively low for regions with non-complex shapes and high for regions with complex shapes. For the purpose of analyzing oil slicks, this geometric feature is particularly useful to detect fragmented oil slicks with complex shapes, i.e., oil slicks with a lot of branches. By looking at equation (5.21) and (5.22), the circularity ratio and the slick complexity are inversely proportional, and are therefore expected to reveal similar trends to some extent.

As already mentioned in the introductory chapter of this thesis, Skrunes in [68] shed light on the potential of using the area, perimeter and circularity ratio as geometric measures for discrimination between marine targets, whereas Brekke in [6] included the area, perimeter and slick complexity for classification of detected dark spots in SAR scenes. This thesis does not include the regional descriptors for classification purposes, but attempts to find trends in SAR time series with respect to the evolving nature of oil slicks.

### 5.3.2 Geometric Moments

An alternative oil slick descriptor involves geometric moments. Due to the various external impacts, the slicks are likely to translate, rotate and change in size as a function of time. Therefore, the geometric features examined should preferably be invariant under these geometric transformations. However, there exist a set of moments especially developed for invariant pattern recognition. *Hu's seven moments invariants* are in fact invariant under the action of translation, rotation, and scaling [39]. The upcoming section derives these moment invariants.

The seven moment invariants presented by Hu in 1962 originates from the two-dimensional $(p+q)$th order raw moments of a density distribution function $p(\boldsymbol{x}, \boldsymbol{y})$, which can be defined in terms of Riemann integrals as [39]

$$m_{pq} = \int_{-\infty}^{\infty} \int_{-\infty}^{\infty} \boldsymbol{x}^p \boldsymbol{y}^q p(\boldsymbol{x}, \boldsymbol{y}) d\boldsymbol{x} d\boldsymbol{y}, \qquad p, q = 0, 1, 2, \dots, \tag{5.23}$$

where $\boldsymbol{x}$ and $\boldsymbol{y}$ are observations. This can further be adopted to the application of image processing by discretizing, that is [35]

$$\hat{m}_{pq} = \sum_x \sum_y x^p y^q I(x, y), \tag{5.24}$$

where $m_{pq}$ is the 2D $(p+q)$th geometric image moment. Geometric moments are popular features within pattern recognition as they provide rich information about the features within an image. The moments are unique as the information they provide represents the image, and that the image itself can be reconstructed by its moments of all orders [61]. For instance, for the 0th geometric moment, equation (5.24) is equivalent to equation (5.19), thereby providing the area.

The corresponding central moments are defined as [35]

$$\mu_{pq} = \sum_x \sum_y (x - \bar{x})^p (y - \bar{y})^q I(x, y), \qquad where \ \bar{x} = \frac{\hat{m}_{10}}{\hat{m}_{00}} \ and \ \bar{y} = \frac{\hat{m}_{01}}{\hat{m}_{00}}. \tag{5.25}$$

The central moments does not change when regions within an image are shifted, i.e., they are invariant under translation [39]. Further, the normalized central moments can be defined as [79]

$$\eta_{pq} = \frac{\mu_{pq}}{\mu_{00}^{\gamma}}, \qquad where \ \gamma = \frac{p+q+2}{2} \tag{5.26}$$

which are invariant to both translation and scaling. By combining these normalized central moments, Hu defined seven moments invariant under translation,

scaling and rotation. The seven moments are listed below and the reader is referred to [39] for the full derivation.

$$\phi_1 = \eta_{20} + \eta_{02} \tag{5.27}$$

$$\phi_2 = (\eta_{20} - \eta_{02})^2 + 4\eta_{11}^2 \tag{5.28}$$

$$\phi_3 = (\eta_{30} - 3\eta_{12})^2 + (3\eta_{21} - \eta_{03})^2 \tag{5.29}$$

$$\phi_4 = (\eta_{30} + \eta_{12})^2 + (\eta_{21} + \eta_{03})^2 \tag{5.30}$$

$$\begin{aligned}\phi_5 = {} & (\eta_{30} - 3\eta_{12})(\eta_{30} + \eta_{12})\left[(\eta_{30} + \eta_{12})^2 - 3(\eta_{21} + \eta_{03})^2\right] \\ & + (3\eta_{21} - \eta_{03})(\eta_{21} + \eta_{03})\left[3(\eta_{30} + \eta_{12})^2 - (\eta_{21} + \eta_{03})^2\right]\end{aligned} \tag{5.31}$$

$$\begin{aligned}\phi_6 = {} & (\eta_{20} - \eta_{02})\left[(\eta_{30} + \eta_{12})^2 - (\eta_{21} + \eta_{03})^2\right] \\ & + 4\eta_{11}(\eta_{30} + \eta_{12})(\eta_{21} + \eta_{03})\end{aligned} \tag{5.32}$$

$$\begin{aligned}\phi_7 = {} & (3\eta_{21} - \eta_{03})(\eta_{30} + \eta_{21})\left[(\eta_{30} + \eta_{21})^2 - 3(\eta_{21} + \eta_{03})^2\right] \\ & + (3\eta_{12} - \eta_{30})(\eta_{21} + \eta_{03})\left[3(\eta_{30} + \eta_{12})^2 - (\eta_{21} + \eta_{03})^2\right]\end{aligned} \tag{5.33}$$

The 1st and 2nd moments (i.e., $\phi_2$ and $\phi_2$) are a combination of second order normalized central moments, while the remaining moments also include third order normalized central moments. The first six moments are also invariant to reflection, while the 7th moment changes sign. Note that the invariance properties of the moments listed are only approximately true, hence the moments will change slightly under the different geometric transformations [35]. For the sake of the investigation presented in this thesis, Hu's 1st invariant planar moment will be used. This moment holds information about the elongatedness of a region, and Brekke in [6] found this geometric descriptor useful for separating dark features with thin, piecewise elongated shapes and other arbitrary shapes. Further, Skrunes in [68] used the same geometric moment for classifying marine targets, like e.g., ships and icebergs.

Figure 5.4 illustrates the behavior of the circularity ratio, slick complexity, and Hu's 1st planar moment invariant as a function of varying geometric region shape. The circularity ratio seems to detect the circular object perfectly by giving it a value of 1, while decreasing as the geometric shape becomes more elliptical and elongated. The slick complexity and Hu's 1st planar moment invariant provides a remarkably similar trend, and it will be interesting to see how much these parameters correspond when studying more arbitrary shapes.

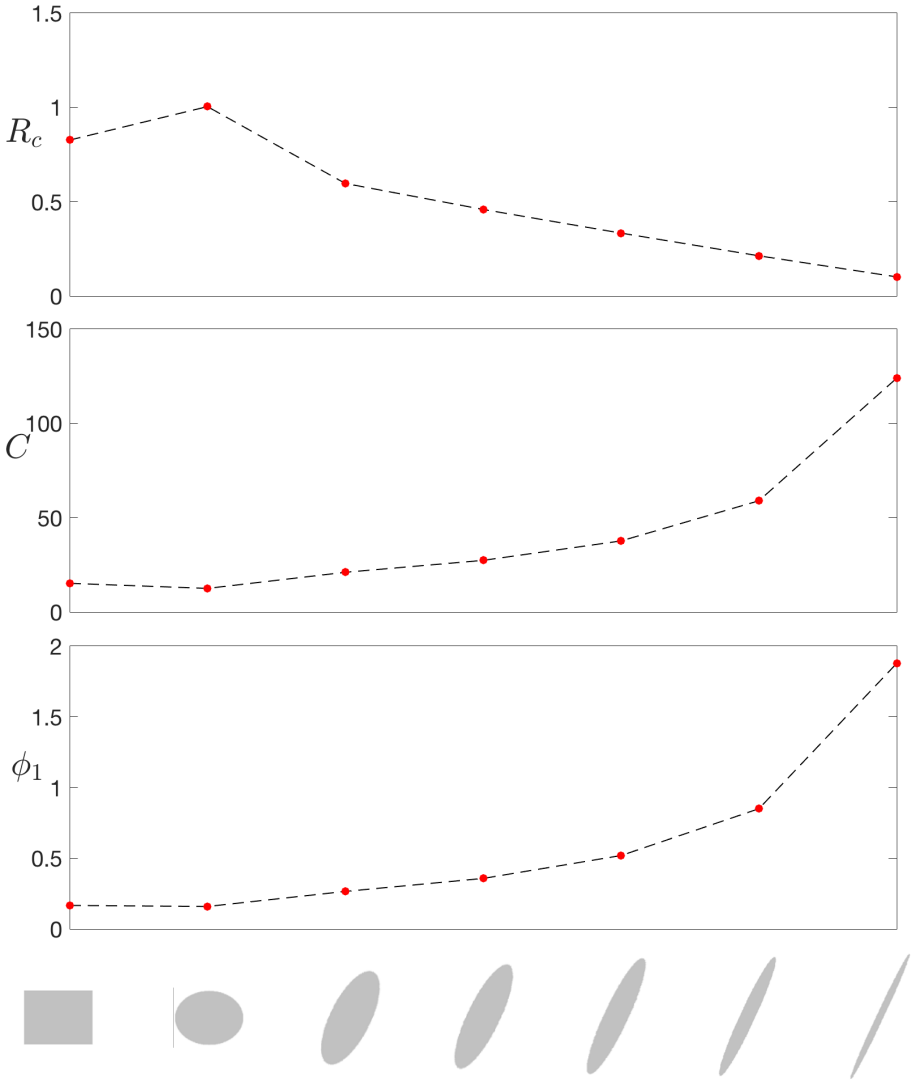


**Figure 5.4:** Behavior of the circularity ratio, slick complexity, and Hu's 1st planar moment invariant as a function of geometric shape.

# 6

# Results and Discussions

This chapter presents the results obtained from the investigation conducted based on the methodology outlined in chapter 5. The suggested segmentation strategies are performed on both data sets, and an effort in detecting potential radar zones is made. Further, the selected geometric region descriptors are computed across all scenes for both data sets, and their temporal development are analyzed for each slick. The first part of this chapter focuses on the radar zone detection scheme, while the second part studies the evolving nature of the slicks. Keep in mind that this thesis works with already detected oil slicks. Hence, no detailed elaboration will be given in exactly how the initial oil slick masks were obtained, besides that it was semi-automatically extracted using the DR as input. In summary, the oil slick mask for the time series acquired during NORSE2015 was extracted using a modified GMM, further elaborated in [18] and [19], whereas a k-means clustering algorithm was used to obtain the masks of the oil slicks in Data Set 2.

## 6.1 Results from the Pilot Study

The pilot project of this thesis focused on investigating properties within an already detected oil spill by an FP SAR system. The sole objective was to examine the possibility of detecting potential zones within oil spills in scenes captured by such a radar system. Two approaches were presented in pursuing evidence backing this hypothesis. The first approach included a progressive morphological segmentation strategy used to inspect the gradient or rate at which the selected polarimetric features, i.e., the DR, PD and PR (see Section (5.1)), changed within the oil slick under observation. The second approach involved a direct within-slick segmentation scheme, providing the basis for a rigorous analysis of how the selected polarimetric features behaved with respect to the segments obtained. Only one scene was studied in the pilot, namely the main slick in the last acquisition in Data Set 2 (see figure 4.5c). The study found tendencies of zoning by studying the internal behavior of the polarimetric features within the slick and the contrast to the surrounding clean ocean. Further, it was insinuated that the number of detectable zones might not necessarily have to correspond to the framework established by optical systems, i.e., the Bonn Agreement Oil Appearance Code using five main class labels.

With respect to detecting potential radar zones, the main extension to the investigation presented in the pilot project is that an additional segmentation strategy is added. This enables a comparative study to be conducted, causing the results to be more credible. The separability measure will not be used to investigate the contrast to the surrounding clean ocean, but more as a processing tool in a merging procedure (recall section 5.2.3). The investigation is also carried out on multiple oil slicks, such that the oil slick zoning detection scheme is tested for various situations. In addition, since the data sets available for this thesis have a relatively high temporal resolution, the evolving nature of the slicks are also studied.

## 6.2 Detection of Potential Radar Zones

In this section, the results obtained when investigating the existence of potential radar zones in SAR scenes are presented. The within-slick segmentations are carried out on both data sets with the DR as input, and a comparative analysis between the final segmentations obtained using the k-means clustering algorithm and the GMM is conducted. Most importantly, the class structures obtained are rigorously evaluated with respect to the ambient environmental conditions, the behavior of the polarimetric features outlined in Section (5.1) and weathering processes, to see if the segmentations potentially reflects the expected internal variations within the slicks. Keep in mind that the k-means is set to search for five classes, while the GMM is set to fit models with a maximum of ten components, as it is unrealistic that oil will contain more zones.

Before the segmentations are carried out, each scene is filtered to reduce speckle. Intuitively, the segmentation will depend on the degree of filtering as it directly alters the spatial resolution. For Data Set 1, i.e., the scenes from NORSE2015, a $9 \times 36$ filter mask is used as these scenes contain relatively small slicks, making them quite sensitive to smoothing. As the scenes in Data Set 2 contained relatively larger slicks, we allow a $15 \times 60$ filter mask to be used for more speckle reduction. An illustration of the segmentation as a function of various filter mask sizes can be viewed in Appendix B for the second acquisition of the main slick in Data Set 2.

Before proceeding, recall some of the general behaviors of oil slicks and potential indicators of oil slick zoning:

- Oil accumulates in the downwind direction where viscous effects dominate the dynamics. Consequently, oil slicks are often experienced to have a relatively well-defined leading edge in the downwind direction, along with a streaky trailing edge in the upwind end of the slick (see Section (3.1.3)).

- Windrows caused by Langmuir circulation are typically observed in the upwind end of oil slicks where the layer of oil is relatively thin (see Section (3.1.3)).

- Oil dampens the capillary waves and decreases the effective dielectric constant on the ocean surface, causing less backscatter to return from oil-infested regions. Hence, the DR is expected to be higher in such oil-infested regions compared to clean ocean, and further increase with oil viscosity and thickness (see Section (5.1.1)). The PR is also expected to be higher in these oil-infested regions compared to clean ocean, and further increase with oil thickness or concentration (see Section (5.1.2)).

### 6.2.1 Results from Data Set 1

This section presents the results concerning the within-slick segmentations of the SAR scenes included in the extensive times series collected during NORSE2015. Recall that the scientific experiment giving rise to this data set involved the release of three mineral oil emulsions with varying oil fraction and a plant oil simulating a biogenetic slick, i.e., E40, E60, E80 and P, respectively. Also, keep in mind the low volume of the releases, i.e., 0.5 $m^3$ for the emulsions and 0.2 $m^3$ for the plant oil, and that the experiment was conducted during relatively high wind (9-11 m/s) coming from a west-southwest direction.

As already mentioned, Jones et al. in [42] also investigated the potential of detecting radar zones by visually inspecting the internal variations of the DR within the oil slicks for this particular data set, and found that zones of thicker oil was identifiable using the VV, HV or HH intensities in the mineral oil emulsions. These zones were only observable in the initial phase after release, and was claimed to most likely be a result of alteration of the surface wave spectrum with different slick thicknesses and not a change in the dielectric properties. It was also concluded that a higher oil content emulsion maintained zoning longest. However, no apparent zoning was observed for the plant oil, potentially caused by the vertical mixing into the water column being so dominant as modeled in [41]. As this data set include 22 acquisitions, only a few scenes will be illustrated to shed light on the overall trend observed, namely the second acquisition captured at 05:46 UTC and the fifteenth acquisition captured at 08:37 UTC. This section discusses the results obtained for the second acquisition first, before proceeding to the latter.

Figure 6.1 and 6.2 shows the k-means and GMM segmentation of the four slicks in the second acquisition, respectively. Note that the effect of the merging procedure is also illustrated for the GMM, where figure 6.2a is the segmentation before, and figure 6.2b represents the final segmentation after the merging procedure is implemented. As can be observed, three of the slicks obtain fewer classes, while preserving much of the same class structure. This demonstrate that the merging procedure works for its intended purpose. The overall impression is that the mineral oil emulsions obtain class structures that might potentially correspond to actual zoning. All the emulsions have a very defined class structure, with a region of relatively high DR located centrally in the slicks, surrounded by continuous region(s) of lower DR. As the oil slicks in this acquisition are relatively fresh, external sources have yet to make any significant impact. It is therefore expected that the denser regions are still located in these central parts, as the oil is still spreading out on the ocean surface. The class structure obtained for the plant oil is more random and discontinuous, and it is hard to see any apparent pattern indicating the presence of zoning.

In general, the GMM provide fewer classes compared to the k-means segmentation, while providing much of the same class structure. This might indicate that the k-means segmentation includes some redundant classes, which is likely a result of the k-means consistently preset to fit five classes. This claim is further supported by studying the behavior of the DR for the k-means segmentation shown in figure 6.1b. The increase from class to class is suspiciously steady, and the standard deviation is more or less equal for all classes. This illustrates the effect of using k-means, which basically forces the fit of five clusters covering approximately the same range. However, it is interesting to see how separable the oil emulsions and the plant oil are. The emulsions are remarkably gathered, with an overall trend of higher DR in each class compared to the plant oil. This is most likely a result of the more significant vertical mixing of oil into the water column for the plant oil, causing less damping on the ocean surface, compared to the emulsions as observed in [41]. This further demonstrates the value of inspecting the internal structures of oil slicks, as a very clear separability between the emulsions and the plant oil can be observed. Proceeding to study the DR for the classes obtained with respect to the GMM, the increases are more significant between classes, and the standard deviation is more varied. As this segmentation strategy in general is less constrained, it is more likely that the classes obtained are more representative.

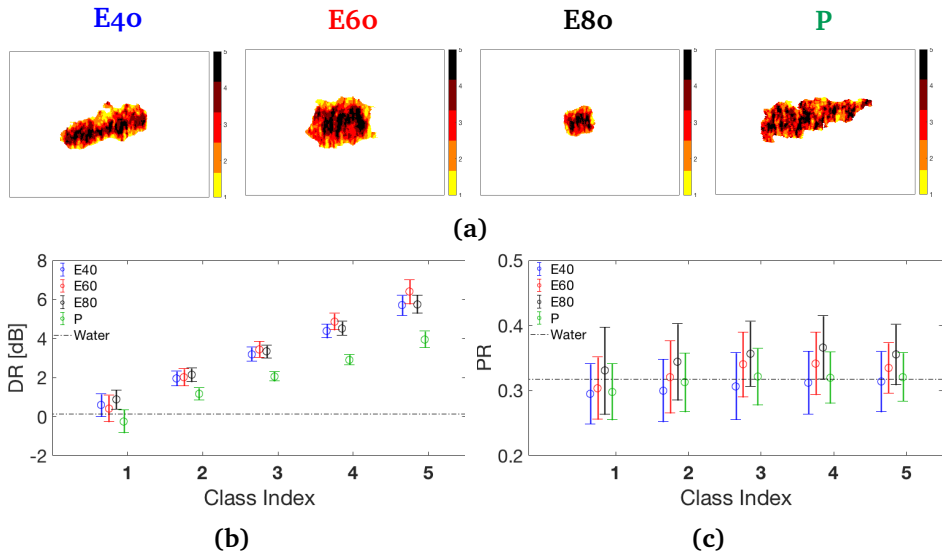


**Figure 6.1:** K-means segmentation of the slicks in the acquisition captured at 05:46 UTC. The segmentations of each slick is illustrated in a), whereas b) and c) shows the behavior of the DR and PR as a function of class index, respectively. The errorbars plotted shows the mean ± 1 standard deviation of the DR/PR, and the dashed line represent the average DR/PR for clean, homogenous ocean.

The behavior of the PR, shown in figure 6.1c and 6.2d for the k-means and GMM segmentation, respectively, does not seem to provide any clear indications of the presence of zoning within the slicks. Here, the errorbars represents the mean ± 1 standard deviation of the DR and PR as a function of class index. Still, some trends are observed. It is interesting to see that the PR in general is higher for the classes in the oil emulsion with the largest oil fraction, i.e., the E80, and further decreases as a function of decreasing oil fraction. Hence, there is seemingly a correlation between increasing oil fraction and increasing PR. Another possible explanation of this behavior might be related to the PR sensitivity to the slicks being located at slightly different incidence angles. However, the value of investigating within the slicks is yet again demonstrated.

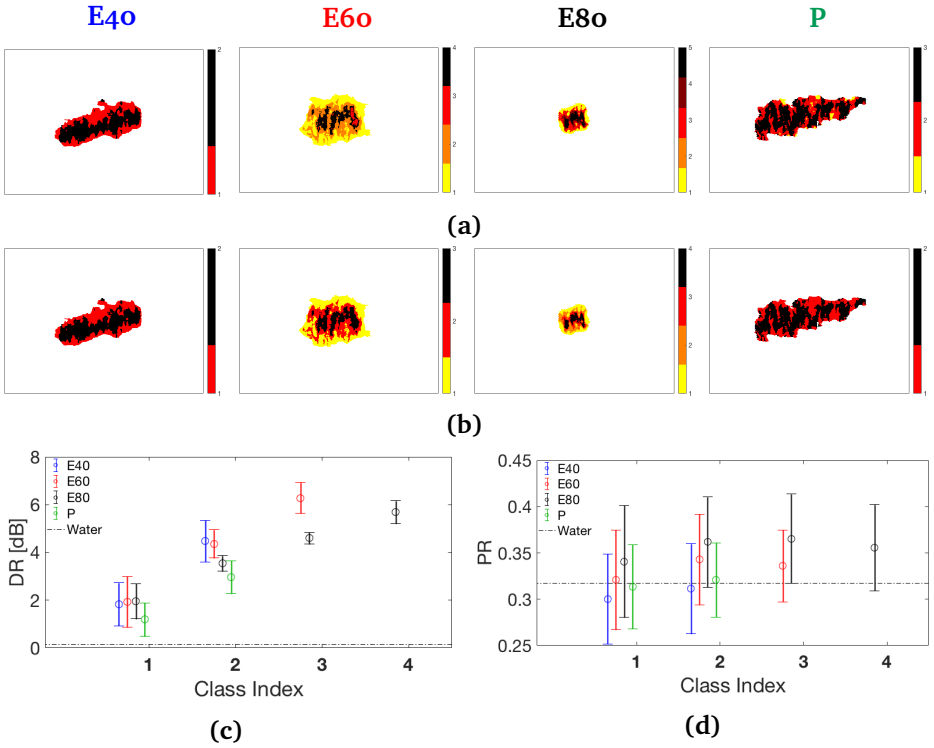


**Figure 6.2:** The corresponding GMM segmentation a) before, and b) after applying the merging procedure for the slicks in the acquisition captured at 05:46 UTC. c) and d) shows the behavior of the DR and PR as a function of class index obtained in b). The errorbars plotted shows the mean ± 1 standard deviation of the DR/PR, whereas the dashed line represent the average DR/PR for clean, homogenous ocean.

The k-means and GMM segmentation of the slicks in the scene acquired at 08:37 UTC, i.e., ~ 3 hours later, is shown in figure 6.3 and 6.4, respectively. As the figures shows, the segmentations are quite chaotic, with no apparent structure that might indicate the presence of zoning, especially for the E40, E60 and P. As for this scene, the classes obtained within the slicks are both discontinuous and fragmented, potentially caused by the slicks exposure to wind and weathering processes. The only slick that might potentially show tendencies of actual zoning is the E80. Here, there seem to exist some region of higher DR stretching out centrally in the slick, especially when studying the GMM segmentation. The impression that this zone in fact correspond to a thicker region of oil is further enhanced when studying the plots showing the behavior of the DR for both segmentations shown in figure 6.3b and 6.4b. Here, this class is clearly indicated with a significant increase in DR. Further, the PR also shows a significant decrease in standard deviation for this particular class compared to the other classes. Hence, this indicate that there might still be at least one zone visible in this slick. This actually correspond well with the findings in [42], where it was found that some zoning was still apparent in the E80 ~ 3 hours after release. Again, the relation between increasing oil fraction and increasing PR is observed.

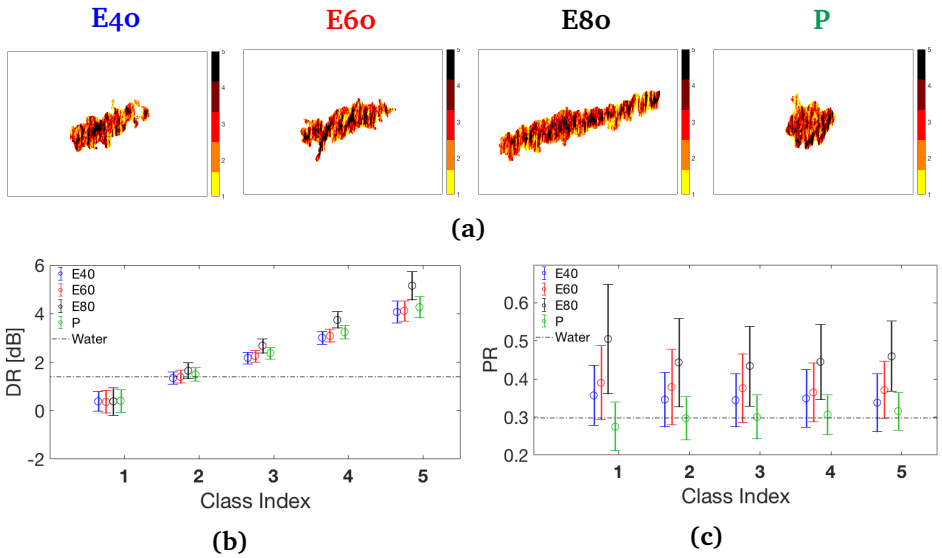


**Figure 6.3:** Overview of the k-means segmentation on the slicks in 08:37 UTC acquisition. The segmentations of each slick is illustrated in a), whereas b) and c) shows the behavior of the DR and PR as a function of class index, respectively. The errorbars plotted shows the mean ± 1 standard deviation of the DR/PR, and the dashed line represent the average DR/PR for clean ocean.

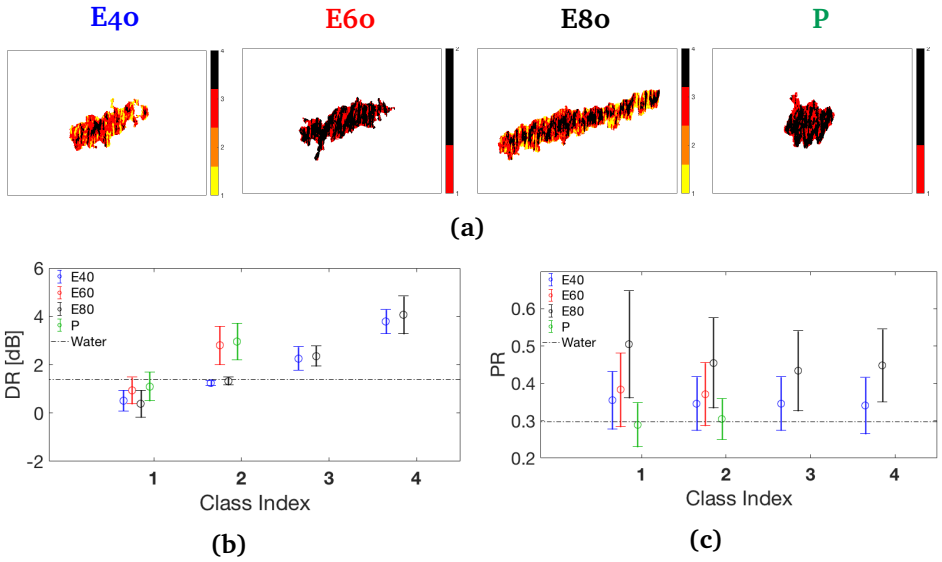


**Figure 6.4:** Overview of the GMM segmentation a) after applying the merging procedure for the slicks in the 08:37 UTC acquisition. b) and c) shows the behavior of the DR and PR as a function of class index obtained in a). The errorbars plotted shows the mean ± 1 standard deviation of the DR/PR, and the dashed line represent the average DR/PR for clean ocean.

To further evaluate the class structures obtained, and either back up or reject the claims made in the previous discussions, a *fake zone* detection scheme is established. The motivation behind introducing this scheme is to see how distinctive the within-slick segmentations are compared to a segmentation of the surrounding clean ocean. Hence, this fake zone detection scheme is based on segmenting a clean, homogenous ocean in the same scene, preferably covering an area of the same order, while spanning over the same incidence angles, for visual comparison. Figure 6.5 illustrates this for the second acquisition captured at 05:46 UTC, where figure 6.5a shows the DR image with a cropped section representing the area segmented by k-means and GMM in figure 6.5b and 6.5c, respectively. In this image, the plant oil is the rightmost slick, followed by the emulsions with increasing oil fraction towards the left. Figure 6.6 illustrates the same for the 08:37 UTC acquisition, but the slicks are now mirrored, i.e., the plant oil is the leftmost slick, due to the 180° difference in heading. Considering the second acquisition, the clean ocean segmentation does not resemble the within-slick segmentations. In fact, the presence of zoning in the oil emulsions, and lack of zoning for the plant oil, is actually apparent just by studying the DR images. As for the acquisition captured at 08:37 UTC, the dissimilarity between the within-slick segmentations and clean ocean segmentation is not as obvious. Here, the DR image does not seem to provide any solid indication of zoning, excluding some darker regions within the E80.

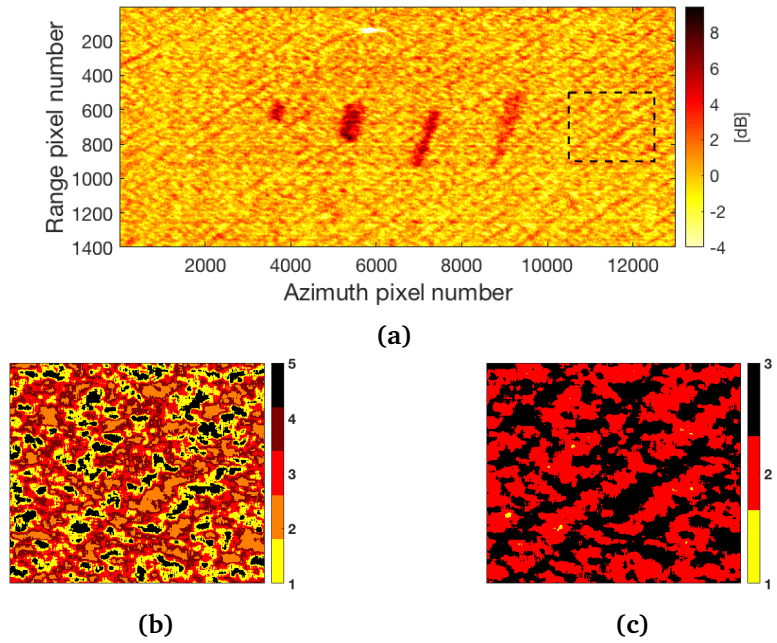


**Figure 6.5:** Result of segmenting clean ocean in the acquisition captured at 05:46 UTC. a) shows the DR image with a cropped section covering clean, homogenous ocean segmented using b) k-means, and c) GMM.

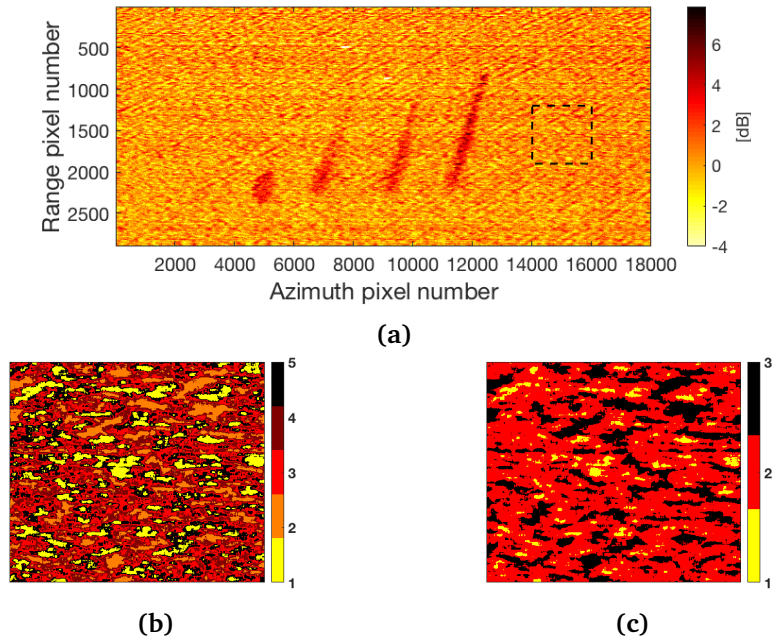


**Figure 6.6:** Result of segmenting clean ocean in the acquisition captured at 08:37 UTC. a) shows the DR image with a cropped section covering clean, homogenous ocean segmented using b) k-means, and c) GMM.

In summary, with respect to the findings and discussion presented above, all the oil emulsions are potentially found to exhibit zoning in the earlier stages after release, exemplified by the results for the second acquisition. Further, the presence of zoning maintained longest for the emulsion with the highest oil fraction, i.e., the E80, where tendencies of zoning was still apparent ~ 3 hours following release. In general, the resulting segmentations of the plant oil did not at any time seem to provide any clear indication of zoning.

The PR did, in some cases, experience a slight decrease in standard deviation for the presumably thickest region of oil, i.e., the zones with the highest DR. Additionally, an increasing trend in PR with increasing oil fraction was observed for the classes obtained for the mineral oil emulsions in both acquisitions. This observation shed light on the potential value of proceeding to investigate the properties within slicks after detection. Further, the DR showed clear trends, and extensive increases between classes that most likely corresponds to actual internal variations within the slicks. Therefore, the zoning observed is most likely a result of variations in damping of the capillary waves, further correlated to oil thickness, and not a result of reduction in the dielectric constant. Additionally, a reasonable separability was observed between the oil emulsions and plant oil in the first acquisition when zoning was still apparent. However, this trend was not observable in the 08:37 UTC acquisition.

The fake zone detection scheme supported the statement made about the slicks in the 05:46 UTC acquisition actually exhibiting zones, as the segmentation obtained for clean ocean deviated a lot from the within-slick segmentations. It also supported the claim saying that the E40, E60 and P did not exhibit zoning in the 08:37 UTC acquisition, as there was a slight similarity between the random patterns observed in the segmentation of clean ocean and within the slicks.

### 6.2.2 Results from Data Set 2

This section presents the within-slick segmentation of the SAR scenes included in Data Set 2. The scientific experiment giving rise to this data set involved the release of two mineral oil emulsions with significantly larger volume (6 $m^3$ and 16 $m^3$ for the test release and main slick, respectively) compared to NORSE2015 (see Section 4.4), and was conducted during calmer wind conditions. Hence, there might be a higher chance of detecting potential zoning within the oil slicks in these scenes.

The k-means and GMM segmentation of the test release and main slick are shown in figure 6.7 and 6.10, respectively. The figures are structured in columns, with the resulting k-means segmentation shown to the left and the corresponding GMM segmentation shown to the right. The slicks are oriented with north pointing upward, and scaled equally to preserve their sizes relative to each other. Also, the ambient wind direction is indicated by the blue arrow, and the flight direction (FD) by the green arrow for each acquisition. The behavior of the DR and PR as a function of classes in the segmentations obtained using k-means and the GMM is shown in figure 6.8 and 6.11 for the test release and main slick, respectively. Here, the errorbars represents the mean ± 1 standard deviation of the DR and PR as a function of class index. In these plots, information with respect to the DR is colored with blue, while the PR is represented by orange. The errorbars with a full line and circular marker represent the classes obtained by segmenting using k-means, whereas the dashed errorbars with a star marker correspond to the segmentation obtained by the GMM. Additionally, a horizontal line plotted in blue and orange represents the average DR and PR for clean, homogenous ocean, respectively. Again, a segmentation of clean, homogenous ocean is provided for visual comparison in figure 6.12, 6.13 and 6.14 for the first, second and last acquisition, respectively. This section starts by presenting the results obtained for the test release, before proceeding to the main slick.

The immediate impression when studying the figures is that both segmentation strategies seem to provide similar class structures for the majority of the slicks, excluding the resulting segmentation of the very first acquisition of the test release (see figure 6.7a and 6.7b). For this particular scene, it is difficult to draw any comparison between the two segmentations as the GMM segmentation provides one major class surrounded by two relatively small regions, whereas the k-means segmentation provides a more detailed structure. This seemingly more detailed structure is most likely a result of the k-means being forced to fit five clusters, thereby chopping the distribution studied into five classes spanning over the same range. Hence, as already mentioned, as the GMM is less constrained it might be more representative. Figure 6.8a shows that the average DR of the classes are large compared to the average DR of clean ocean,

and that the DR increases from class to class for both segmentations. However, this between-class increase is not that significant compared to segmentations discussed later on. As for the PR, it is hard to observe any indications of zoning for this slick in this scene.

Proceeding to the segmentation of the second scene for the test release, shown in figure 6.7c and 6.7d, both segmentation strategies seem to be fairly in agreement on the class structure. The results are quite interesting, as it somewhat resembles something that could be expected with respect to the prevailing wind conditions. There seem to exist a zone of higher DR located centrally, shifted towards the downwind edge of the slick, with fragmenting tendencies in the upwind end. This potentially denser zone of oil is further surrounded by larger, continuous zones of oil with lower average DR, i.e., potentially zones with thinner oil. When studying the behavior of the DR and PR with respect to each class, shown in figure 6.8b, it is clear that the obtained classes are quite distinctive. The average DR within the classes experience a moderate increase from class to class, while preserving a relatively low standard deviation. In addition, the PR also experience a slight increase as a function of increasing class index, with a fairly stable standard deviation for each class.

Moving on to the last acquisition, the test release has changed quite significantly over a period of only 15 minutes. Now, the slick is starting to become quite elongated and fragmented as shown in figure 6.7e and 6.7f. Again, the two segmentation strategies provide very similar class structures, but the GMM has fewer classes. As already discussed, this might indicate that there exist some redundant classes in the k-means segmentation induced by the constraint of consistently seeking five classes. The potentially denser region is still located towards the downwind edge of the slick, while the majority of the potentially thinnest region of oil is located in the upwind end of the slick. This is good, as it shows correlation to the segmentation in the previous scene. The behavior of the DR and PR with respect to each class for both strategies are plotted in figure 6.8c. This time, the DR increases more significantly between the classes, while the PR also shows an increasing trend. This increasing trend is more prominent for the GMM segmentation, which might support the claim of the k-means segmentation having redundant classes. It is interesting that the average PR of the presumably densest zone stands out so clearly, at least with respect to the k-means segmentation.

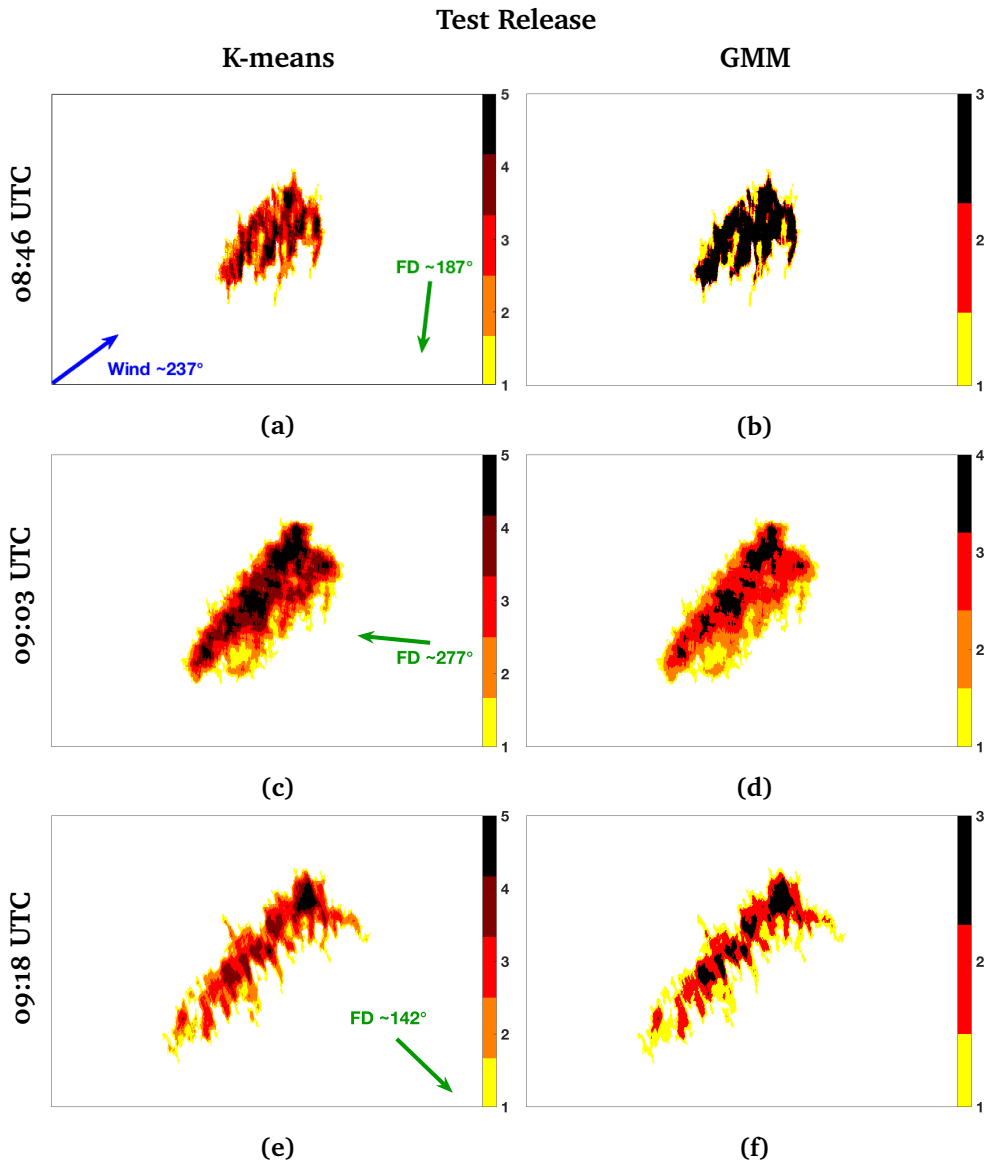


**Figure 6.7:** Overview of the k-means and GMM segmentation of the test release for the acquisitions in Data Set 2 after filtering with a $15 \times 60$ filter mask. The indices on the colorbar shows the colorcoding of the classes, along with the number of classes found by the GMM. Additionally, the images are scaled equally to preserve their sizes relative to each other, and oriented with north point up. The wind direction is indicated by the blue arrow in a) and apply to all scenes, whereas the flight direction (FD) is indicated by the green arrow.

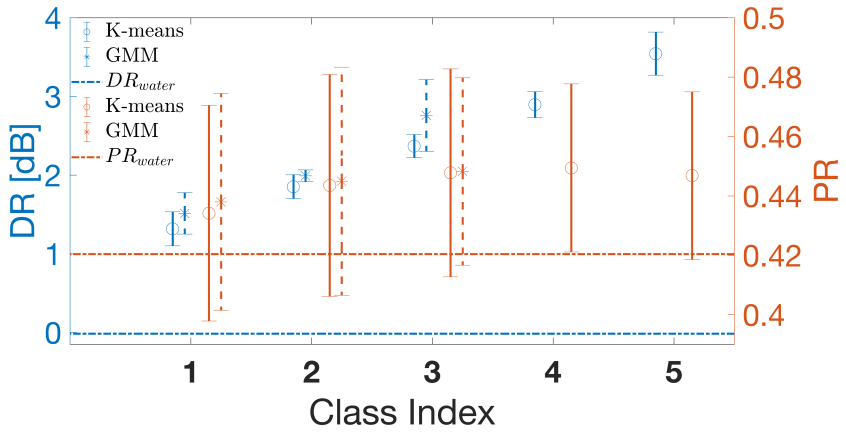


(a)

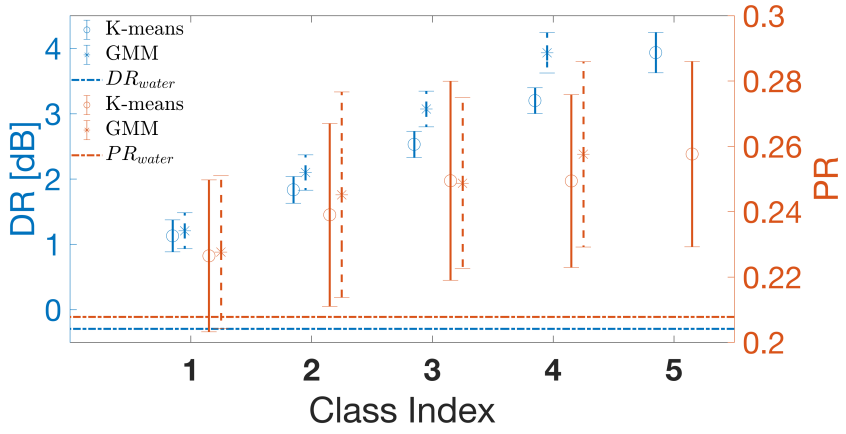


(b)

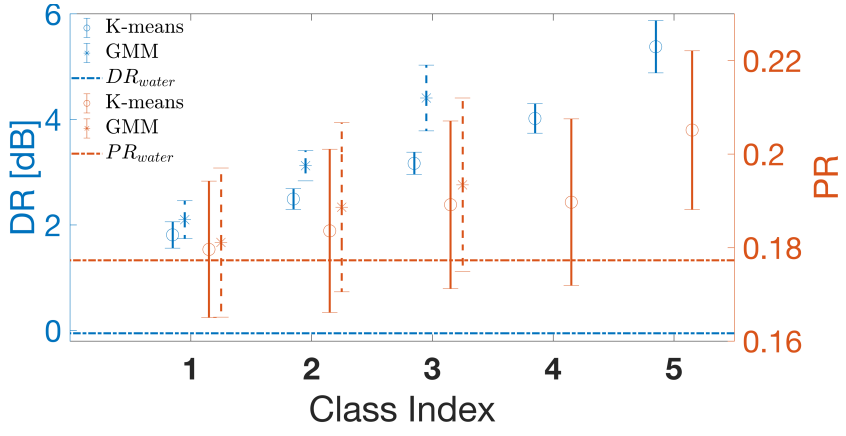


(c)

**Figure 6.8:** Overview of the behavior of the DR and PR as a function of segmentation provided by the k-means and GMM for a) the first acquisition, b) the second acquisition, and c) the third acquisition of the test release in Data Set 2. Information with resect to the DR is colored with blue, while the PR is represented by orange. The errorbars, representing the mean ± 1 standard deviation, with a full line and circular marker correspond the segmentation obtained by k-means, whereas the dashed errorbars with a star marker correspond to the segmentation obtained by the GMM.

The k-means and GMM segmentation of the main slick is shown in figure 6.10, with the behavior of the DR and PR for the classes obtained plotted in figure 6.11. Recall that the release of the main slick ended at 08:53 UTC, i.e., after the first acquisition was captured. Hence, the slick is relatively small in the first scene compared to the two following acquisitions. Despite this, the k-means and GMM provide quite similar class structures for this scene, which resembles something that is expected, with a thicker layer of oil in the center and a potential sheen around the edges. Figure 6.11a shows the behavior of the DR and PR for this scene. The DR increases steadily for the k-means segmentation. Intuitively, the GMM segmentation with one less class, shows a slightly larger increase from class to class. The PR also seem to show a slight increase, especially between class index 3 and 4, and 2 and 3 for the k-means and GMM segmentation, respectively. Additionally, the standard deviation of the PR decrease slightly for the potentially thickest regions of oil, i.e., the region with the highest DR in both segmentations.

Proceeding to the next acquisition, captured 17 minutes later, it is clear that the slick extent and shape has changed significantly. The resulting segmentation of the oil slick mask is shown in figure 6.10c and 6.10d using k-means and the GMM, respectively. Again, both segmentation strategies seem to provide very similar class structures that really resembles the expected internal appearance of the oil slick. The zone with highest DR is pushed towards a very well-defined leading edge in the downwind direction, with regions of thinner oil located in the upwind end of the slick. Such a class structure is expected as oil in general accumulates in the downwind direction leaving behind thinner regions of oil. Further, the behavior of the DR and PR for the different classes obtained is shown in figure 6.11b. The average DR increases quite significantly from the, presumingly, thinnest region of oil to the thickest region of oil. However, in the HH channel for this particular scene, the main slick is contaminated by the signal of a nearby vessel, illustrated in figure 6.9. Hence, since the PR is a function of the HH-channel, the PR will not be discussed for this particular slick in this scene.

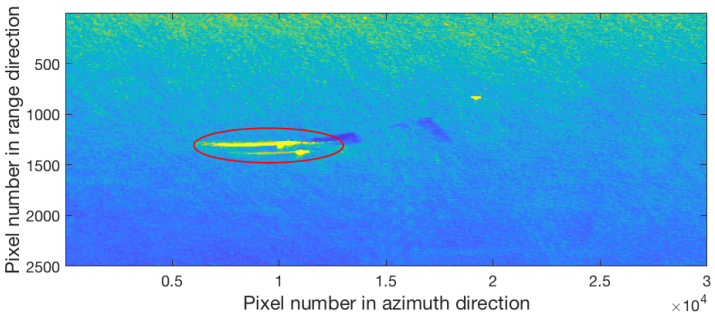


**Figure 6.9:** Intensity image of the HH channel for the 09:03 UTC acquisition in Data Set 2. The red ring marks the smeared out signal from the vessels

The obtained segmentations of the main slick in the final acquisition correlates very well with the segmentation provided for the previous scene discussed above, and is shown in figure 6.10e and 6.10f. The slick continues to increase in size while keeping much of the same shape. The obtained class structures for both segmentation strategies are more or less identical to the naked eye. The slick has, still, a very well-defined leading edge in the downwind direction, with a zone of relatively high average DR accumulated towards it. Consequently, regions of thinner oil are left behind, just as seen in the previous segmentation. The main difference between the segmentation obtained for this scene compared to the previous scene, is that the slick now shows tendencies of being fragmented, both in the outer edge and internally, in the upwind end of the slick. This is potentially caused by Langmuir circulation, which tends to cause such a feathering effect in the upwind end of the slick (see Section (3.1.3)).

By studying the behavior of the polarimetric features with respect to the classes obtained, shown in figure 6.11c, it is apparent that the classes might potentially correspond to actual internal variations within the slick. The DR experience a significant increase as a function of increasing class index, while preserving a relatively low standard deviation. The average PR also seem to increase more for the classes obtained in this segmentation compared to all slicks studied so far in this thesis, while preserving a relatively constant standard deviation. This increasing trend is interesting, as this polarimetric feature is independent of the segmentation and sorting of the classes. In fact, this might indicate that the class structures obtained represent zones of higher damping and a reduction in the dielectric constant. Hence, this observation supports the hypothesis of zoning being detectable within oil slicks in SAR scenes. In summation, as the class structure correlates so well with the segmentation of the previous scene, along with being structured as expected with respect to the prevailing wind conditions, and the fact that the DR and the PR experience such increases between the classes, it is reasonable to believe that the segmentations potentially reflect the internal structure of the oil slick with respect to oil thickness.

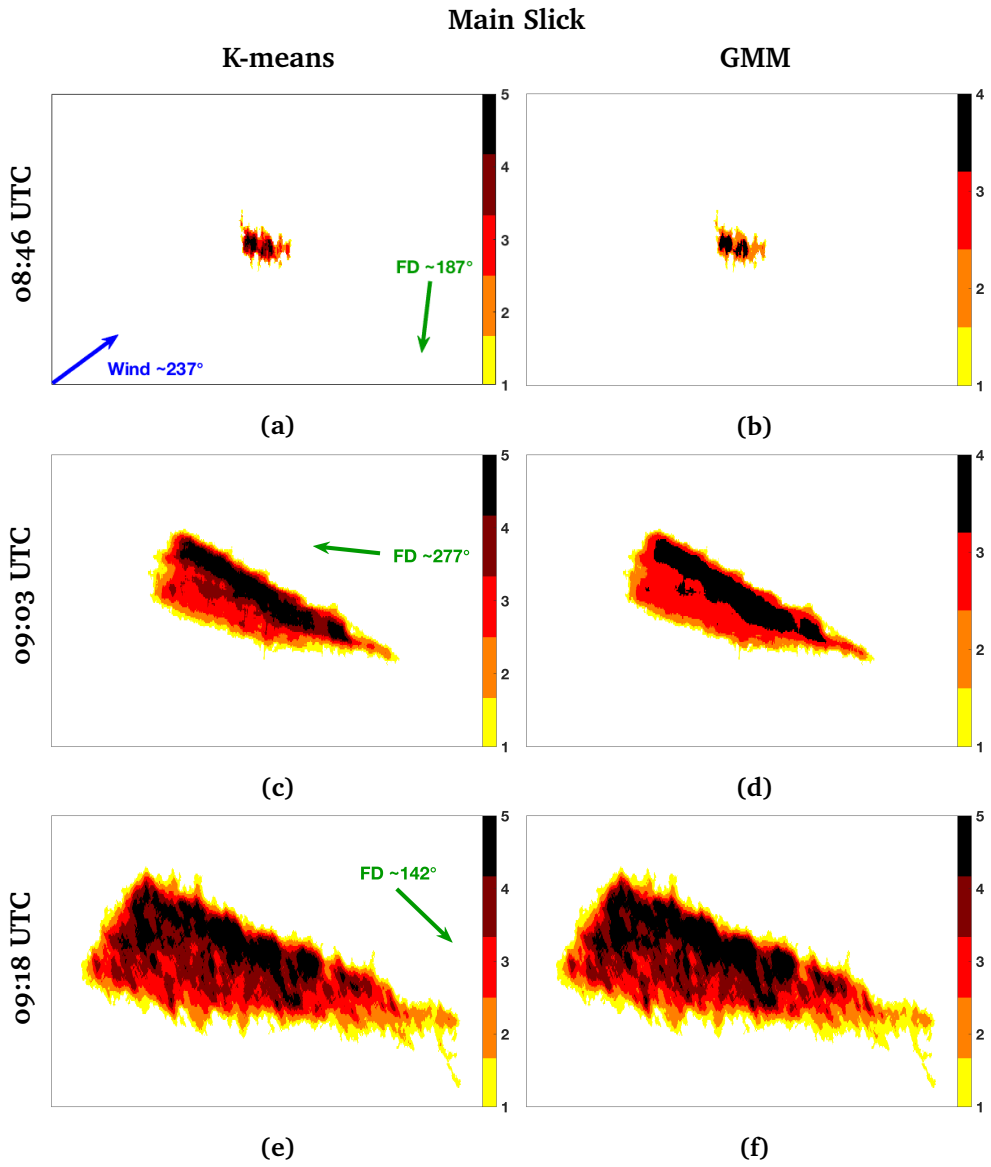


**Figure 6.10:** Overview of the k-means and GMM segmentation of the main slick in Data Set 2 after filtering with a $15 \times 60$ filter mask. The indices on the colorbar shows the colorcoding of the classes, along with the number of classes found by the GMM. Additionally, the images are scaled equally to preserve their sizes relative to each other, and oriented with north point up. The wind direction is indicated by the blue arrow in a) and apply to all scenes, whereas the flight direction (FD) is indicated by the green arrow.

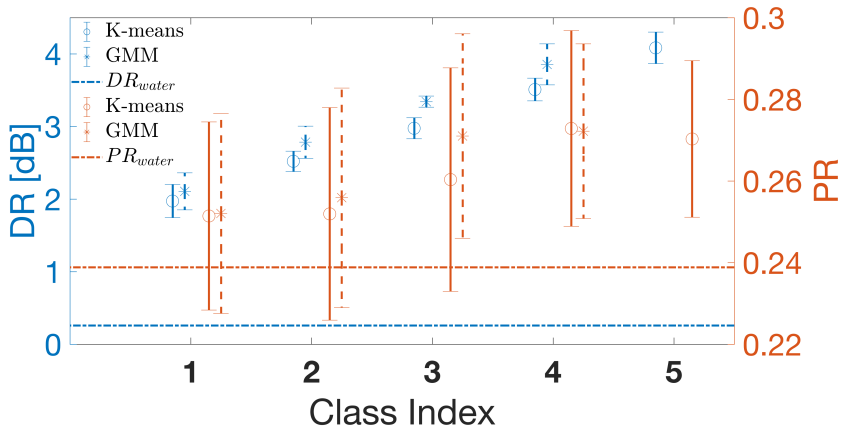


(a)

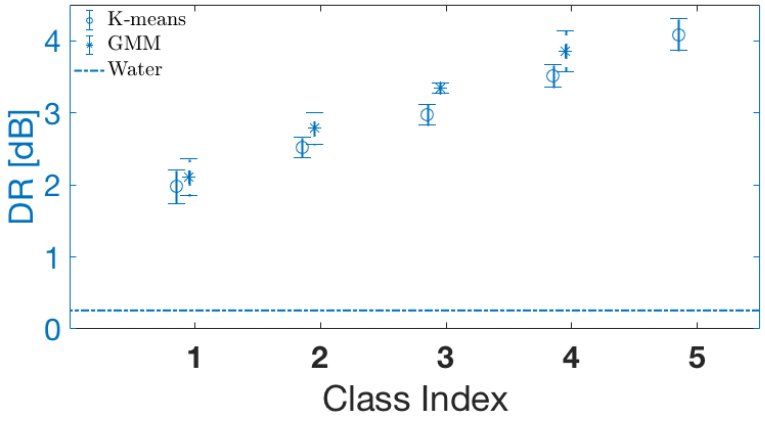


(b)

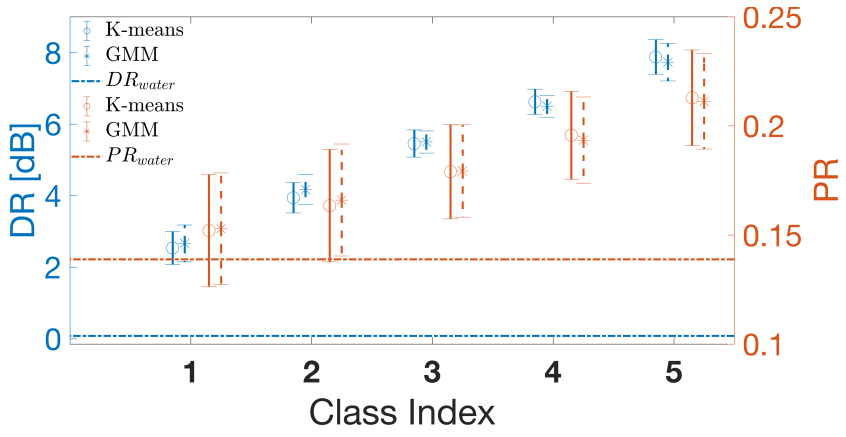


(c)

**Figure 6.11:** Overview of the behavior of the DR and PR as a function of segmentation provided by the k-means and GMM for a) the first acquisition, b) the second acquisition, and c) the third acquisition of the main slick in Data Set 2. Information with resect to the DR is colored with blue, while the PR is represented by orange.The errorbars, representing the mean ± 1 standard deviation, with a full line and circular marker correspond the segmentation obtained by k-means, whereas the dashed errorbars with a star marker correspond to the segmentation obtained by the GMM.

Segmentation of clean, homogenous ocean is yet again provided in figure 6.12, 6.13 and 6.14 for the first, second and last acquisition included in this data set, respectively. Considering the first scene, figure 6.12a shows the DR image with a cropped out section segmented by k-means in figure 6.12b and the GMM in figure 6.12c. Figure 6.13 and 6.14 are structured equally, and illustrates the same for the second and last acquisition, respectively. In general, none of the segmented water regions resembles any of the within-slick segmentations in their corresponding scenes. This support the claims made about the within-slick segmentations of the slicks actually representing internal variations of thickness.

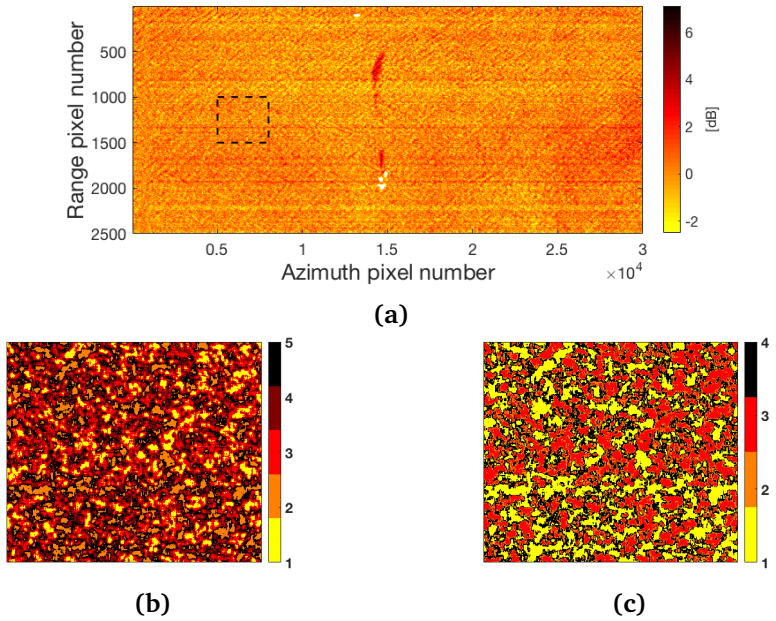


**Figure 6.12:** Result of segmenting clean, homogenous ocean using k-means and GMM in the first acquisition (08:46 UTC). a) shows the DR image with a cropped section segmented by using b) k-means, and c) GMM.

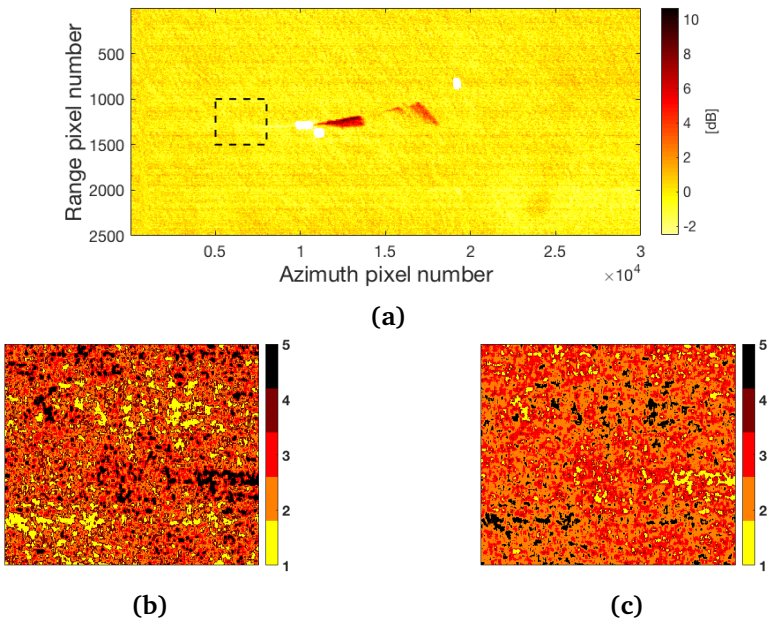


**Figure 6.13:** Result of segmenting clean, homogenous ocean using k-means and GMM in the second acquisition (09:03 UTC). a) shows the DR image with a cropped section segmented by using b) k-means, and c) GMM.

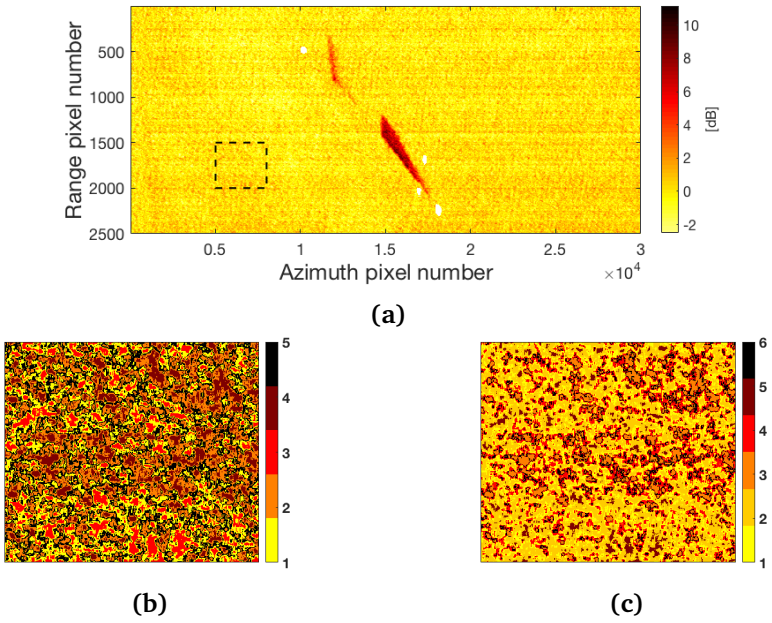


**Figure 6.14:** Result of segmenting clean, homogenous ocean using k-means and GMM in the last acquisition (09:18 UTC). a) shows the DR image with a cropped section segmented by using b) k-means, and c) GMM.

In summary, it is reason to believe that the majority of class structures obtained from the within-slick segmentations of the oil slicks discussed in this section might reflect actual internal variations within the slicks, excluding the very first acquisition of the test release (see figure 6.7a and 6.7b). The k-means and GMM segmentation strategy are both fairly in agreement about the class structures, although the k-means in most cases provides more classes (due to the constrain of seeking five classes). In general, the DR increases with increasing class index, and the increase is observed to be generally higher in the main slick compared to the test release. This is most likely a result of the volumetric differences between the slicks, causing the larger main slick to produce more damping on the ocean surface. However, the PR only seem to react on the, assumed to be, densest zone of oil by either a relatively significant increase in mean value or by a decrease in standard deviation. Especially the segmentation of the second and last acquisition of the main slick provided clear and correlated class structures. Here, the DR varies from ~2 to 8 dB between the outer, thinnest region and the inner, densest region. For the second acquisition of the main slick, the standard deviation becomes much lower for the densest region, whereas the PR shows a steady increase between the classes for the segmentation of the main slick in the last acquisition. Consequently, the classes obtained for this last segmentation of the main slick might reflect zones with both a higher damping and reduced dielectric properties.

## 6.3 Studying the Evolving Nature of the Slicks

The upcoming section presents the results obtained when studying the temporal development of the various geometric features selected (see Section (5.3)) for the slicks in both data sets. The goal of this investigation is to become familiar and form an understanding of how oil slicks evolve as a function of time. Such knowledge can be used to model the fate and behavior of detected oil spills, estimate oil spill lifetimes, and potentially discriminate and classify different oil types as some might act differently. The geometric features are computed across all scenes for the respective slicks, and their behavior is analyzed and discussed in an attempt to observe distinctive trends.

### 6.3.1 Results from Data Set 1

This section presents the results obtained when studying the temporal development of the geometric features over the extensive UAVSAR time series collected during NORSE2015. The geometric features are computed across all scenes for each slick, and can be viewed in figure 6.15-6.19. In these figures, the E40, E60, E80 and P is indicated by blue, red, black, and green, respectively. Additionally, dashed arrows are added on top of the plots to show which flight each acquisition belong to. Still, normal fonts on the x-axis correspond to acquisitions made while ascending, bold fonts represent scenes captured while descending, while the cross-flight acquisition is denoted by a * symbol. This ascending-descending imaging geometry is likely to influence the results as the geometric features are computed with respect to the oil slick masks extracted with the DR as input. Skrunes et al. in [73] investigated the dependency of oil spill observations in polarimetric SAR data on imaging geometry, and found indications of higher DR for mineral oil slicks in scenes captured while looking downwind compared to upwind. Note that the E80 is not represented in the very first acquisition, as the release was not completed before the time of acquisition.

The temporal development of the area is plotted in figure 6.15 for the four slicks. As discussed, the alternating look-direction from scene to scene seems to affect the geometric features quite significantly, shown as the oscillating pattern. In general, the oil emulsions experience a larger increase in area compared to the plant oil, with the E80 tending towards the largest slick extent. As mentioned, since the E80 was released so late, this slick has a very low extent in the earliest acquisitions, but catches up with the other slicks within the first hour. Most of the increase seems to occur in the scenes captured during the first flight (05:32 - 08:53 UTC). In fact, in the second flight (11:45 - 13:18 UTC), the slicks seem to experience a slight decrease in area. Here, the oscillating patterns also become more severe. Jones et al. in [41] observed a similar trend, and resonated that this alternating behavior was most likely a result of the look-direction relative

to the wind direction, as discussed. Why the oscillation becomes more severe for the second flight was not specifically discussed, but a possible explanation is that the slicks become more difficult to segment in these scenes as the slicks have been exposed longer to the ocean surface, thereby being more affected by weathering processes.

As mentioned, the overall trend observed in figure 6.15 is that the oil emulsions tend towards a larger slick extent compared to the plant oil. Hence, this trend might indicate that the emulsions are more affected by spreading compared to the plant oil. This behavior corresponds well with the observations made by Jones et al. in [41], which found that the biogenetic slick simulant (P) was entrained more quickly as the vertical mixing into the water column was more dominant. An even more interesting observation is that the E80 emulsion experiences the largest increase in slick extent, followed by E60 and E40, respectively. Hence, there is seemingly a correlation between higher oil fraction and larger slick extent. This is potentially correlated to the ongoing emulsification of the oil slicks, where the oil emulsion with the highest oil content has the potential of capturing more water, thereby having the opportunity of expanding more.

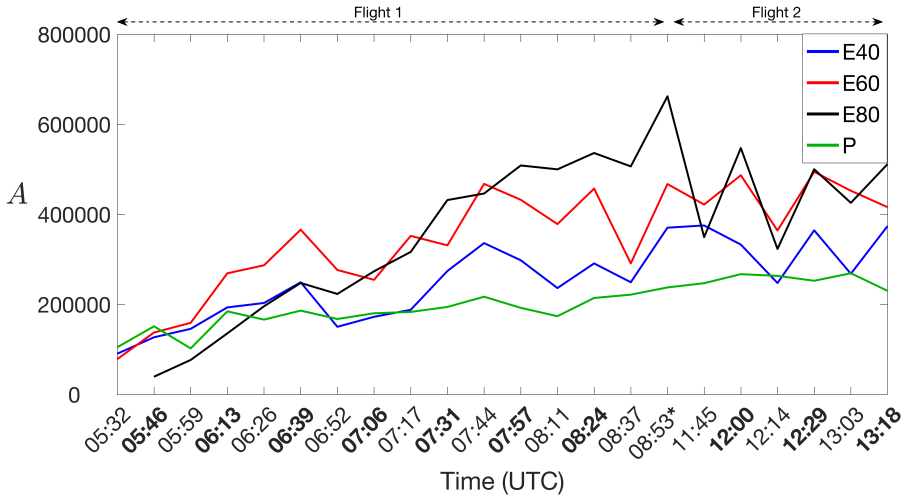


**Figure 6.15:** Overview of the temporal development of the area for the slicks in Data Set 1. The slicks are denoted by color, where blue, red, black and green correspond to E40, E60, E80, and P, respectively. Normal fonts on the x-axis correspond to acquisitions made while ascending, bold fonts represent scenes captured while descending, while the cross-flight acquisition is denoted by a * symbol.

The temporal development of the perimeter, i.e., the length of the oil slick periphery, is plotted in figure 6.16. This geometric feature seems to show much of the same tendency as observed for the temporal development of the area, which is expected as the perimeter is fairly correlated to the area. Intuitively, a large area produces a large perimeter, while a small area results in a small perimeter. However, this is true if the region of interest has a fairly smooth i.e., non-complex shape. Consider a small region of interest with an irregular shape, e.g., with a shape similar to the oil slick mask in figure 6.7e. The total area covered would be relatively small, but the complex shape would lead to a relatively large perimeter. Hence, since the trends are so similar for both the area and perimeter, the shape of the oil slick masks might be fairly smooth. By manual inspection, this is in fact true for the majority of the oil slick masks. As discussed earlier, the oil emulsions spread significantly more out on the ocean surface compared to the plant oil, thereby providing a good separation when studying the temporal development of the area. Consequently, in this case, the perimeter also provides a fairly good separation between the mineral oil emulsions and the plant oil $\sim$ 2 hours after release.

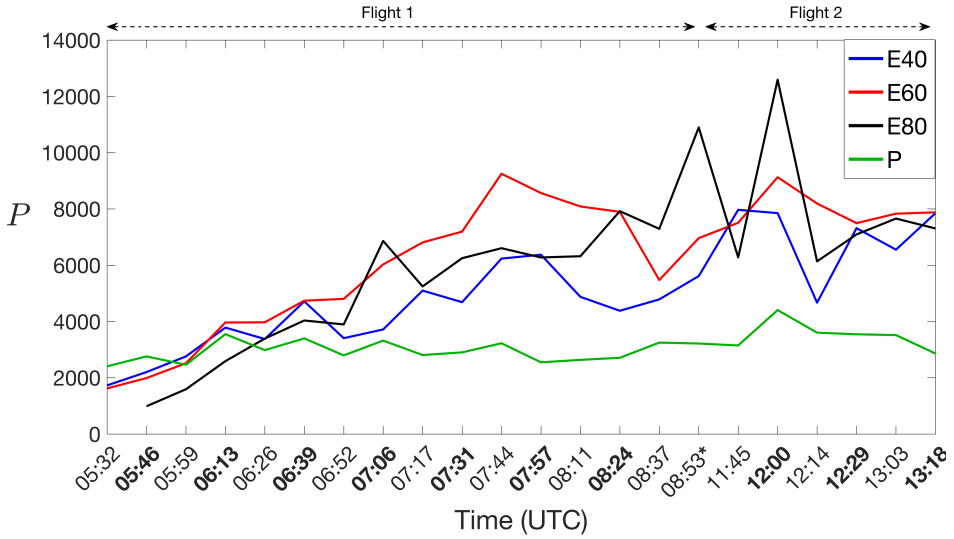


**Figure 6.16:** Overview of the temporal development of the perimeter for the slicks in Data Set 1. The slicks are denoted by color, where blue, red, black and green correspond to E40, E60, E80, and P, respectively. Normal fonts on the x-axis correspond to acquisitions made while ascending, bold fonts represent scenes captured while descending, while the cross-flight acquisition is denoted by a * symbol.

The temporal development of the circularity ratio is plotted in figure 6.17. Recall that this geometric feature is a ratio between the area and perimeter of a region, and expected to say something about how circular a region is. The plot shows that the oil emulsions initially are "more" circular compared to the plant oil. This initial behavior agrees well with the slicks appearances in the intensity images shown figure 4.4, where the oil emulsions are more compact compared to the plant oil. Intuitively, the circularity decreases relatively fast in line with the fact that the emulsions becomes elongated. Recall figure 5.4 that showed a clear connection between increasing elongatedness and decreasing circularity ratio. Hence, this behavior is expected. However, the circularity ratio increases as a function of time for the plant oil. This implies that the plant oil tends towards a more circular and compact shape as time goes by. This correspond well with the observation made in [42], which, as already mentioned, found that the plant oil to rapidly tended towards a more circular shape. As figure 6.17 shows, the circularity ratio provides a clear separation between the mineral oil emulsions and the plant oil 1h 22 minutes after release and throughout the entire time series. In addition, the alternating variations seem more sever for the plant oil compared to the oil emulsions. However, this geometric feature might be suited for the application of separating oil emulsions from biogenetic oil slicks, but further testing is required to validate this.

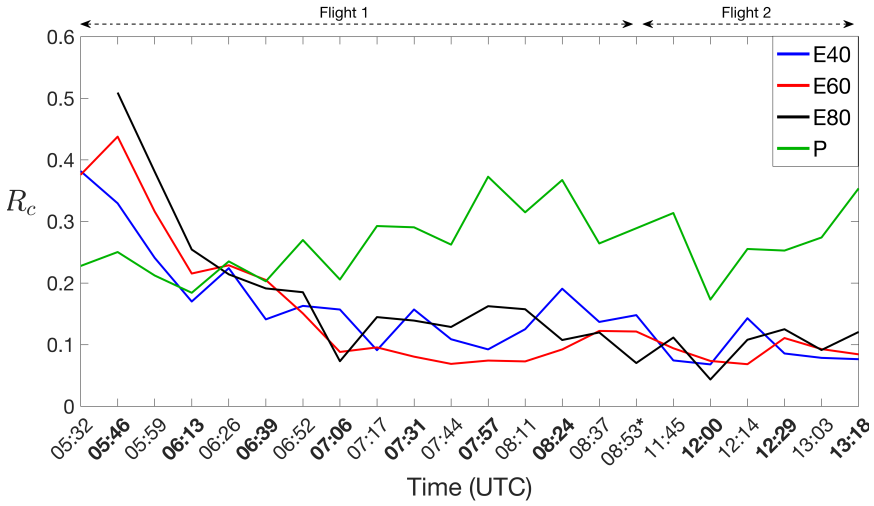


**Figure 6.17:** Overview of the temporal development of the circularity ratio for the slicks in Data Set 1. The slicks are denoted by color, where blue, red, black and green correspond to E40, E60, E80, and P, respectively. Normal fonts on the x-axis correspond to acquisitions made while ascending, bold fonts represent scenes captured while descending, while the cross-flight acquisition is denoted by a * symbol.

Proceeding to the next geometric feature, the temporal development of the slick complexity is studied in this section. As this geometric feature is somewhat inversely proportional to the circularity ratio (see equation (5.21) and (5.22)) discussed in the previous paragraph, it is expected that this feature also provides a reasonable separation between the plant oil and the oil emulsions. The slick complexity is computed across all scenes and plotted in figure 6.18, and, as expected, shows more or less the inverse of the trend observed for the circularity ratio. Initially, all slicks are more or less equally "complex". As time goes by, the oil emulsions experience an increase trend, while the plant oil is more or less stable. Again, this is increasing trend is expected when considering the elongated shapes the oil emulsions tends towards, and the relation illustrated between increasing elongatedness and increasing slick complexity in figure 5.4. The stable slick complexity for the plant oil is most likely a result of the plant oil reaching an equilibrium shape and size relatively fast. Again, the separation between the oil emulsions and the plant oil is very good 1h and 22minutes after release. In this case the alternating variations are more severe for the oil emulsions compared to the plant oil. However, due to the apparent trend observed, this feature might also be suited for separating mineral oil emulsions and plant oil, but further testing is still needed to validate this.

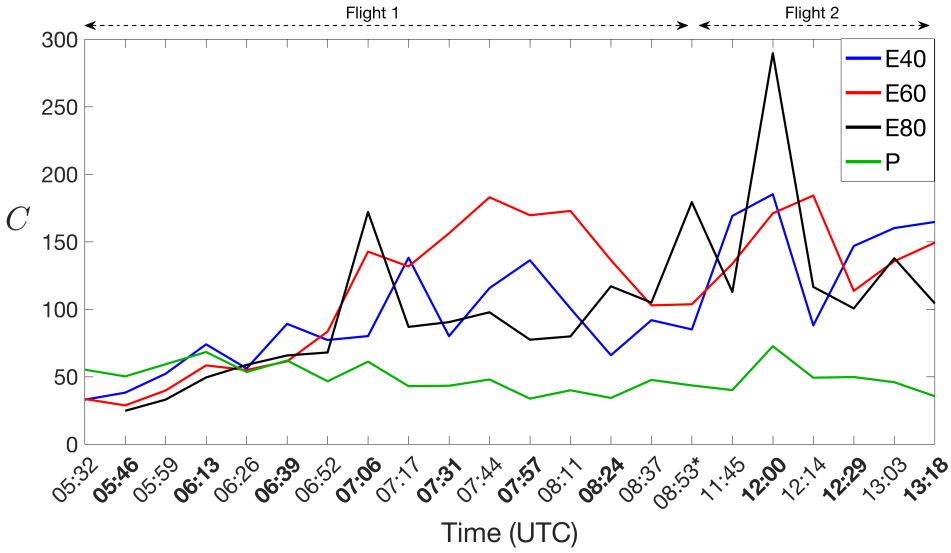


**Figure 6.18:** Overview of the temporal development of the slick complexity for the slicks in Data Set 1. The slicks are denoted by color, where blue, red, black and green correspond to E40, E60, E80, and P, respectively. Normal fonts on the x-axis correspond to acquisitions made while ascending, bold fonts represent scenes captured while descending, while the cross-flight acquisition is denoted by a * symbol.

At last, the temporal development of Hu's 1st planar moment invariant is plotted in figure 6.19. This feature is expected to hold information about a regions elongatedness, and is expected to separate thin, piecewise elongated shapes and other arbitrary shapes. This is not really the case for the slicks studied in this thesis, as no apparent separation is can be observed between the oil emulsions tending towards elongated shapes and the plant oil tending towards a circular shape. The oscillating pattern seem to be less sever across all scenes for this feature, indicating that this feature might not be as affected to the flight tracks, i.e., different look-direction. This is somewhat expected, as this geometric moment is translation, scaling and rotational invariant. What is interesting is how severely this feature react on the cross-flight acquisition, especially for the E80 emulsion. However, it is hard to extract any valuable information from this feature, indicating that this geometric feature might not be suited for this type of sensitivity study.

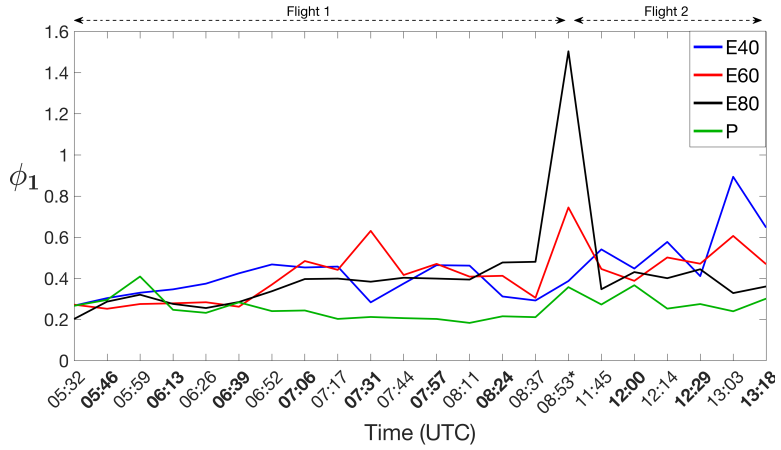


**Figure 6.19:** Overview of the temporal development of Hu's 1st planar moment invariant for the slicks in Data Set 1. The slicks are denoted by color, where blue, red, black and green correspond to E40, E60, E80, and P, respectively. Normal fonts on the x-axis correspond to acquisitions made while ascending, bold fonts represent scenes captured while descending, while the cross-flight acquisition is denoted by a * symbol.

In summary, the area indicated that there might exist a correlation between increasing oil fraction in mineral oil emulsions and increasing slick extent. Further, the perimeter, plant oil, and slick complexity was found to provide a good separation between the emulsions and the plant oil $\sim$ 2 hours following release. In contrast, Hu's 1st planar moment invariant did not provide any interesting trends. The sensitivity of segmenting oil slicks with respect to the DR in upwind/downwind conditions was also indirectly illustrated by the alternating patterns observed for most of the geometric region descriptors.

### 6.3.2 Results from Data Set 2

This section presents the results obtained when analyzing the evolving nature of the slicks in Data Set 2. Since the time series included in this data set only consisted of three acquisitions, it will be hard to deduct any solid conclusions from the trends observed. Nevertheless, the investigation is carried out to verify if the geometric features behaves as expected, and a brief discussion is therefore presented. Figure 6.20 shows the temporal development of all the selected geometric features for both slicks. The blue and red color represent the test release and main slick, respectively.

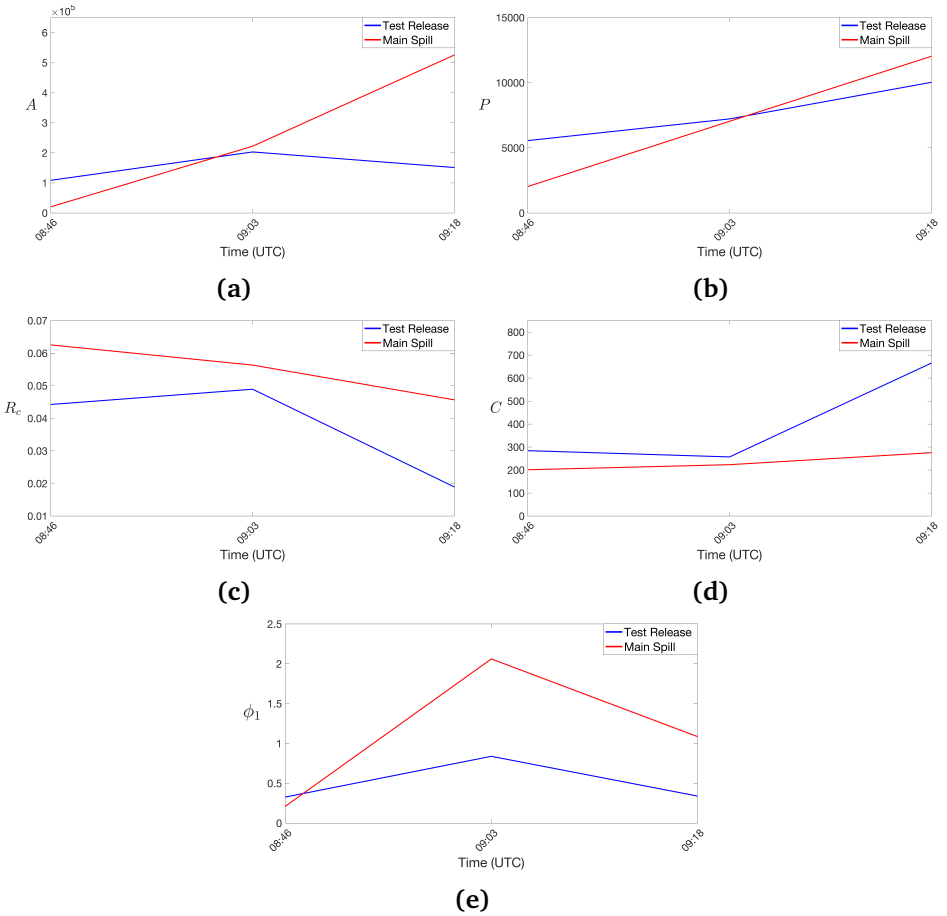


**Figure 6.20:** The temporal development for both slicks in Data Set 2, plotted as a function of the a) area, b) perimeter, c) circularity ratio, d) slick complexity, and d) Hu's 1st invariant planar moment.

The temporal development of the area is plotted in figure 6.20a. The results are quite interesting, showing that the test release is fairly stable in size, with a slight increase followed by a slight decrease over the three acquisitions. However, the main slick experiences an almost linear increase. A possible reason to why this increase is not continuous for the test release might be because of the slicks longer exposure to the ocean surface, causing more forcing from weathering processes. Another, more intuitively, reason arises from the fact that there is a significant difference in volume between the slicks, where the main slick is almost three times larger then the test release (6/16 $m^3$). This implies a larger spread, and also gives the potential of a larger amount being emulsified.

The temporal development of the perimeter, plotted in figure 6.20b seems to show much of the same tendency as for the area. The minor difference is the increase from the second to the last acquisition for the test release. This is most likely caused by the complex shape that the oil slick mask of the test release in this last acquisition has (see figure 6.7e).

The temporal development of the circularity ratio and the slick complexity is plotted in figure 6.20c and 6.20d. The figures are more or less inversions of each other, which is expected by the inverse relation between these parameters. In general, the plot indicates that both slicks tends towards a less circular and more complex shape, which correspond well with the appearance of the oil slicks in figure 4.5, and the isolated oil slick masks which can be viewed in figure 6.7/6.10. The irregular shape of the oil mask of the last acquisition for the test release (again see figure 6.7e) is well detected by the slick complexity, indicated with a large value.

Last but not least, the temporal development of Hu's 1st invariant planar moment is plotted in figure 6.20e. Both slicks seems to behave similarly with respect to this parameter, with an increase followed by a decrease. By studying the oil slick masks shown figure 6.7 and 6.10 for the test release and main slick, respectively, it is hard to explain why. One potential reason might be that the mask of the first and last acquisition for both slicks are generally more irregular, or in other words, the oil slick mask of the second acquisition for both slicks are smoother then in the other acquisitions.

## 6.4 Sensitivity of the Polarimetric and Geometric Features to Segmentation

In this section, the sensitivity of the selected polarimetric features and geometric region descriptors previously discussed are tested with respect to segmentation. The goal is to examine how the features changes with respect to varying looseness/tightness of the masks. The extraction of oil slick masks are in general quite sensitive to the amount of despecke filtering performed, where more smoothing are likely to produce a looser oil slick masks with smoother shapes. Opposite, less speckle filtering is likely to produce a tighter mask with more complex shapes. Segmenting every single slick in every scene with respect to different filter masks would be time consuming, hence another method is proposed. To simulate oil slicks with various sizes and smoothness, a dilation and erosion procedure is introduced. The same progressive morphological method as developed in the pilot project will be used. This thesis will not go into detail on the exact method, but in summary, a structuring element is constructed and applied to the initial masks causing a pixel-by-pixel dilation/erosion in all directions. The main effect of dilation is that the shape of the masks, in addition to becoming larger, tends towards a smoother shape as more dilation is performed. A demonstration of the morphological procedure with respect to dilation is shown in figure 6.21 for the complex mask of the test release in the last acquisition of Data Set 2 (see figure 6.7e/6.7f). Figure 6.21a shows the initial oil slick mask, while figure 6.21b and 6.21c shows the obtained mask when dilating the initial mask with 20 and 40 pixels in all directions, respectively. As the figure shows, more dilation produces a smother shape, as intended. On the contrary, the morphological erosion procedure does not preserve the shape of the region as much as when dilating. This is not a problem when inspecting the polarimetric features, as just a more central area within the slick is desired. However, this might cause problems when studying the sensitivity of the geometric features.

As mentioned, the low number of acquisitions included in Data Set 2 makes it hard to observe any solid trends. Hence, this data set is discarded, and the investigation is only carried out on the extensive time series collected during NORSE2015. In this section, the sensitivity of the polarimetric features, i.e., the DR and PR are considered first, before proceeding to the geometric region descriptors.

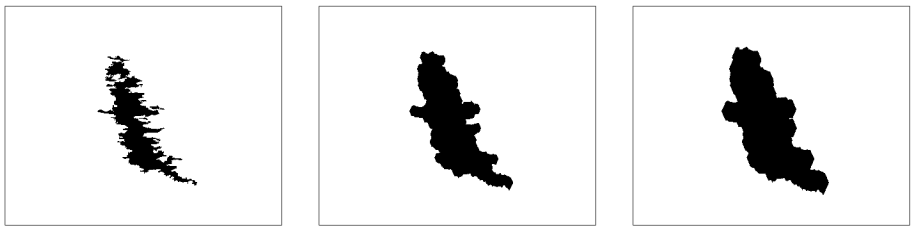

(a) (b) (c)

**Figure 6.21:** Concept of using morphological dilation to expand and smooth oil slick masks. a) shows the initial oil slick mask of the test release in the last acquisition of Data Set 2, b) shows the resulting mask after a 20 pixel dilation, and c) shows the resulting mask after a 40 pixel dilation.

The sensitivity with respect to the oil slick masks of the E80 will be illustrated, as equal trends are observed for the E40, E60 and P. Figure 6.21 illustrates how the average DR and PR changes when varying the looseness/tightness of the E80 masks. The continuous line represents the average DR and PR within the initial oil slick masks, while the red/blue dotted line represent the oil masks after a 20 pixel dilation/erosion, and the red/blue dashed line represents the oil masks after a 40 pixel dilation/erosion. Additionally, a light blue continuous line indicating the average DR and PR for clean ocean, covering the same area while spanning over the same incidence angels, is added for comparison.

As shown in figure 6.22a, the average DR decreases steadily when dilating the mask with 20 and 40 pixels. This is expected as more water pixels are included in the dilated masks. In contrast, the DR increases almost equally when eroding inwards towards central parts of the slicks. Further, the DR of the slicked masks have a significantly larger value compared to the clean ocean. The trend observed demonstrates the sensitivity and importance of the strictness of the oil slick segmentation. There is a significant difference in DR just by introducing a slight dilation and erosion of 20 pixels. Further, the difference between the initial mask and the manipulated masks seem to decreases as time goes by. This is a result of the relative fraction between initial pixels and dilated/eroded pixels decreases as the slick grows. In general, at least for the mineral oil emulsions, the slick extent increases as a function of time, while the pixel dilation/erosion is kept constant. Hence, as an example, the effect of including water pixels by a 20/40 pixel dilation is larger for the relatively smaller oil masks in the initial phase after release. Another interesting observation is that the average DR within the masks decreases as a function of time. This is potentially a result of various weathering processes affecting the oil slick appearance, i.e., the contrast as time goes by. The sensitivity of looking up- and downwind under acquisition with respect to the DR is yet again observed by the alternating pattern, corresponding well with the findings in [73].

However, as shown in figure 6.22b, the average PR is seemingly unaffected by varying the strictness of the oil slick masks. This indicates that the PR does not provide a very good contrast for the slicks studied and the surrounding clean ocean. This is supported by the fact that the light blue line representing the behavior of the PR in clean ocean provide a more or less identical trend. This is potentially correlated to the low amount of oil discharged for each substance, and the relatively rough ambient wind conditions. Again, the upwind/downwind effect is observed. In general, this polarimetric features seem to be more sensitive to the look-direction as the alternation is more apparent, and the fact that the cross-flight acquisition clearly stands out.

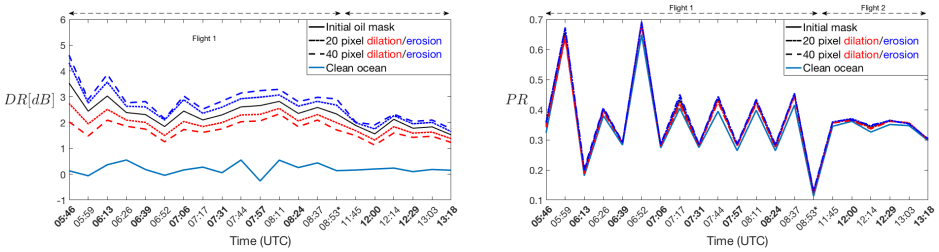


**(a)** **(b)**

**Figure 6.22:** Behavior of the average DR and PR as a function of looser/tighter oil slick masks. The continuous line shows the behavior with respect to the initial oil slick masks, the red/blue dotted line represent the oil masks after a 20 pixel dilation/erosion, and the red/blue dashed line represent the oil masks after a 40 pixel dilation/erosion. In addition, a continuous light blue line is added to represent the behavior of the polarimetric features for clean ocean.

Similarly, the sensitivity of the geometric region descriptors to varying oil slick masks was also investigated. The effect of dilating the masks did not affect the overall trend of the features, as previously shown in figure 6.15-6.19 in Section (6.3.1), any particularly, as the shape in general was very well preserved. On the contrary, as the shape of the masks were severely sensitive to eroding, the results became quite chaotic and incomparable. Hence, no apparent trends were possible to observe, and no conclusions are drawn.

# 7

# Conclusions

This thesis adds to the on-going discussion of the application of multi-polarization SAR data for oil slick characterization (see e.g., [22][42][56][69]). The thesis began with presenting the fundamental theory behind remote sensing by SAR, before embedding it into the application of monitoring marine oil spills in Chapter 3. Further, the data sets available for this thesis was presented in Chapter 4, followed by Chapter 5 which outlined the methodology developed for the investigation presented. At last, the investigation was carried out on the data sets available, and the results were presented and discussed in Chapter 6.

## 7.1 Contributions and Findings

The observations and conclusions drawn from the investigation presented in this thesis are summarized below:

- The availability of detailed and accurate information concerning marine oil spills provides several benefits. Especially information about the internal structure within oil spills can be used to optimize oil spill recovery operations by directing responders to the most crucial areas. The potential of detecting zones within oil spills in multi-polarization SAR scenes was investigated in this thesis by performing a direct within-slick segmentation, using a simple k-means clustering algorithm and a GMM

combined with a merging procedure based upon JM separability. Two data sets were studied with different oil slick properties, captured under different environmental conditions. The results obtained with respect to the extensive time series collected during NORSE2015 were found to limit the hypothesis of the existence of radar zones in the general case, as zoning was only apparent in the mineral oil emulsions for a restricted time period, most likely due to high winds and the low volume of oil released. The emulsion with the highest oil content maintained zoning longest, while the plant oil did not provide any clear indication of zoning during the entire time series. In general, the observations made corresponded well with the findings in [42]. As for Data Set 2, the presence of potential radar zones was well detected, and encourages a more extensive study on more data for detecting oil spill zoning using SAR. The reason why zoning is more prominent in these scenes is most likely due to the significantly higher amount of oil released, and the slightly calmer wind conditions. Further, the value of inspecting internal variations within oil slicks for discrimination purposes was also demonstrated, as tendencies were observed with respect to separating mineral oil emulsions from plant oil.

- The motivation behind using two segmentation strategies was to provide basis for a comparative study between the within-slick segmentations obtained. In general, the simple and more constrained k-means clustering algorithm provided segmentations very similar to the GMM for the majority of the slicks studied in this thesis. As for the GMM, the BIC model selection criteria tended to recommend models with empty and relatively small classes, most likely representing regions of mixed pixels. Consequently, the merging procedure was implemented to entrain the number of zones to a realistic level. Hence, the BIC might not be the best model selection criteria for this application, but the lack of time prevented a thorough study of other criteria. However, future studies should definitely consider using others. The main difference between the two strategies was that the GMM in general outputted fewer classes that seemingly showed much of the same class structures as for the k-means. Hence, the k-means was more prone to include redundant classes, induced by the constrain of consistently seeking five clusters. However, if only a fast and rough estimate of the internal variations within oil slicks is needed, the k-means clustering algorithm might provide sufficient results.

- As no optical imagery was available for verification, an evaluation of the classes obtained by the segmentation strategies was conducted with respect to the DR in the VV channel and the PR, along with the prevailing environmental conditions. The DR provided a clear increase between

classes in the within-slick segmentations assumed to reflect internal variations in oil slick thickness. The PR did not show as prominent trends, but seem to detect the thickest regions of oil in most cases. Further, a fake zoning detection scheme was also established by comparing the obtained within-slick segmentations of the oil slicks to segmentations of clean, homogenous ocean in their respective scenes. This simple extension helped decide whether or not the obtained within-slick segmentations potentially did reflect the wave spectrum at the ocean surface or actual internal variations within the slicks.

- The within-slick segmentations are highly sensitive to the choice of despeckling filter mask, as shown in figure B.1. The trade-off between spatial resolution and denoising is crucial, and the size of the filter mask should therefore be rigorously chosen based on the relative size of the slick in the scene studied.

- A comprehensive understanding of the evolving nature of oil slicks is also of interest for several parties. Multiple dark feature detection schemes have been established for marine applications, but the lack of detailed information about the actual phenomenon observed causes false alarm rates to be high. Satellite imagery provides snapshots of oil spills, with no information about the history and future aspects. Hence, by being familiar with the fate and behavior of various marine oil spills, it might be possible to classify and discriminate between different spills, estimate lifetimes, and predict future behaviors, which potentially might be useful for customizing recovery operations. The temporal development of a set of selected geometric features was studied in this thesis for both data sets available. The results obtained indicated that there seemingly is a correlation between increasing oil fraction for mineral oil emulsion and increasing slick extent during the 8h period of time studied after release. Further, by studying the temporal development of the circularity ratio, a good separation between oil emulsions and plant oil was observed. The slick complexity was also found to provide a reasonable separation between the oil emulsion and the plant oil, and seem to detect complex oil slicks very well.

- The effect of look-direction relative to the wind under acquisition in SAR scenes was clearly observed for both polarimetric features and, consequently, the geometric features. Skrunes et al. in [73] investigated the effect of wind direction and incidence angle on multi-polarization SAR observations, and found that all multi-polarization SAR features investigated, e.g., the DR, PR, PD, etc., had some degree of dependency on the imaging geometry, i.e., incidence angle and look-direction relative to the wind. Similarly, in this thesis, the DR and PR were found to alternate

between scenes with alternating heading (7°/187 °), i.e. alternating look-direction (see figure 6.22). The PR was observed to be more sensitive to upwind/downwind compared to the DR, as the alternations were more severe, and the fact that the cross-flight acquisition clearly stood out. However, the geometric features was also observed to provide alternating patterns, most likely a result of being dependent on the oil slick masks, which again is extracted by using the DR.

- The importance of the looseness/tightness of the oil slick segmentation is demonstrated with respect to the DR and PR. The average DR was observed to decrease when dilating the initial oil slick masks, i.e., when including more clean ocean pixels, while increasing when eroding inwards towards more central regions of the slicks in the extensive time series captured during NORSE2015. However, the PR was not found to deviate at all, indicating a poor contrast between the slicks and the surrounding clean ocean for this particular data set. This is most likely due to the low volume of the releases in combination with the relatively high wind.

## 7.2 Uncertainties

The lack of optical data for verification leads to a speculative investigation with respect to detecting potential radar zones within oil spills, and prevents the opportunity of presenting any firm conclusions. Another common problem within research of remote sensing data is that, often, fundamental information about the targets observed are unknown. As the oil slicks studied in this thesis are deliberately discharged for experimental purposes, their properties and release time is known, along with complementary *in situ* measurements. Hence, few or no uncertainties are directly related to the actual targets under observation. By evaluating potential uncertainties related to the methodology developed, a few comes to mind. The fundamental assumption when using a GMM, is that the data studied is assumed to be Gaussian distributed. Although the within-slick distribution was observed to be somewhat a composition of Gaussians for the slick studied in the pilot project, it is uncertain that this is true in general. The chance of the within-slick segmentation strategies converging towards local minimums instead of global minimums when optimizing will always be there, hence there is a chance of the segmentations being imperfect. In addition, the merging procedure developed might not be sufficiently robust to provide the desired output for all cases investigated in this thesis.

## 7.3 Future Work

There are several possible improvements and extensions to the investigation outlined in this thesis. Most importantly, optical data should be available for verification when pursuing the existence of potential radar zones. The simple and extendable method developed for the investigation in this thesis should also be extensively tested on more data, preferably collected by a variety of airborne and spaceborne SAR sensors. Suggestions to direct improvements on the method develop for the application of detecting zones within SAR scenes might include other finite mixture models assuming non-gaussian distributed data, other model selection criteria, and a more comprehensive merging procedures depending on factors like e.g., shape, in addition to just size and similarity as used in this thesis.

As for studying the evolving nature of oil slicks, the geometric region descriptors selected for the investigation in this thesis should be further tested to potentially reject or build confidence in the observations made in this thesis. Also, there exist an extensive selection of parameters within this field, and many more should preferably be included in future studies.

# Bibliography


[1] Fate of marine oil spills. Technical report, The International Tanker Owners Pollution Federation (ITOPF), 2002.

[2] W. Alpers and H. A. Espedal. "*Oils and Surfactants*" *in Synthetic Aperture Radar Marine User's Manual*. U.S. Department of Commerce, National Oceanic and Atmospheric Administration, September 2004.

[3] V. Barale and M. Gade. *Remote Sensing of the European Seas*. Springer Netherlands, 2008.

[4] M. Basseville. Distance measures for signal processing and pattern recognition. *Signal Processing*, 18(4):349–369, 1989.

[5] V. Bhateja, A. Tripathi, A. Gupta, and A. Lay-Ekuakille. Speckle suppression in SAR images employing modified anisotropic diffusion filtering in wavelet domain for environment monitoring. *Measurement*, 74:246–254, October 2015.

[6] C. Brekke. *Automatic screening of Synthetic Aperture Radar imagery for detection of oil pollution in the marine environment*. PhD thesis, University of Oslo, December 2007.

[7] C. Brekke and A. Solberg. Oil Spill Detection by Satellite Remote Sensing. *Remote Sensing of Environment*, 95(1):1–13, March 2005.

[8] J. B. Campbell and R.H. Wynne. *Introduction to Remote Sensing*. Guilford Press, 5 edition, 2011.

[9] E.A. Carvalho, D.M. Ushizima, F.N.S. Medeiros, C.I.O. Martins, R.C.P. Marques, and I.N.S. Oliveira. SAR imagery segmentation by statistical region growing and hierarchical merging. *Digital Signal Processing*, 20(5):1365–1378, September 2010.

[10] G. Celeux and G. Soromenho. An entropy criterion for assessing the

number of clusters in a mixture model. *Journal of classification*, 13(2):195–212, September 1996.

[11] T. Celik. Unsupervised Change Detection in Satellite Images Using Principal Component Analysis and k-Means Clustering. *IEEE Geoscience and Remote Sensing Letters*, 6(4):772–776, October 2009.

[12] Y. Chan-Su, P. Seong-Min, O. Yisok, and O. Kazuo. An analysis of the radar backscatter from oil-covered sea surfaces using moment method and Monte-Carlo simulation: preliminary results. *Acta Oceanologica Sinica*, 32(1):59–67, January 2013.

[13] S. Cloude. *Polarisation Applications in Remote Sensing*. Oxford University Press, 2010.

[14] National Research Council. *Oil in the Sea III: Inputs, Fates, and Effects*. National Academies Press, 2003.

[15] I.G. Cumming and F.H. Wong. *Digital Processing of Synthetic Aperture Radar data*. Artech House, 2005.

[16] M. Dabboor, S. Howell, M. Shokr, and J. Yackel. The Jeffries-Matusita distance for the case of complex Wishart distribution as a separability criterion for fully polarimetric SAR data. *International Journal of Remote Sensing*, 35(19):6859–6873, October 2014.

[17] W. Dierking. Sea Ice Monitoring by Synthetic Aperture Radar. *Oceanography*, 26(2):100–111, June 2013.

[18] A. P. Doulgeris and T. Eltoft. Scale Mixture of Gaussian Modelling of Polarimetric SAR Data. *EURASIP Journal on Advances in Signal Processing*, 2010(1):874592, November 2009.

[19] A.P. Doulgeris. A simple and extendable segmentation method for multi-polarisation SAR images. *Proc. POLINSAR in Frascati, Italy*, 2013.

[20] M. Drivdal, G. Brostrom, and K. H. Christensen. Wave-induced mixing and transport of buoyant particles: application to the Statfjord A oil spill. *Ocean Science*, 10(6):977–991, December 2014.

[21] C. Elachi and J.J. Van Zyl. *Introduction to the physics and techniques of remote sensing*. John Wiley & Sons, 2006.

[22] M. M. Espeseth, S. Skrunes, C. E. Jones, C. Brekke, B. Holt, and A. P.

Doulgeris. Analysis of Evolving Oil Spills in Full-Polarimetric and Hybrid-Polarity SAR. *IEEE Transactions on Geoscience and Remote Sensing*, 55(7):4190–4210, July 2017.

[23] M.M. Espeseth. Synthetic Aperture Radar Compact Polarimetry for Sea Ice Surveillance. Master's thesis, UiT The Arctic University of Norway, July 2015.

[24] M. F. Fingas. Introduction to Oil Chemistry and Properties. In *Handbook of Oil Spill Science and Technology*, chapter 3, pages 51–59. Gulf Professional Publishing, Boston, February 2015.

[25] M. F. Fingas and C. E. Brown. Review of oil spill remote sensing. *Spill Science & Technology Bulletin*, 4(4):199–208, 1997.

[26] Norwegian Clean Seas Association for Operating Companies. Our operation. `http://www.nofo.no/en/our-operation/`, last checked 31.05.2018.

[27] A. G. Fore, B. D. Chapman, B. P. Hawkins, S. Hensley, C. E. Jones, T. R. Michel, and R. J. Muellerschoen. UAVSAR polarimetric calibration. *IEEE Transactions on Geoscience and Remote Sensing*, 53(6):3481–3491, June 2015.

[28] G. Franceschetti, A. Iodice, D. Riccio, G. Ruello, and R. Siviero. SAR raw signal simulation of oil slicks in ocean environments. *IEEE Transactions on Geoscience and Remote Sensing*, 40(9):1935–1949, September 2002.

[29] F. D. Frate, A. Giacomini, D. Latini, D. Solimini, and W. J. Emery. The Gulf of Mexico oil rig accident: analysis by different SAR satellite images. *In Proceedings of SPIE*, 8179, October 2011.

[30] C. Fratley and A. E. Raftery. How many clusters? which clustering method? answers via model-based cluster analysis. *The computer journal*, 41(8), 1998.

[31] M. Gade, W. Alpers, H. Hühnerfuss, H. Masuko, and T. Kobayashi. Imaging of biogenic and anthropogenic ocean surface films by the multifrequency/-multipolarization SIR-C/X-SAR. *Journal of Geophysical Research: Oceans*, 103(C9):18851–18866, August 1998.

[32] M. Gade, W. Alpers, H. Huhnerfuss, V. R. Wismann, and P. A. Lange. On the Reduction of the Radar Backscatter by Oceanic Surface Films: Scatterometer Measurements and Their Theoretical Interpretation. *Remote Sensing of the Environment*, 66(1):52–70, October 1998.

[33] A. Gasull, X. Fabregas, J. Jiménez, F. Marqués, V. Moreno, and M. A. Herrero. Oil spills detection in SAR images using mathematical morphology. *Proceedings of EUSIPCO*, 1, Januar 2002.

[34] F. Girard-Ardhuin, G. Mercier, F. Collard, and R. Garello. Operational oil-slick characterization by SAR imagery and synergistic data. *IEEE Journal of Oceanic Engineering*, 30(3):487–495, July 2005.

[35] R. C. Gonzalez and R. E. Woods. *Digital Image Processing*. Pearson Education, 3 edition, 2010.

[36] C. A. S. Hanssen. Comparing SAR measurements of natural oil seeps in the Gulf of Mexico with mineral and biological slicks in the North Sea. Master's thesis, University of Tromsø, June 2013.

[37] J. P. Hollinger and R. A. Menella. Oil Spills: Measurements of Their Distributions and Volumes by Multifrequency Microwave Radiometry. *Science*, 181(4094):54–56, July 1973.

[38] B. Holt. "*SAR imaging of the ocean surface*" *in Synthetic Aperture Radar Marine User's Manual*. U.S. Department of Commerce, National Oceanic and Atmospheric Administration, September 2004.

[39] M. Hu. Visual pattern recognition by moment invariants. *IRE transactions on information theory*, 8(2):179–187, February 1962.

[40] The International Tanker Owners Pollution Federation (ITOPF). Fate of oil spills: Weathering. `http://www.itopf.com/knowledge-resources/documents-guides/fate-of-oil-spills/weathering/`, last checked 31.05.2018.

[41] C. E. Jones, K.-F. Dagestad, Ø. Breivik, B. Holt, J. Røhrs, K. H. Christensen, M. M. Espeseth, C. Brekke, and S. Skrunes. Measurement and modeling of oil slick transport. *Journal of Geophysical Research – Oceans*, 121(10), October 2016.

[42] C.E. Jones, M. M. Espeseth, B. Holt, C. Brekke, and S. Skrunes. Characterization and discrimination of evolving mineral and plant oil slicks based on L-band synthetic aperture radar (SAR). *In Proceedings of SPIE*, October 2016.

[43] A. B. Koehler and E. S. Murphree. A Comparison of the Akaike and Schwarz Criteria for Selecting Model Order. *Journal of the Royal Statistical Society. Series C (Applied Statistics)*, 37(2):187–195, 1988.

[44] Kystverket. Testet oljevernberedskap i nordsjøen. http://www.kystverket.no/Nyheter/2015/Juni/Testet-oljevernberedskap-i-Nordsjoen/, last checked 11.04.2018.

[45] Jet Propulsion Laboratory. Uavsar - uninhabited aerial vehicle syntethic aperture radar. https://uavsar.jpl.nasa.gov/technology/, last checked 31.05.2018.

[46] J. Lee and E. Pottier. *Polarimetric Radar Imaging: From Basics to Applications*. CRC Press, 2009.

[47] W. J. Lehr. *Review of modeling procedures for oil spill weathering behavior. In Oil Spill Modelling and Processes*. WIT Press, 2001.

[48] W. J. Lehr and D. Simecek-Beatty. The Relation of Langmuir Circulation Processes to the Standard Oil Spill Spreading, Dispersion, and Transport Algorithms. *Spill Science & Technology Bulletin*, 6(3):247–253, June-August 2000.

[49] A. Lewis. Current status of the BAOAC (Bonn Agreement Oil Appearance Code). Technical report, Netherlands North Sea Agency Directie Noordzee, January 2007.

[50] J. Li and W. Chen. Clustering synthetic aperture radar (SAR) imagery using an automatic approach. *Canadian Journal of Remote Sensing*, 33(4):303–311, June 2007.

[51] Y. Li and Y. Zhang. Synthetic aperture radar oil spills detection based on morphological characteristics. *Geo-spatial Information Science*, 17(1):8–16, 2014.

[52] P. Lombardo and C. J. Oliver. Optimum detection and segmentation of oil-slicks using polarimetric SAR data. *In IEE Proceedings Radar, Sonar and Navigation*, 147(6):309–321, December 2000.

[53] J. Mao and A. K. Jain. Texture classification and segmentation using multiresolution simultaneous autoregressive models. *Pattern Recognition*, 25(2):173–188, February 1992.

[54] D. Massonnet and J.-C. Souyris. *Imaging with Synthetic Aperture Radar*. CRC Press, May 2008.

[55] G. McLachlan and D. Peel. *Finite Mixture Models*. John Wiley & Sons, 2004.

[56] B. Minchew. Determining the mixing of oil and sea water using polarimetric synthetic aperture radar. *Geophysical Research Letters*, 39(16):16607–, August 2012.

[57] B. Minchew, C. E. Jones, and B. Holt. Polarimetric analysis of backscatter from the deepwater horizon oil spill using L-band synthetic aperture radar. *IEEE Transactions on Geoscience and Remote Sensing*, 50(10), October 2012.

[58] A. Moreira, P. Prats-Iraola, M. Younis, G. Krieger, I. Hajnsek, and K. P. Papathanassiou. A tutorial on synthetic aperture radar. *IEEE Geoscience and Remote Sensing Magazine*, 1(1), March 2013.

[59] American Society of Chemical Engineers Task Committee on Modeling of Oil Spills. A state-of-the-art review of modeling transport and fate of oil spills. *Journal of Hydraulic Engineering*, 122(11), 1996.

[60] C. Oliver and S. Quegan. *Understanding Synthetic Aperture Radar Images*. SciTech Publishing, 2004.

[61] A. Papoulis. *Probability, Random Variables, and Stochastic Processes*. McGraw-Hill, 3rd edition, 1991.

[62] N. Pinel, C. Bourlier, and I. Sergievskaya. Two-dimensional radar backscattering modeling of oil slicks at sea based on the model of local balance: Validation of two asymptotic techniques for thick films. *IEEE Transactions on Geoscience and Remote Sensing*, 52(5), May 2014.

[63] M. Reed, Ø. Johansen, P. J. Brandvik, P. Daling, A. Lewis, R. Fiocco, D. Mackay, and R. Prentki. Oil spill modeling towards the close of the 20th century: Overview of the state of the art. *Spill Science & Technology Bulletin*, 5(1), 1999.

[64] A. Reigber, M. Jager, J. Fischer, R. Horn, R. Scheiber, P. Prats, and A. Nottensteiner. Performance of the L- and P-band subsystems of the F-SAR airborne SAR instrument. In *EUSAR 2012; 9th European Conference on Synthetic Aperture Radar*, pages 286–289, April 2012.

[65] K. Roeder and L. Wasserman. Practical bayesian density estimation using mixtures of normals. *Journal of the American Statistical Association*, 92(439), 1997.

[66] Henrik Rye. Probable effects of langmuir circulation observed on oil slicks in the field. *Spill Science & Technology Bulletin*, 6(3):263–271, 2000.

[67] D. Schmidt-Etkin. Spill Occurrences: A World Overview. In M. F. Fingas, editor, *Oil Spill Science and Technology*, pages 7 – 48. Gulf Professional Publishing, Boston, 2011.

[68] S. Skrunes. Marine Target Characteristics in Satellite SAR Imagery. Master's thesis, UiT The Arctic University of Norway, February 2011.

[69] S. Skrunes. *Characterization of Low Backscatter Regions in the Marine Environment by Multipolarization C-and X-band Synthetic Aperture Radar Data*. PhD thesis, University of Tromsø, July 2014.

[70] S. Skrunes, C. Brekke, and A. P. Doulgeris. Characterization of low-backscatter ocean features in dual-copolarization SAR using log-cumulants. *IEEE Geoscience and Remote Sensing Letters*, 12(4), April 2015.

[71] S. Skrunes, C. Brekke, and T. Eltoft. Characterization of marine surface slicks by Radarsat-2 multipolarization features. *IEEE Transactions on Geoscience and Remote Sensing*, 52(9), September 2014.

[72] S. Skrunes, C. Brekke, T. Eltoft, and V. Kudryavtsev. Comparing near-coincident C- and X-band SAR acquisitions of marine oil spills. *IEEE Transactions on Geoscience and Remote Sensing*, 53(4), April 2015.

[73] S. Skrunes, C. Brekke, C. E. Jones, M. M. Espeseth, and B. Holt. Effect of wind direction and incidence angle on polarimetric SAR observations of slicked and unslicked sea surfaces. *Remote Sensing of Environment*, 213:73–91, 2018.

[74] S. Skrunes, C. Brekke, C. E. Jones, and B. Holt. A multisensor comparison of experimental oil spills in polarimetric SAR for high wind conditions. *IEEE Journal of Selected Topics in Applied Earth Observations and Remote Sensing*, 9(11):4948–4961, November 2016.

[75] A. Solberg. Remote sensing of ocean oil-spill pollution. *Proceedings of the IEEE*, 100(10), 2012.

[76] A. Solberg, C. Brekke, and P. O. Husoy. Oil spill detection in Radarsat and Envisat SAR images. *IEEE Transactions on Geoscience and Remote Sensing*, 45(3):746–755, March 2007.

[77] G. Soromenho. Comparing approaches for testing the number of componenets in a finite mixture model. *Computational Statistics*, 9(1), 1993.

[78] W. Taylor and M. Boerner. Basic concept in radar polarimetry. *PolSARpro*

*Lecture Notes 3*, 2007.

[79] S. Theodoridis and K. Koutroumbas. *Pattern Recognition*. Elsevier, 4 edition, 2009.

[80] F. T. Ulaby, R. K. Moore, and A.K Fung. *Microwave remote sensing: Active and passive. Volume 2-Radar remote sensing and surface scattering and emission theory*. Artech House Inc, 1982.

[81] G. R. Valenzuela. Theories for the interaction of electromagnetic and oceanic waves—a review. *Boundary-Layer Meteorology*, 13(1), January 1978.

[82] Wikipedia. K-means clustering. `https://en.wikipedia.org/wiki/K-means_clustering`, last checked 31.05.2018.

[83] V. Wismann, M. Gade, W. Alpers, and H. Huhnerfuss. Radar signatures of marine mineral oil spills measured by an airborne multi-frequency radar. *International Journal of Remote Sensing*, 19(18), 1998.

# Appendices

# A Correlation Test: Damping Ratio vs. Copolarization Difference

The Person's correlation coefficient measures the strength of the linear correlation between two variables [23]. The coefficient varies from 1 to $-1$ [79], where 1 indicate a perfect positive linear correlation, 0 is no linear correlation, and $-1$ is a perfect negative linear correlation between the variables studied. Figure A.1 shows scatter plots between the DR and PD for both oil slicks over the three acquisitions in Data Set 2. The figure is structured in rows, where the blue scatter plots represent the test release, while the red scatter plots represent the main slick over the three acquisitions. Additionally, the Pearson's correlation coefficient is added in the subcaption of each figure to quantify their correlation. As the figures and their respective subcaptions indicate, the DR and PD shows a high, negative linear correlation for the majority of the slicks.

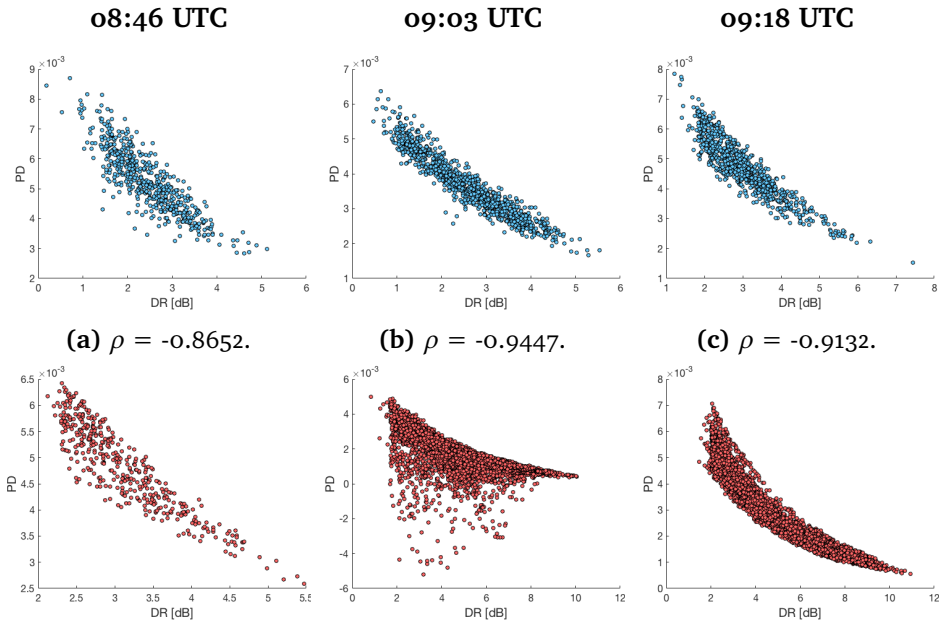


**(a)** $\rho$ = -0.8652. **(b)** $\rho$ = -0.9447. **(c)** $\rho$ = -0.9132.

**(d)** $\rho$ =-0.9113. **(e)** $\rho$ = -0.6030. **(f)** $\rho$ = -0.9492.

**Figure A.1:** Scatter plot showing the correlation between the DR and PD for the scenes in Data Set 2. The blue scatter plots correspond to the test release, while the red scatter plot correspond to the main slick. The time of acquisition is labeled above each column of figures. The Persons correlation coefficient between the DR and PD is added in the subcaption of their respective plots.

# B Filter Mask Dependency on the Within-Slick Segmentation

The importance of the descpeckling filter mask size is demonstrated for the main slick in the second acquisition (09:03 UTC) of Data Set 2 in figure B.1. The figure is vertically structured with the segmentation strategy labeled for each column, along with the size of the filter masks indicated in the subcaption. The results deviates much across the different filter masks, where larger masks results in smoother and more uniform class structures. Consequently, a significant amount of detail is lost. The $15 \times 60$ filter mask seems to provide the best trade-off between noise reduction and preservation of spatial resolution, and will therefore be used for the scenes in Data Set 2.

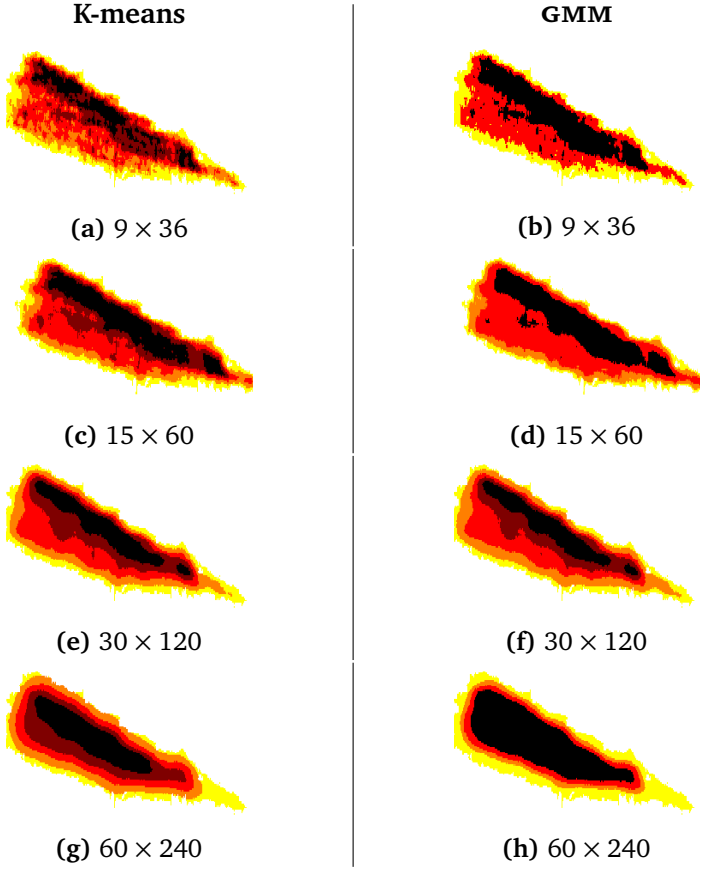


**Figure B.1:** Overview of the importance of the descpeckling filter mask size when performing the within-slick segmentation for the second acquisition (09:03 UTC) of the main slick in Data Set 2. The figure is vertically structured and labeled with the segmentation strategy used in each column of figures, along with the size of the respective filter masks indicated in the subcaption.